1
General Properties of Nitrides

Introduction

GaN as a representative of its binary cousins, InN and AlN, and their ternaries along with the quaternary, is considered one of the most important semiconductors after Si. It is no wonder that it finds ample applications in lighting and displays of all kinds, lasers, detectors, and high-power amplifiers. These applications stem from the excellent optical and electrical properties of nitride semiconductors. The parameters are imperative in determining the utility and applicability of this class of materials to devices, as will be made evident in this chapter and throughout the book.

In this chapter, the structural, mechanical, thermal, chemical, electrical, and optical properties of GaN and its binary cousins as well as the substrates commonly used for nitride epitaxy are treated in a general sense for quick reference. The detailed properties associated with electrical and optical parameters and properties are discussed in chapters dealing with transport and optical processes in GaN and related alloys. Because GaN is used in the form of a thin film deposited on foreign substrates, meaning templates other than GaN, a discussion of heteroepitaxial thin films is of paramount importance. Consequently, the properties of nitride films intricately depend on substrates, inclusive of the inherent properties such as lattice constants and thermal expansion coefficients, and on the process-induced characteristics such as surface preparation and chemical and physical interactions at the surface. These too are discussed in the book.

1.1
Crystal Structure of Nitrides

Group III nitrides can be of crystalline structures: the *wurtzite* (Wz), *zinc blende* (ZB), and *rock salt*. Under ambient conditions, the thermodynamically stable structure is wurtzite for bulk AlN, GaN, and InN. The zinc blende structure for GaN and InN has been stabilized by epitaxial growth of thin films on {0 1 1} crystal planes of cubic substrates such as Si [1], SiC [2], MgO [3], and GaAs [4]. In these cases, the intrinsic tendency to form the Wz structure is overcome by the topological compatibility.

Handbook of Nitride Semiconductors and Devices. Vol. 1. Hadis Morkoç
Copyright © 2008 WILEY-VCH Verlag GmbH & Co. KGaA, Weinheim
ISBN: 978-3-527-40837-5

However, Wz structure could very likely be present at the extended defect sites. The rock salt form is possible only under high pressures and, therefore, is laboratory form of exercise.

Let us now discuss the space groups for the various forms of nitrides. The rock salt, or NaCl, structure (with space group $Fm\overline{3}m$ in the Hermann–Mauguin notation and O_h^5 in the Schoenflies notation) can be induced in AlN, GaN, and InN under very high pressures. The reason for this is that the reduction of the lattice dimensions causes the interionic Coulomb interaction to favor the ionicity over the covalent nature. The structural phase transition to rock salt structure was experimentally observed at the following estimated pressure values: 22.9 GPa (17 GPa in other estimates) for AlN [5], 52.2 GPa for GaN [6], and 12.1 GPa for InN [7]. Rock salt III nitrides cannot be produced by any epitaxial growth.

The space grouping for the zinc blende structure is $F\overline{4}3m$ in the Hermann–Mauguin notation and T_d^2 in the Schoenflies notation. The zinc blende structure has a cubic unit cell, containing four group III elements and four nitrogen elements. (Although the term zinc blende originated in compounds such as ZnS, which could be in cubic or hexagonal phase, it has been used ubiquitously for compound semiconductors with cubic symmetry. The correct term that should be used for the cubic phase of GaN is actually sphalerite. However, to be consistent with the usage throughout the literature, even at the expense of accuracy, the term zinc blende has been used in this book). The position of the atoms within the unit cell is identical to the diamond crystal structure. Both structures consist of two interpenetrating face-centered cubic sublattices, offset by one quarter of the distance along a body diagonal. Each atom in the structure may be viewed as positioned at the center of a tetrahedron, with its four nearest neighbors defining the four corners of the tetrahedron. The stacking sequence for the (1 1 1) close-packed planes in this structure is AaBbCc. Lowercase and uppercase letters stand for the two different kinds of constituents.

The wurtzite structure has a hexagonal unit cell and thus two lattice constants, c and a. It contains six atoms of each type. The space grouping for the wurtzite structure is $P6_3mc$ in the Hermann–Mauguin notation and C_{6v}^4 in the Schoenflies notation. The point group symmetry is 6 mm in the Hermann–Mauguin notation and C_{6v} in the Schoenflies notation. The Wz structure consists of two interpenetrating *hexagonal close-packed* (hcp) sublattices, each with one type of atom, offset along the c-axis by 5/8 of the cell height ($5c/8$). The wurtzite and zinc blende structures are somewhat similar and yet different. In both cases, each group III atom is coordinated by four nitrogen atoms. Conversely, each nitrogen atom is coordinated by four group III atoms. The main difference between these two structures lies in the stacking sequence of closest packed diatomic planes. The Wz structure consists of alternating biatomic close-packed (0 0 0 1) planes of Ga and N pairs, thus the *stacking sequence* of the (0 0 0 1) plane is AaBbAa in the (0 0 0 1) direction.

Although the main interest is in Wz GaN as opposed to zinc blende GaN, a description of stacking sequence of both GaN polytypes with the accepted Ramsdel notation is warranted, so is the stacking order of SiC polytypes that are relevant to GaN because they are used for substrates in GaN epitaxy. Therefore, a generic description of stacking in Wz semiconductors is given below. A comprehensive description of the tetrahedrally coordinated structures is imperative for a clear picture

of nitride semiconductors, particularly the extended defects that are discussed in detail in Chapter 4. The bonds describe a tetrahedron denoted by T, which has one atom species at each of the three corners and the other atom species in its center [8,9]. The basal plane of this structure is defined by one face of the tetrahedron and the bond perpendicular to this plane defines the *c*-axis. A rotation of 180 ° around the *c*-axis produces a twin variant denoted by T′ as shown in Figure 1.1a (left).

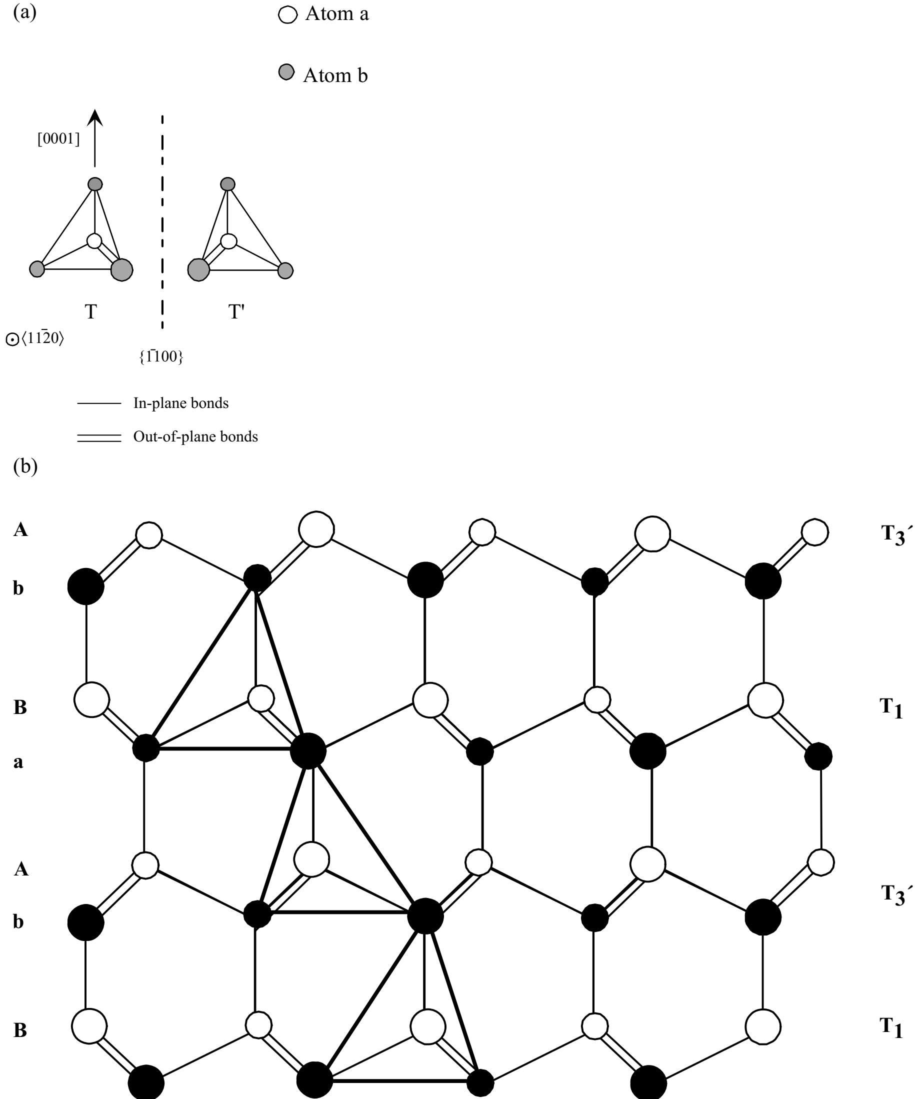

Figure 1.1 Representation of the tetrahedrally coordinated materials in the Ramsdel notation. (a) The two possible tetrahedra. (b) The T_1, T_3', T_1, T_3', tetrahedral stacking composing the 2H sequence. Courtesy of Pierre Ruterana [9].

The two variants (twins T and T′) are related to one another by mirror symmetry about one of the $\{1\,\bar{1}\,0\,0\}$ *m*-planes. A tetrahedron can occupy one of the three possible positions in the basal plane. The representation of the tetrahedrally coordinated materials in the Ramsdel notation is shown in Figure 1.1a for two possible tetrahedra, one is the mirror image twin of the other with respect to the $(1\,\bar{1}\,0\,0)$ *m*-plane. The single bonds are on the $(1\,1\,\bar{2}\,0)$ plane, called the *a*-plane. The layers of the tetrahedra can then be denoted by T_1, T_2, T_3, and by T_1', T_2', T_3' for its twin. An example of T_1, T', T_1, T_3' stacking order representing 2H ordering as in wurtzitic GaN is shown in Figure 1.1b. The structure of nitride semiconductors and most relevant polytypes of SiC can be completely described by a combinatorial stacking of the aforementioned six tetrahedra layers. Naturally, not all the stacking sequences must obey the following two rules to keep a corner sharing structure, as such not all stacking orders are allowed:

(i) A tetrahedron T can be followed by another one of the same kind with the following subscript: $T_1T_2T_3$, and inversely for the twin variant: $T_3'T_2'T_1'$.
(ii) A tetrahedron T_1 must be followed by the twin variant of the preceding subscript: T_1T_3', and inversely for its twin variant: $T_1'T_2$.

In the Ramsdel notation, the stacking order for the wurtzite structure corresponding to various polytypes can be denoted as

- T_1T_3' or T_2T_1' or T_3T_2' for the 2H polytype, which is also applicable to Wz nitride semiconductors;
- $T_1T_2T_1'T_3'$ for the 4H polytype;
- $T_1T_2T_3T_2'T_1'T_3'$ for the 6H polytype;
- $T_1T_2T_3$ or $T_3'T_2'T_1'$ for the 3C polytype.

The 3C, 4H, and 6H stacking sequences as well as 2H sequence on 6H sequence are discussed in Chapter 3.

Recall that GaN crystallizes in the cubic structure (zinc blende or sphalerite, the latter being the correct term and the former being the one used universally) or in the more stable hexagonal structure (wurtzite). The anions (N^{3-}) form an hcp structure in which the cations (Ga^{3+}) occupy half of the tetrahedral sites. The structure of a unit cell of GaN projected along [0 0 0 1] is depicted schematically in Figure 1.2. The open symbols represent γ sites that are occupied by nitrogen atoms; the Ga atoms are in the tetrahedral sites, β. These latter sites can either be at heights $(3/8)c$ above (β_1) or below (β_2) N site, depending on the crystal polarity.

A stick-and-ball representation of Ga-polarity and N-polarity Wz structure is depicted in Figure 1.3. The Wz and zinc blende structures differ only in the bond angle of the second nearest neighbor (Figure 1.4). As clearly shown, the stacking order of the Wz along the [0 0 0 1] *c*-direction is AaBb, meaning a mirror image but no in-plane rotation with the bond angles. In the zinc blende structure along the [1 1 1] direction, there is a 60° rotation that causes a stacking order of AaBbCc. The point with regard to rotation is illustrated in Figure 1.4b. The nomenclature for various commonly used planes of hexagonal semiconductors in two- and three-dimensional versions is presented in Figures 1.5 and 1.6. The Wz group III nitrides lack an

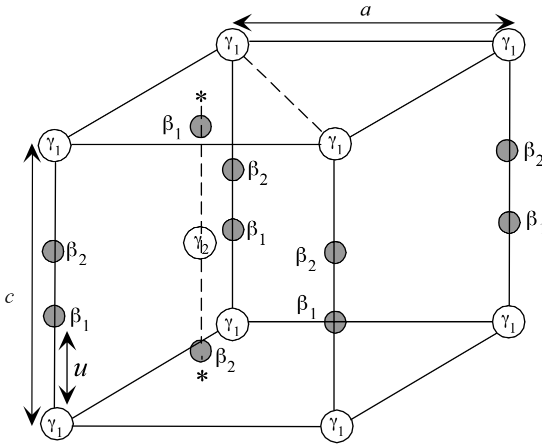

Figure 1.2 Schematic diagram showing the β_1 and β_2 tetrahedral sites of GaN unit cell. Starting with the assumption that N occupies the γ sites, only one family of β sites can be simultaneously occupied by Ga atoms. Courtesy of Pierre Ruterana [9].

inversion plane perpendicular to the *c*-axis; thus, nitride surfaces have either a group III element (Al, Ga, or In) polarity (referred to as Ga-polarity) with a designation of (0 0 0 1) or (0 0 0 1)A plane or a N-polarity with a designation of $(0\,0\,0\,\bar{1})$ or (0 0 0 1)B plane. We will use the former notations for each. The distinction between these two directions is essential in nitrides because of their implications for the polarity of the polarization charge. Three surfaces and directions are of special importance in

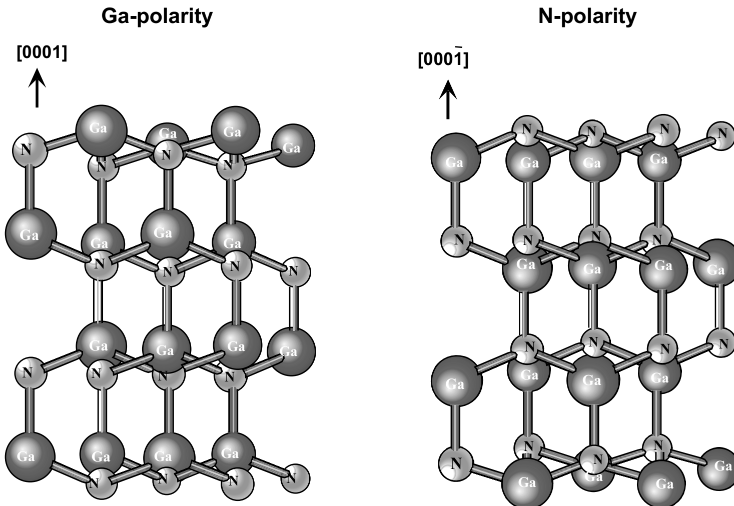

Figure 1.3 A stick-and-ball diagram of a hexagonal structure.

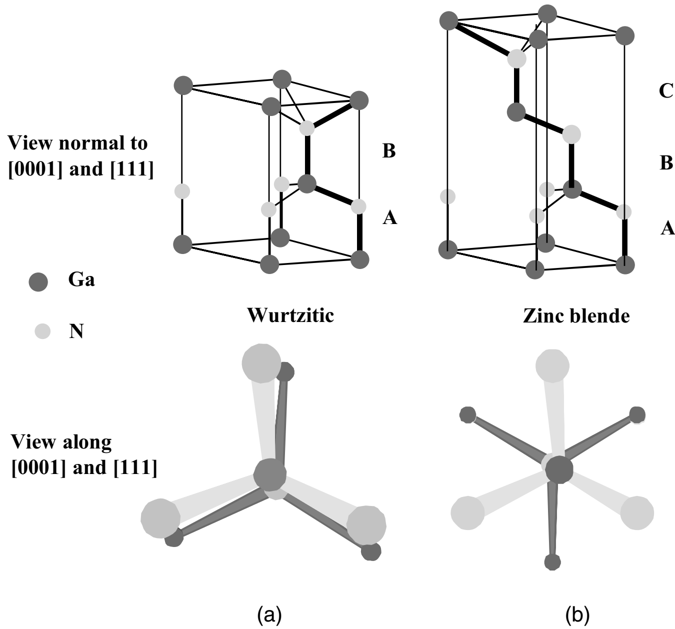

Figure 1.4 A stick-and-ball stacking model of crystals with (a, both top and bottom) 2H wurtzitic and (b, both top and bottom) 3C zinc blende polytypes. The bonds in an A-plane $(1\,1\,\bar{2}\,0)$ are indicated with heavier lines to accentuate the stacking sequence. The figures on top depict the three-dimensional view. The figures at the bottom indicate the projections on the (0 0 0 1) and (1 1 1) planes for wurtzitic and cubic phases, respectively. Note the rotation in the zinc blende case along the ⟨1 1 1⟩ direction. (Please find a color version of this figure on the color tables.)

nitrides, which are (0 0 0 1) *c*-, $(1\,1\,\bar{2}\,0)$ *a*-, and $(1\,\bar{1}\,0\,0)$ *m*-planes and the directions associated with them, ⟨0 0 0 1⟩, $\langle 11\bar{2}0\rangle$, and $\langle 1\bar{1}00\rangle$ as shown in Figure 1.7. The (0 0 0 1), or the basal plane, is the most commonly used surface for growth. The other two are important in that they represent the primary directions employed in reflection high-energy electron diffraction (RHEED) observations in molecular beam epitaxial growth, apart from being perpendicular to one another. They also represent the direction of stripes employed in the *epitaxial lateral overgrowth* (ELO), details of which are discussed in Section 3.5.5.2.

The cohesive energy per bond in the wurtzite form is 2.88 eV (63.5 kcal mol^{-1}), 2.2 eV (48.5 kcal mol^{-1}), and 1.93 eV (42.5 kcal mol^{-1}) for AlN, GaN, and InN, respectively [10]. The calculated energy difference $\Delta E_{\text{W-ZB}}$ between wurtzite and zinc blende lattice is small [11]: $\Delta E_{\text{W-ZB}} = -18.41$ meV/atom for AlN, $\Delta E_{\text{W-ZB}} = -11.44$ meV/atom for InN, and $\Delta E_{\text{W-ZB}} = -9.88$ meV/atom for GaN. Wurtzite form is energetically preferable for all three nitrides compared to zinc blende, although the energy difference is small.

The Wz structure can be represented by lattice parameters a in the basal plane and c in the perpendicular direction, and the *internal parameter u*, as shown in Figure 1.8.

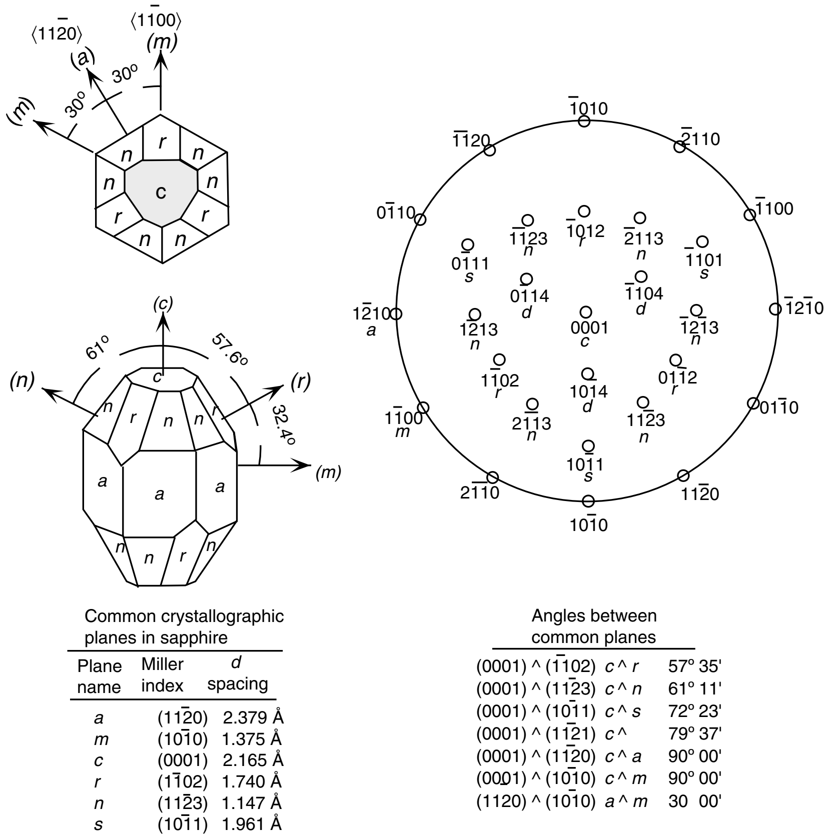

Common crystallographic planes in sapphire

Plane name	Miller index	d spacing
a	$(11\bar{2}0)$	2.379 Å
m	$(10\bar{1}0)$	1.375 Å
c	(0001)	2.165 Å
r	$(1\bar{1}02)$	1.740 Å
n	$(11\bar{2}3)$	1.147 Å
s	$(10\bar{1}1)$	1.961 Å

Angles between common planes

Planes		Angle
(0001) ^ $(\bar{1}\bar{1}02)$	c ^ r	57° 35'
(0001) ^ $(11\bar{2}3)$	c ^ n	61° 11'
(0001) ^ $(10\bar{1}1)$	c ^ s	72° 23'
(0001) ^ $(11\bar{2}1)$	c ^	79° 37'
(0001) ^ $(11\bar{2}0)$	c ^ a	90° 00'
(0001) ^ $(10\bar{1}0)$	c ^ m	90° 00'
(1120) ^ $(10\bar{1}0)$	a ^ m	30 00'

Figure 1.5 Labeling of planes in hexagonal symmetry (* for sapphire).

The *u* parameter is defined as the anion–cation bond length (also the nearest neighbor distance) divided by the *c* lattice parameter. The *c* parameter depicts the unit cell height. The wurtzite structure is a hexagonal close-packed lattice, comprising vertically oriented X–N units at the lattice sites. The *basal plane lattice parameter* (the edge length of the basal plane hexagon) is universally depicted by *a* and the *axial lattice parameter,* perpendicular to the basal plane, is universally described by *c*. The interatomic distance in the basic unit is described by the internal parameter *u*. In an ideal wurtzite structure represented by four touching hard spheres, the values of the axial ratio and the internal parameter are $c/a = \sqrt{8/3} = 1.633$ and $u = 3/8 = 0.375$, respectively. The crystallographic vectors of wurtzite are $\vec{a} = a(1/2, \sqrt{3}/2, 0)$, $\vec{b} = a(1/2, -\sqrt{3}/2, 0)$, and $\vec{c} = a(0, 0, c/a)$. In Cartesian coordinates, the basis atoms are (0, 0, 0), (0, 0, *uc*), $a(1/2, \sqrt{3}/6, c/2a)$, and $a(1/2, \sqrt{3}/6, [u + 1/2]c/a)$.

Table 1.1 tabulates the calculated structural parameters *a*, *c*/*a*, and $\varepsilon_1 = u - u_{\mathrm{ideal}}$ for the III–V nitrides by three different groups [12–14]. In the case of Bernardini *et al.* [12], they optimized the structure within both the *generalized gradient*

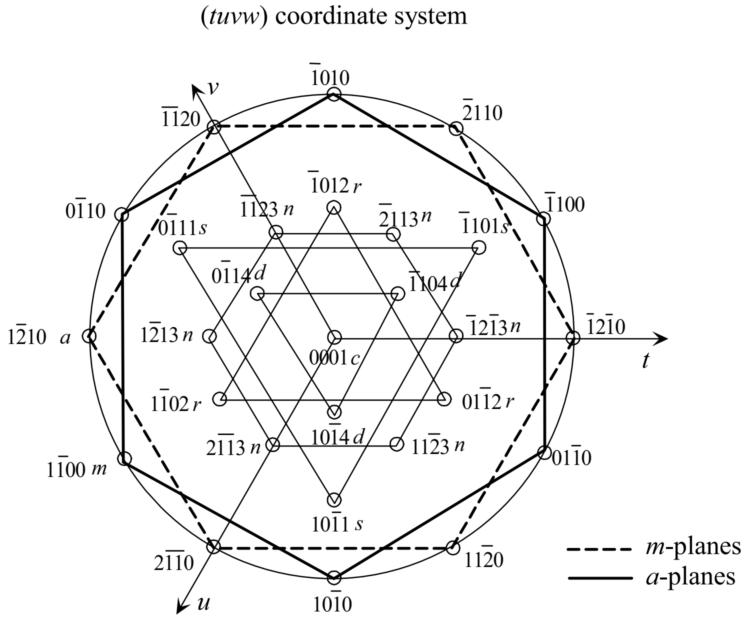

Figure 1.6 A magnified view of labeling of planes in hexagonal symmetry in the (*tuvw*) coordinate system with *w* representing the unit vector in the *c*-direction. The lines are simply to show the symmetry only. If the lines connecting *m*-points among each other and *a*-points among each other were to be interpreted as the projection of those planes on the *c*-plane, the roles would be switched in that the lines connecting the *m*-points would actually represent the *a*-planes and lines connecting the *a*-points would actually represent the *m*-planes that are normal to the plane of the page.

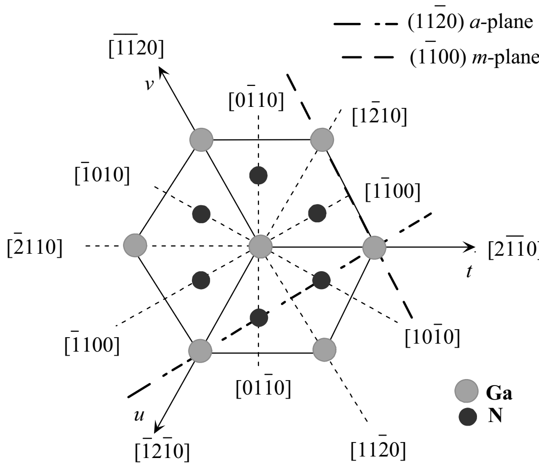

Figure 1.7 The orientations which are commonly used in nitrides, namely the $(11\bar{2}0)$ and $(1\bar{1}00)$ planes and associated directions are shown as projections on the (0001) basal plane.

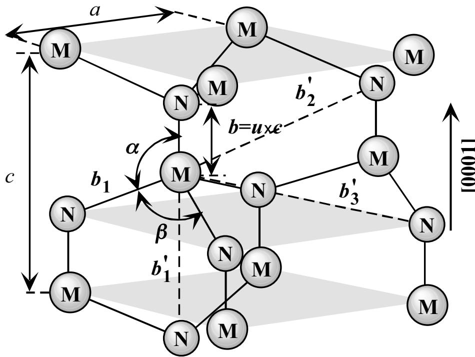

Figure 1.8 Schematic representation of a wurtzitic metal nitride structure with lattice constants *a* in the basal plane and *c* in the basal direction, *u* parameter, which is expressed as the bond length or the nearest neighbor distance (*b*) divided by *c* (0.375 in ideal crystal), α and β (109.47 in ideal crystal) are the bond angles, and b'_1, b'_2, and b'_3, represent the three types of second nearest neighbor distances.

approximation (GGA) and *local density approximation* (LDA). The experimental data are from Leszczynski *et al.* [15].

In all Wz III nitrides, experimentally observed c/a ratios are smaller than ideal and it has been postulated that not being so would lead to the zinc blende phase [16]. There are two avenues that can lead to a deviation from ideal: changing the c/a ratio or changing the u value. It should be pointed out that a strong correlation exists between the c/a ratio and the u parameter so that when c/a decreases, the u parameter increases in a manner to keep the four tetrahedral distances nearly constant through a distortion of tetrahedral angles. For equal bond length to prevail, the following relation must hold:

$$u(1/3)(a^2/c^2)+1/4. \tag{1.1}$$

Table 1.1 Structural parameters for GaN reported by Bechstedt, Großner, and Furthmüller (BGF) [13] and by Wei and Zunger (WZ) [14] using the local density approximation (LDA).

	***a* (Å)**	***c/a***	**ε_1 ($10^{-3}c/a$)**
BGF	3.150	1.6310	6.5
WZ	3.189	1.6259	1.8
BFV (LDA)	3.131	1.6301	1.6
BFV (GGA)	3.197	1.6297	1.9
Experimental data	3.1890	1.6263	2.0

However, Bernardini, Fiorentini, and Vanderbilt [12] employed both the LDA and GGA methods. Lattice constant a is given in Å and ε_1 in $10^{-3}c/a$.

The nearest neighbor bond length along the c-direction (expressed as b in Figure 1.8) and off c-axis (expressed as b_1 in Figure 1.8) can be calculated as

$$b = cu \quad \text{and} \quad b_1 = \sqrt{\frac{1}{3}a^2 + \left(\frac{1}{2} - u\right)^2 c^2}. \tag{1.2}$$

In addition to the nearest neighbors, there are three types of second nearest neighbors designated in Figure 1.8 as b'_1 (one along the c-direction), b'_2 (six of them), and b'_3 (three of them), which are given as [17]

$$b'_1 = c(1-u), \quad b'_2 = \sqrt{a^2 + (uc)^2}, \quad \text{and} \quad b'_3 = \sqrt{\frac{4}{3}a^2 + c^2\left(\frac{1}{2} - u\right)^2}. \tag{1.3}$$

The bond angles, α and β, are given by [17]

$$\alpha = \pi/2 + \arccos\left[\left(\sqrt{1 + 3(c/a)^2(-u + 1/2)^2}\right)^{-1}\right],$$
$$\beta = 2\arcsin\left[\left(\sqrt{4/3 + 4(c/a)^2(-u + 1/2)^2}\right)^{-1}\right]. \tag{1.4}$$

Table 1.2 tabulates the calculated as well as experimentally observed structural parameters discussed above, inclusive of the lattice parameters, the nearest and second nearest neighbor distances, and the bond angles for three end binaries, GaN, AlN, and InN. The distances are in terms of Å.

The lattice parameters are commonly measured at room temperature by X-ray diffraction (XRD), which happens to be the most accurate one, using the Bragg law. In ternary compounds, the technique is also used for determining the composition; however, strain and relevant issues must be accounted for as the samples are in the

Table 1.2 Calculated (for ideal crystal) and experimentally observed structural parameters for GaN, AlN, and InN [17].

	GaN		**AlN**		**InN**	
	Ideal	**Exp.**	**Ideal**	**Exp.**	**Ideal**	**Exp.**
u	0.375	0.377	0.375	0.382	0.375	0.379
a (Å)	3.199	3.199	3.110	3.110	3.585	3.585
c/a	1.633	1.634	1.633	1.606	1.633	1.618
b (Å)	1.959	1.971	1.904	1.907	2.195	2.200
b_1 (Å)	1.959	1.955	1.904	1.890	2.195	2.185
b'_1 (Å)	3.265	3.255	3.174	3.087	3.659	3.600
b'_2 (Å)	3.751	3.757	3.646	3.648	4.204	4.206
b'_3 (Å)	3.751	3.749	3.646	3.648	4.204	4.198
α	109.47	109.17	109.47	108.19	109.47	108.69
β	109.47	109.78	109.47	110.73	109.47	110.24

form of epitaxial layers on foreign substrates. The accuracy of X-ray diffraction and less than accurate knowledge of the elastic parameters together allow determination of the composition to only within about 1% molar fraction. In addition to composition, the lattice parameter can be affected by free charge, impurities, stress (strain), and temperature [18]. Because the c/a ratio correlates with the difference of the electronegativities of the two constituents, components with the greatest differences show the largest departure from the ideal c/a ratio [19]. For GaN, the c/a ratio and the value of u are measured as 1.627 (1.634 in Ref. [17]) and 0.377, respectively, which are close to the ideal values [20]. AlN deviates significantly from the ideal parameters: $c/a = 1.601$ (1.606 in Ref. [17]) and $u = 0.382$. Although the data for InN are not as reliable, values of $u = 0.379$ and $c/a = 1.601$ have been reported [17]. Inhomogeneities, strain, partial relaxation of strain, and high concentration of structural defects may distort the lattice constants from their intrinsic values and cause a wide dispersion among the reported values. Table 1.3 lists a comparison of measured and calculated lattice parameters reported for AlN, GaN, and InN crystallized in the wurtzite structure in more detail in terms of the specifics of the sample used for measurements and complements. The dispersion is even a greater concern in ternary and quaternaries, as compositional inhomogeneities, in addition to the aforementioned issues, cause an additional dispersion. The particulars of the ternaries are discussed in Section 1.5.

The wurtzite polytypes of GaN, AlN, and InN form a continuous alloy system whose direct bandgaps range, according to data that adorned the literature for years, from 1.9 eV for InN, to 3.42 eV for GaN, and to 6.2 eV for AlN. A revisit of the InN bandgap indicates it to be about 0.78 eV [30] and the same for AlN is about 6 eV in which case the energy range covered would be about 0.7–6 eV. Thus, the III–V nitrides could potentially be fabricated into optical devices, which are active at wavelengths ranging from the red well to the ultraviolet. The bandgaps of nitrides,

Table 1.3 Measured and calculated lattice constants of wurtzite AlN, GaN, and InN.

Compound	Sample	*a* (Å)	*c* (Å)
AlN	Bulk crystal [21]	3.1106	4.9795
	Powder [22]	3.1130	4.9816
	Epitaxial layer on SiC [23]	3.110	4.980
	Pseudopotential LDA [24]	3.06	4.91
	FP-LMTO LDA [25]	3.084	4.948
GaN	Bulk crystal [18]	3.189	5.1864
	Relaxed layer on sapphire [26]	3.1892	5.1850
	Powder [29]	3.1893	5.1851
	Relaxed layer on sapphire [27]	3.1878	5.1854
	GaN substrate – LEO [28]	3.1896	5.1855
	Pseudopotential LDA [24]	3.162	5.142
	FP-LMTO LDA [25]	3.17	5.13
InN	Powder [29]	3.538	5.703
	Pseudopotential LDA [24]	3.501	5.669
	FP-LMTO LDA [25]	3.53	5.54

LDA: local density approximation; FP-LMTO: full-potential linear muffin–tin orbital.

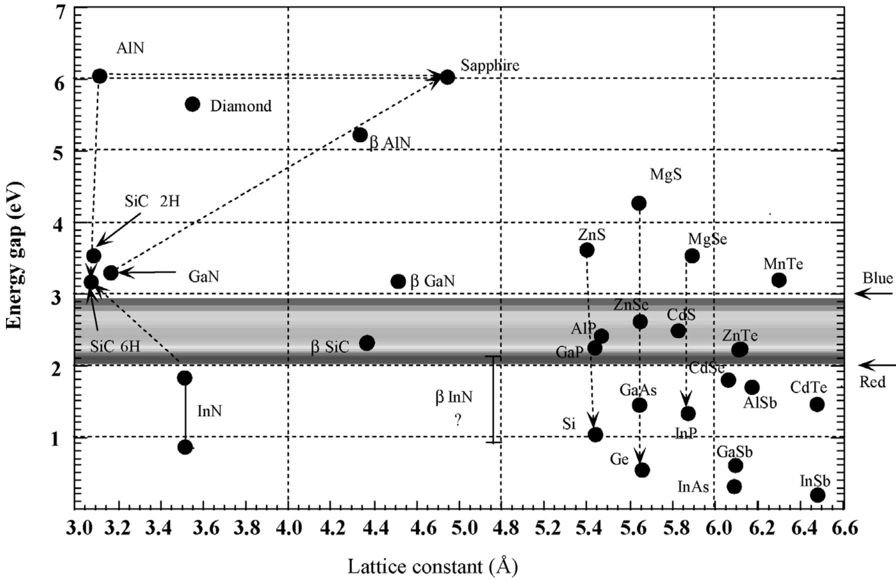

Figure 1.9 The bandgaps of nitrides, substrates commonly used for nitrides, and other conventional semiconductors versus their lattice constants. (Please find a color version of this figure on the color tables.)

substrates commonly used for nitrides, and other conventional semiconductors are shown in Figure 1.9 with respect to their lattice constants.

All III nitrides have partially covalent and partially ionic bonds. The concept of *fractional ionic character* (FIC) is useful in interpreting many physical phenomena in the crystals [31,32]. The FIC may be defined for a binary compound AB as $\mathrm{FIC} = |Q_A^* - Q_B^*|/|Q_A^* + Q_B^*|$, where Q_A^* and Q_B^* are effective charges on atoms A and B. The FIC values range from zero for a covalent compound (each atom has four electrons) to 1 for an ionic compound (all eight electrons belong to the anion). Figure 1.10 displays the charge distribution along the AB bond for all three compounds. The arrow along the bond charge indicates the atomic boundaries in the crystals that are not always at the minimum of the line charge along the bond AB. This should be expected taking into account the partial covalent bond of the compounds, because only in the ionic crystals, the atomic boundary is clearly defined. Table 1.4 lists the calculated effective radii, r_{III} and r_N, the effective charges, and FIC for AlN, GaN, and InN. The ionicity of AlN is high. This may explain the difficulties with AlN doping. It is well known that only covalent semiconductors or semiconductors with a large covalent component can form hydrogen-like shallow levels in the bandgap by substitution of a host atom with a neighbor with one more or one less electron. GaN and InN have a smaller than AlN but nearly equal ionicity. GaN was doped both p- and n-type. Thus, one can expect that InN can also be doped n- and p-type. To date, only n-type InN has been obtained because of high volatility of nitrogen and easiness of nitrogen vacancy formation that acts as a donor in this compound.

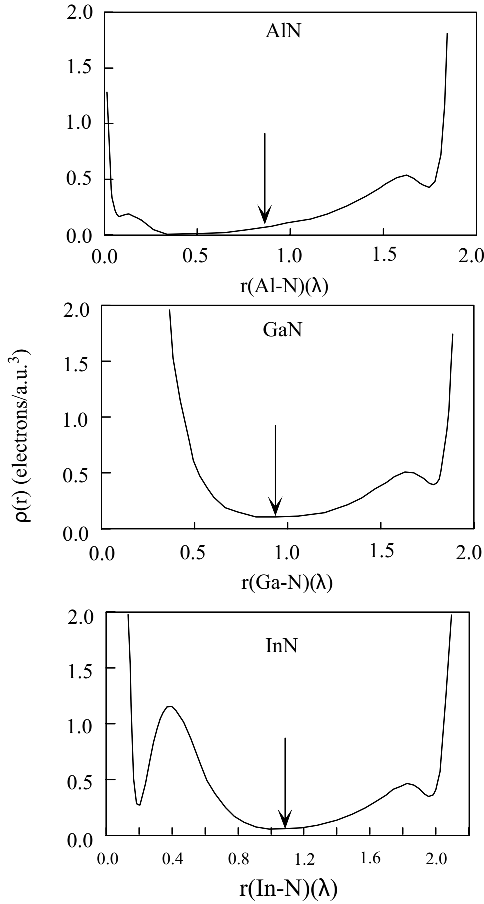

Figure 1.10 Charge density along the III–N bond in III nitride semiconductors.

The III-nitrides are commonly grown on mismatched substrates because of the lack of suitable native substrates. Thus, the epitaxial layers are strained during cool down, if they are sufficiently thick for them to relax at the growth temperature. The mechanical forces related to strain dramatically change the band structure of the epitaxial layers. The pressure dependence of the bandgap energy E_g can be expressed as $E_g = E_g(0)$ $gP + dP^2$, where $E_g(0)$ is the bandgap of stress-free semiconductor, g and d are the

Table 1.4 Calculated ionic radii (Å), effective charges (electrons), and the fractional ionic character (FIC) for III nitrides [32].

Compound	r_{III} (Å)	r_N (Å)	Q^*_{III} (e)	Q^*_N (e)	FIC
AlN	0.8505	1.0523	1.12	6.88	0.72
GaN	0.9340	1.0119	1.98	6.02	0.51
InN	1.0673	1.0673	1.83	6.17	0.54

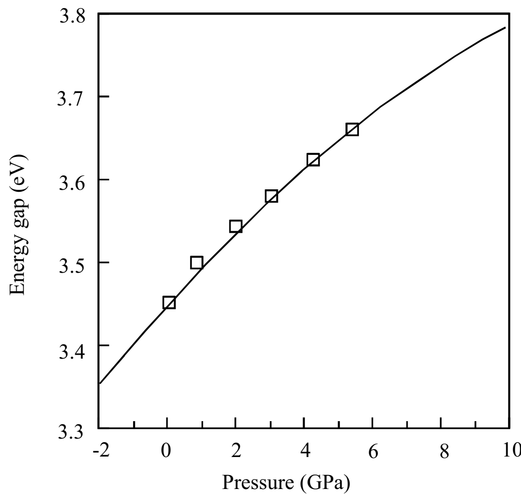

Figure 1.11 Pressure dependence of the GaN energy gap, showing the typical sublinear character. Solid line represents the calculations of Christiansen and Gorczyca [35], which have been rigidly upshifted by ~0.82 eV for a better fit with experiments, and the squares represent experimental results [6].

pressure coefficients, and P is the pressure. For GaN, g and d parameters are 4.2×10^{-3} and -1.8×10^{-5}, respectively [33,34]. The bandgap is in terms of eV and the pressure is in terms of kbar. The pressure dependence has, in general, a sublinear character. The variation of the GaN energy gap with pressure, both theoretical [35] and experimental [6], is shown in Figure 1.11. The calculated pressure coefficients for III nitrides are given in Table 1.5.

Parameters associated with mechanical properties of GaN in wurtzitic phase are tabulated in Tables 1.6 and 1.7, the latter dealing with the sound wave velocity. The same parameters for the zinc blende phase of GaN are tabulated in Tables 1.8 and 1.9.

Table 1.5 Calculated pressure coefficients for III nitrides including wurtzitic, zinc blende, and rock salt phases (g in units of meV GPa^{-1} and d in units of meV GPa^{-2}) [35].

	Wurtzite polytype		Zinc blende polytype		Rock salt polytype	
Compound	***G***	***d***	***g***	***d***	***g***	***d***
AlN	40	−0.32	42	−0.34	43	−0.18
GaN	39	−0.32	40	−0.38	39	−0.32
InN	33	−0.55	16	−0.02	41	−0.08

It should be noted that rock salt phases cannot be synthesized and exist only under high pressures beyond the phase transition point. g and d parameters with values of $E_g = E_g(0) + gP + dP^2$.

Table 1.6 Parameters related to mechanical properties of wurtzitic GaN (in part after Ref. [36]).

Wurtzite polytype GaN	Parameter value/comments	Comments/ references
Group of symmetry	C_{6v}^4 ($P6_3mc$)	
Molar volume, V_c ($cm^3\,mol^{-1}$)	13.61	
Molecular mass ($g\,mol^{-1}$)	83.7267	
Density ($g\,cm^{-3}$)	6.11 or 6.15	The latter by Bougrov *et al.* [37]
Number of atoms in 1 cm^3	8.9×10^{22}	
Lattice constants	$a = 3.1893$ Å for powder, $c = 5.1851$ Å for powder[a]	
Bulk modulus B (GPa) (compressibility^{-1})	210 [38][b] or 20.4×10^{11} dyn cm^{-2} (204 GPa)	The latter by Bougrov *et al.* [37]
dB/dP	4	
Young's modulus (GPa)	150	
Poisson's ratio, ν or σ_0 ($\nu = C_{13}/(C_{11}+C_{12})$)	0.23 ± 0.06 (0.198–0.37) from C parameters	[39]
Knoop's hardness (GPa)	15.5	At 300 K
Surface microhardness ($kg\,mm^{-2}$)	1200–1700	300 K, using Knoop's pyramid test [36,40,41]
Nanoindentation hardness (GPa)	10.8 at 300 K	
Yield strength (GPa)	0.1 at 1000 K	
Deformation potential, E_{ds}	8.54 eV unscreened, 12 eV screened	
C_{11} (GPa)	390 ± 15, 29.6×10^{11} dyn cm^{-2} (296 GPa)	[38,42]
C_{12} (GPa)	145 ± 20, 13.0×10^{11} dyn cm^{-2} (130 GPa)	The second set is from Ref. [43]
C_{13} (GPa)	106 ± 20, 15.8×10^{11} dyn cm^{-2} (158 GPa)	The second set is calculated from the mean square displacement of the lattice atoms measured by X-ray diffraction
C_{33} (GPa)	398 ± 20, 26.7×10^{11} dyn cm^{-2} (267 GPa)	
C_{44} (GPa)	105 ± 10, 2.41×10^{11} dyn cm^{-2} (241 GPa)	

$\nu\langle 0001\rangle = (\Delta a/a_{relaz})/(\Delta c/c_{relax})$ or $\nu\langle 0001\rangle = (\Delta a/a_0)/(\Delta c/c_0)$ with $\Delta a = a_{meas} - a_{relax}$ and $\Delta c_{meas} - c_{relax}$. Conversion: $1\,dyn\,cm^{-2} = 0.1$ Pa (i.e., $1\,GPa = 10^{10}\,dyn\,cm^{-2}$). For details of elastic constants and piezoelectric constants, see Tables 2.27 and 2.28, and at 300 K $B_s = 210\pm10$ GPa, $B_s = [C_{33}(C_{11}+C_{12}) - 2(C_{13})^2]/[C_{11}+C_{12}+2C_{33}-4C_{13}]$.

[a] See Section 1.2.2 for details and lattice parameter for GaN on different substrates

[b] Average of Voigt and Reuss bulk modulus.

Table 1.7 Wave propagation properties in wurtzitic GaN [36].

Wave propagation direction	Wave character	Expression for wave velocity	Wave velocity (in units of 10^5 cm s^{-1})
[1 0 0]	V_L (longitudinal)	$(C_{11}/\rho)^{1/2}$	7.96
	V_T (transverse, polarization along [0 0 1])	$(C_{44}/\rho)^{1/2}$	4.13
	V_T (transverse, polarization along [0 1 0])	$(C_{11}-C_{12})/2\rho)^{1/2}$	6.31
[0 0 1]	V_L (longitudinal)	$(C_{33}/\rho)^{1/2}$	8.04
	V_T (transverse)	$(C_{44}/\rho)^{1/2}$	4.13

Parameters associated with thermal properties of GaN in wurtzitic and zinc blende phases (expected to be identical or nearly identical – treated to be identical here) are tabulated in Table 1.10.

The parameters associated with electrical and optical properties of wurtzitic GaN are tabulated in Table 1.11. The same parameters associated with the zinc blende phase of GaN are tabulated in Table 1.12.

Table 1.8 Parameters related to mechanical properties of zinc blende GaN (in part after Ref. [36]).

Zinc blende polytype GaN	Parameter value/comments	Comments/references
Group of symmetry	$T_d^2(F43m)$	
Molar volume, V_c, ν_a, or Ω (cm^3 mol^{-1})	$(\sqrt{3}a^2c)/4 = 2.283\times10^{-23}$cm^3	
Molecular mass (g mol^{-1})	1.936×10^{-23}	
Density (g cm^{-3})	6.15	
Number of atoms in 1 cm^3	8.9×10^{22}	
Lattice constant (Å)	$a = 4.511-4.52$	
Bulk modulus, B (GPa)	$B_s = 204$ [36], 201 (theory) [45], 237 [46], 200 [47]	$B_s = \frac{C_{33}(C_{11}+C_{12})-2(C_{13})^2}{C_{11}+C_{12}+2C_{33}-4C_{13}}$
dB/dP	3.9, 4.3	
Young's modulus (GPa)	181 [36]	$Y_0 = (C_{11}+2C_{12})(C_{11}-C_{12})/(C_{11}+C_{12})$
Shear modulus, C' (GPa)	67 [36]	$C' = (C_{11}-C_{12})/2$
Poisson's ratio, ν or σ_0	0.352 [36]	ν or $\sigma_0 = C_{13}/(C_{11}+C_{12})$
Knoop's hardness		
Surface microhardness		
Nanoindentation hardness		
Yield strength		
Deformation potential, E_{ds}		
C_{11} (GPa)	293	[42]
C_{12} (GPa)	159	
C_{44} (GPa)	155	

$B_s = [C_{33}(C_{11}+C_{12})-2(C_{13})^2]/[C_{11}+C_{12}+2C_{33}-4C_{13}]$ or $B_s = \frac{C_{33}(C_{11}+C_{12})-2(C_{13})^2}{C_{11}+C_{12}+2C_{33}-4C_{13}}$.

Table 1.9 Wave propagation properties in zinc blende GaN (after Ref. [36]).

Wave propagation direction	Wave character	Expression for wave velocity	Wave velocity (in units of 10^5 cm s^{-1})
[1 0 0]	V_L (longitudinal)	$(C_{11}/\rho)^{1/2}$	6.9
	V_T (transverse)	$(C_{44}/\rho)^{1/2}$	5.02
[1 1 0]	V_L (longitudinal)	$[(C_{11}+C_{12}+2C_{44})/2\rho]^{1/2}$	7.87
	$V_{t//}$(transverse)	$V_{t//}=V_T=(C_{44}/\rho)^{1/2}$	5.02
	$V_{t\perp}$ (transverse)	$[(C_{11}-C_{12})/2\rho]^{1/2}$	3.3
[1 1 1]	V'_1	$[(C_{11}+2C_{12}+4C_{44})/3\rho]^{1/2}$	8.17
	V'_1	$[(C_{11}-C_{12}+C_{44})/3\rho]^{1/2}$	3.96

For the crystallographic directions, see Ref. [44].

Table 1.10 Parameters related to thermal properties of GaN, wurtzitic, and zinc blende phases are expected to be the in this respect with the exception of the first two parameters, which are for the wurtzitic phase (in part Ref. [36]).

GaN	Parameter value/comments	Comments/references
Temperature coefficient (eV K^{-1})	$dE_g/dT=-6.0\times10^{-4}$	Wurtzite structure only
Thermal expansion (K^{-1})	$\Delta a/a=5.59\times10^{-6}$, $\alpha_{\|\|}=\alpha_a=5.59\times10^{-6}$ (wurtzite structure) [48]	$\Delta c/c=3.17\times10^{-6}$; for a plot versus temperature, see Ref. [49] (wurtzite structure only)
Thermal conductivity κ (W cm^{-1} K^{-1})	11.9 at 77 K, 2.3 at 300 K, 1.5 at 400 K	For low dissociation material ($\leq10^6$ cm^{-2})
Debye temperature (K)	600	
Melting point (°C)	>1700 (at 2 kbar), 2500 (at tens of kbar)	[50]
Specific heat (J g^{-1} °C^{-1})	0.49	[37]
Thermal diffusivity (cm^2 s^{-1})	0.43	[37]
Heat of formation, ΔH_{298} (kcal mol^{-1})	−26.4	
Heat of atomization, ΔH_{298} (kcal mol^{-1})	−203	
Heat of sublimation (kcal mol^{-1})	72.4 ± 0.5	
Heat capacity (J mol^{-1} K^{-1})	35.4 at 300 K	
Specific heat (J mol^{-1} K^{-1}) (298 K < T < 1773 K)	$C_p=38.1+8.96\times10^{-3}T$	[51]
Enthalpy, ΔH^0 (kcal mol^{-1})	−37.7	
Standard entropy of formation, ΔS^0 (cal mol^{-1} K^{-1})	−32.43	

The specific heat C_p of Wz GaN at constant pressure for 298 K < T < 1773 K is $C_p=38.1+8.96\times10^{-3}T$ (J mol^{-1} K^{-1}) [51].

Table 1.11 Parameters related to electrical and optical properties of Wz GaN (in part after Refs [36,44]).

Wurtzite polytype GaN	Parameter value/comments			Comments/ references
Bandgap energy, E_g (eV), direct	3.42 at 300 K, 3.505 at 1.6 K			
Breakdown field (cm^{-1})	$3–5\times10^6$ at 300 K			[53]
Electron affinity (eV)	4.1			[37]
Energy separation between Γ and M–L valleys (eV)	−1.9 at 300 K			[37]
	1 at 300 K			[52]
Energy separation between M–L valleys degeneracy (eV)	0.6 at 300 K			[37]
	0.6 at 300 K			[52]
Energy separation between Γ and A valleys (eV)	1.3–2.1 at 300 K			[37]
	2 at 300 K			[52]
Energy separation between A valley degeneracy (eV)	1 at 300 K			[37]
	0.2 at 300 K			[52]
Index of refraction	n (1 eV) = 2.35 or 2.3 2.29, n (3.42 eV) = 2.85 at 300 K (extrapolated to 0 eV), $E\perp c$ interference method (the value for $E\|\|c$ is 1.5(2)% lower at 500 nm); also see energy dependence and long-wavelength value [54]			
Dielectric constants (static)	10.4 ($E\|\|c$)			[55]
	9.5 ($E\perp c$)			[55]
	8.9 in c-direction ($E\|\|c$) at 300 K			[37]
Dielectric constants (high frequency)	5.35			[37]
	5.8 ($E\|\|c$) at 300 K			[56]
	5.35 ($E\perp c$) at 300 K			[55]
	5.47 ($E\|\|c$)			
Optical LO phonon energy (meV)	91.2			[37]
A_1-LO, ν_{A1}(LO) (cm^{-1})	710–735	[57]	744	Reflectivity [55]
A_1-TO, ν_{A1}(TO||) (cm^{-1})	533–534	[34]	533	Raman [56]
E_1-LO, ν_{E1}($LO_\perp$) (cm^{-1})	741–742	[58]	746	Reflectivity [55]
E_1-TO, ν_{E1}($TO_\perp$) (cm^{-1})	556–559	[59]	559	Raman [60]
E_2 (low) (cm^{-1})	143–146			
E_2 (high) (cm^{-1})	560–579			

Table 1.11 (*Continued*)

Wurtzite polytype GaN	Parameter value/comments	Comments/ references
Energy of spin–orbital splitting, E_{so} (meV)	11 (+5, −2) at 300 K calculated from the values of energy gap $E_{g,dir}$ (given in this table)	[61]
Energy of crystal-field splitting, E_{cr} (meV)	40 at 300 K	[37]
	22 (2), calculated from the values of energy gap $E_{g,dir}$ (given in this table)	[61]
Effective electron mass, m_e or $m_e^{//}$	$0.20m_0$ at 300 K	[37]
	$0.20m_0$	[62]
	$0.27m_0$ by Faraday rotation	[52]
	0.138–0.2	
Effective electron mass, $m_{e\perp}$ or $m_e^{\perp}$	$0.20m_0$, 300 K; fit of reflectance spectrum	[63]
	$0.15–0.23m_0$	[52]
Effective hole mass	$0.8m_0$ at 300 K	[64]
Effective hole masses (heavy), m_{hh}	$m_{hh} = 1.4m_0$ at 300 K	Calculated
	$m_{hhz} = m_{hh}^{//} = 1.1m_0$ at 300 K	[15]
	$m_{hh_\perp} = m_{hh}^{\perp} = 1.6m_0$ at 300 K	[70]
	$m_{hh}^{//} = 1.1 - 2.007m_0$	[52]
	$m_{hh}^{\perp} = 1.61 - 2.255m_0$	[52]
Effective hole masses (light)	$m_{lh} = 0.3m_0$ at 300 K	Calculated
	$m_{lhz} = m_{lh}^{//} = 1.1m_0$ at 300 K	[15]
	$m_{lh}^{\perp} = m_{lh_\perp} = 0.15m_0$ at 300 K	[70]
	$m_{lh}^{//} = 1.1 - 2.007m_0$	[52]
	$m_{lh_\perp} = 0.14 - 0.261m_0$	[52]
Effective hole masses (split-off band), m_s	$m_{sh} = 0.6m_0$ at 300 K	Calculated
	$m_{shz} = m_{ch}^{//} = 0.15m_0$ at 300 K	[36]
	$m_{sh_\perp} = m_{ch}^{\perp} = 1.1m_0$ at 300 K	[70]
	$m_{sh_\perp} = m_{ch}^{//} = 0.12 - 0.16m_0$	[52]
	$m_{ch}^{\perp} = 0.252 - 1.96m_0$	[52]
Effective mass of density of state, m_v	$1.4m_0$	[37]
Effective conduction band density of states (cm^{-3})	2.3×10^{18} at 300 K	
Effective valence band density of states (cm^{-3})	4.6×10^{19} at 300 K	
Electron mobility ($cm^2\,V^{-1}\,s^{-1}$)	~1400 experimental at 300 K	50 000 at 20 K [65]
Hole mobility ($cm^2\,V^{-1}\,s^{-1}$)	<20	At 300 K
n-doping range (cm^{-3})	$10^{16}\,cm^{-3}$–high 10^{19}	

(*Continued*)

Table 1.11 (*Continued*)

Wurtzite polytype GaN	Parameter value/comments	Comments/ references
p-doping range (cm^{-3})	10^{16} cm^{-3}–mid 10^{18}	
Diffusion coefficient for electrons ($cm^2 s^{-1}$)	25	[36]
Diffusion coefficient for holes ($cm^2 s^{-1}$)	5, 26, 94	[36,53]

The details of the energies of high symmetry points compiled by Fritsch *et al.* [52] are given in Table 2.1. Dependence of the bandgap on hydrostatic pressure: $E_g = E_g(0) + gP + dP^2$, where $E_g(0)$ is the bandgap of stress-free GaN. The values for g parameter are 39–42 meV GPa^{-1} and the same for d parameter are -0.18 to -0.32 meV GPa^{-2}. For others, see Table 1.5.

The phonon energies are discussed later on in Table 1.27 in detail and effective masses are discussed in Chapter 2. More details of effective masses can be found in Table 2.9.

More should be said about the dielectric constants. Electromagnetic theory indicates that for any longitudinal electromagnetic wave to propagate, the dielectric function $\varepsilon(\omega)$ must vanish. Doing so leads to [66]

$$\frac{\varepsilon(\omega)}{\varepsilon(\infty)} = \frac{\omega_{LO}^2 - \omega^2}{\omega_{TO}^2 - \omega^2}, \tag{1.5}$$

where ω_{LO} and ω_{TO} represent the transverse optical (TO) and longitudinal optical (LO) phonon frequencies and $\varepsilon(\omega)$ and $\varepsilon(\infty)$ represent the low and high (optical) frequency dielectric constants. The phonon branches associated with a wurtzitic symmetry are discussed in Section 1.2.2 dealing with the mechanical properties of GaN. When $\omega = \omega_{LO}$, the dielectric function vanishes, $\varepsilon(\omega_{LO}) = 0$. Equation 1.5 can be expanded to the directional dependence of the dielectric function in nitrides in general and GaN in particular. In the direction parallel to the c-axis or the z-direction, from the Γ point to the A point, in the k-space, (with x, y representing the in-plane coordinates), the low- and high-frequency dielectric functions are related each with the help of A_1(LO) and E_1(TO) phonons through [67]

$$\varepsilon_{//}(\omega) = \varepsilon_{\perp}^{\infty} \frac{\omega^2 - \omega_{//}^2(\mathrm{LO})}{\omega^2 - \omega_{//}^2(\mathrm{TO})}. \tag{1.6}$$

Likewise, Equation 1.5 can be expanded in the direction perpendicular to the c-axis or in the basal plane or the (x, y) plane, the z-direction (in k-space between the Γ point and M (1/2, 0, 0) or K (1/3, 1/3, 0) points), the low- and high-frequency dielectric functions are related each with the help of A_1(TO) and E_1(LO) phonons through

$$\varepsilon_{\perp}(\omega) = \varepsilon_{\perp}^{\infty} \frac{\omega^2 - \omega_{\perp}^2(\mathrm{LO})}{\omega^2 - \omega_{\perp}^2(\mathrm{TO})}, \tag{1.7}$$

where $\perp$ and $//$ indicate in the basal plane and along the c-direction, respectively.

Table 1.12 Parameters related to electrical and optical properties of zinc blende GaN (in part after Refs [36,44]).

Zinc blende polytype GaN	Parameter/comments	Comments/references
Bandgap energy (eV)	3.2–3.28 at 300 K	3.302 at low temperature
Breakdown field ($V\,cm^{-1}$)	$\sim 5\times10^{6}$	[36]
Index of refraction	n (at 3 eV) = 2.9, 2.3	
Dielectric constant (static)	9.7 at 300 K	[37]
	9.2 by $(2\varepsilon_0^{\perp}+\varepsilon_0^{//})/3$ of wurtzitic form	[52]
Dielectric constant (high frequency)	5.3 at 300 K	Using Lyddane–Sachs–Teller relation ($\varepsilon_0/\varepsilon_{high}=\omega^2_{LO}/\omega^2_{TO}$)
Energy separation between Γ and X valleys, E_Γ (eV)	1.4	[36]
	~1.1	[52]
Energy separation between Γ and L valleys, E_L (eV)	1.6–1.9	[36]
	~2	[52]
Spin–orbit splitting in valence band, Δ_{so} or E_{so} (eV)	0.02	At 300 K [36]
	0.017	[69]
Effective electron mass, m_e	$0.13m_0$	At 300 K [37]
	$0.14m_0$	[52]
Effective hole masses (heavy)	$m_{hh}=1.3m_0$, $m_{hh}^{[110]}=1.52m_0$	At 300 K
	$m_{[100]}=0.8m_0$, $m_{hh}^{[100]}=0.84m_0$	[36,70]
	$m_{[111]}=1.7m_0$, $m_{hh}^{[111]}=2.07m_0$	Second set of figures are from Ref. [52], which are deemed more reliable
Effective hole masses (light)	$m_{lh}=0.19m_0$, $m_{lh}^{[110]}=0.20m_0$	
	$m_{[100]}=0.21m_0$, $m_{lh}^{[100]}=0.22m_0$	
	$m_{[111]}=0.18m_0$, $m_{lh}^{[111]}=0.19m_0$	
Effective hole masses (split-off band), m_s, m_{ch}, or m_{so}	$m_{sh}=0.33m_0$,	
	$m_{so}=0.35m_0$	
	$m_{[100]}=0.33m_0$	
	$m_{[111]}=0.33m_0$	
Effective conduction band density of states	$1.2\times10^{18}\,cm^{-3}$	At 300 K [37]
Effective valence band density of states	$4.1\times10^{19}\,cm^{-3}$	At 300 K [37]
Electron mobility ($cm^2\,V^{-1}\,s^{-1}$)	≤1000 at 300 K	[36]
Hole mobility ($cm^2\,V^{-1}\,s^{-1}$)	≤350 at 300 K	[36]
Diffusion coefficient for electrons ($cm^2\,s^{-1}$)	25	[36]
Diffusion coefficient for holes ($cm^2\,s^{-1}$)	9, 9.5, 32	[36]
Electron affinity	4.1 eV	[37]
Optical LO phonon energy (meV)	87.3	At 300 K

The details of the energies of high symmetry points are given in Table 2.1.

For wurtzitic GaN, the various directional components of phonon frequencies are $\omega_{\perp}(\text{LO}) \rightarrow \text{E}_1(\text{LO}) = 91.8$ meV, $\omega_z(\text{LO}) = \omega_{//}(\text{LO}) \rightarrow \text{A}_1(\text{LO}) = 91$ meV, $\omega_{\perp}(\text{TO}) \rightarrow \text{E}_1(\text{TO}) = 69.3$ meV, and $\omega_z(\text{TO}) = \omega_{//}(\text{TO}) \rightarrow \text{A}_1(\text{TO}) = 66$ meV. In the z-direction (along the c-direction) and perpendicular to the z-direction (in basal plane), LO and TO phonons are not mixed. For any direction other than the in-plane and out-of-plane configurations, the LO and TO phonons mix and hybridize. For a given propagation direction with an angle θ relative to the c-axis (0z), one finds three phonon branches. One is an ordinary TO phonon mode with atomic displacement in the (0xy) plane. The other two branches have a mixed TO and LO character and their dielectric functions are given by the solutions of [68]

$$\varepsilon_{//} \cos^2\theta + \varepsilon_{\perp} \sin^2\theta = 0. \tag{1.8}$$

Using the above relationship, the phonon energy as a function of the angle can easily be calculated. Doing so leads to the conclusion that the upper branch (LO-like) remains between A_1(LO) and E_1(LO) energies, whereas the lower branch (TO-like) remains between A_1(TO) and E_1(TO) energies. Therefore, the dispersion remains small compared to the LO–TO separation, owing to the relatively small cell asymmetry and the large ionicity of atomic bonds. A more important consequence of LO–TO mixing is that the TO-like mode becomes coupled to carriers whereas in the c-direction A_1(LO) mode and in the basal plane E_1(LO) phonons couple to the carriers.

For the special case $\omega = 0$ (or very small frequencies compared to the LO and TO phonon frequencies), the relationship between the optical and static dielectric constants reduces to the well-known *Lyddane–Sach–Teller* relationship

$$\frac{\varepsilon(\omega)}{\varepsilon(\infty)} = \frac{\omega_{\text{LO}}^2}{\omega_{\text{TO}}^2}, \tag{1.9}$$

which will be used to determine the optical frequency dielectric constant from the knowledge of A_1(LO) and A_1(TO) phonon frequencies along the c-direction and E_1(LO) and E_1(TO) in the basal plane. This relationship is used very often.

Parameters related to the energy bandgap, carrier mass, and mechanical properties of AlN have been determined [71–76]. Extensive data on all the binary and ternary band structure parameters can be found in Chapter 2. For example, additional parameters on the critical point energies for Wz GaN, AlN, and InN are given in Tables 2.1–2.3, respectively. Tables 2.4–2.6 list the critical point energies for ZB GaN, AlN, and InN, respectively. Effective masses and other band parameters for Wz GaN are listed in Table 2.9. Table 2.10 tabulates the Luttinger band parameters for ZB GaN. Table 2.14 lists the effective band parameters for Wz AlN, whereas the effective masses and band parameters for Wz AlN are tabulated in Table 2.15. Luttinger parameters for ZB AlN are listed in Table 2.16. The band parameters and effective masses for Wz InN are tabulated in Tables 2.19 and 1.20, respectively.

Returning to the content of this chapter, parameters associated with the mechanical properties of AlN in wurtzitic and zinc blende phases are tabulated in Tables 1.13 and 1.14, respectively. The parameters related to the sound wave velocity in wurtzitic AlN are listed in Table 1.15.

Table 1.13 Parameters related to mechanical properties of wurtzitic AlN (in part after Ref. [36]).

Wurtzite AlN	Parameter/comments	Comments/references
Group of symmetry	C_{6v}^4 ($P6_3mc$)	
Number of atoms in 1 cm^3	9.58×10^{22}	
Molar volume, V_c ($cm^3\,mol^{-1}$)	12.47	
Molecular mass ($g\,mol^{-1}$)	40.9882	
Density ($g\,cm^{-3}$)	3.28	
	3.255 $g\,cm^{-3}$ by X-ray	[77]
	3.23 $g\,cm^{-3}$ by X-ray	[78]
Lattice constants	$a=3.112$ Å, $c=4.979$–4.982 Å	
Bulk modulus, B (GPa)	159.9–210.1, 21×10^{11} $dyn\,cm^{-2}$ (210 GPa) ($B_s=210$)	[78]
dB/dP	5.2–6.3	
Young's modulus, E or Y_0 (GPa)	374, 308	The latter from Ref. [79]
Poisson's ratio, ν or σ_0	0.18–0.21	
Poisson's ratio σ_0 along the different crystallographic directions	{0001}, c-plane	0.287 Ref. [80]
	$\{11\bar{2}0\}$, a-plane ($l=\langle0001\rangle, m=\langle1\bar{1}00\rangle$)	0 Ref. [80]
	$\{11\bar{2}0\}$, a-plane ($l=\langle1\bar{1}00\rangle, m=\langle0001\rangle$)	0.216 Ref. [80]
Knoop's hardness (GPa)	10–14 at 300 K	[81]
Nanoindentation hardness (GPa)	18	[82]
Yield strength (GPa)	0.3 at 1000 °C	
Surface microhardness on basal plane (0 0 0 1)	800 $kg\,mm^{-2}$ by 300 K, using Knoop's pyramid test	[36,40,41]
C_{11} (GPa)[a]	410 ± 10	[42,83]
C_{12} (GPa)[a]	149 ± 10	Refer to Table 1.29 as well
C_{13} (GPa)[a]	99 ± 4	Refer to Table 1.29 as well
C_{33} (GPa)[a]	389 ± 10	Refer to Table 1.29 as well
C_{44} (GPa)[a]	125 ± 5	Refer to Table 1.29 as well
Velocity of the longitudinal sound waves, v_l	10 127 $m\,s^{-1}$	[79]
Velocity of the shear waves, v_s	6333 $m\,s^{-1}$	The sound velocities and related elastic module (experimental data)
Longitudinal elastic modulus, C_l	334 GPa	
Shear elastic modulus, C_s	131 GPa	

Conversion: 1 $dyn\,cm^{-2}=0.1$ Pa (i.e., 1 GPa $=10^{10}$ dyn $^-cm^2$). See Table 1.29 for more details. For details of elastic constants and piezoelectric constants, see Tables 2.27 and 2.28. This expression is given already in conjunction with Table 1.6 and it is also $B_s=[C_{33}(C_{11}+C_{12})-2(C_{13})^2]/[C_{11}+C_{12}+2C_{33}-4C_{13}]$. Temperature derivatives of the elastic module: $d\ln C_l/dT=-0.37\times10^{-4}\,K^{-1}$; $d\ln C_s/dT=-0.57\times10^{-4}\,K^{-1}$; $d\ln B_s/dT=-0.43\times10^{-4}\,K^{-1}$.
[a]See Table 1.29 for a more in-depth treatment of these parameters.

Parameters associated with thermal properties of wurtzitic AlN are tabulated in Table 1.16.

Parameters associated with electrical and optical properties of wurtzitic AlN are tabulated in Table 1.17. The same range of parameters associated with the zinc blende

Table 1.14 Parameters related to mechanical properties of zinc blende AlN.

Zinc blende AlN	Not much is known about the zinc blende phase		Comments/references
Lattice constant (Å)	$a = 4.38$		
Bandgap (eV)	5.4, indirect		[84]
E_g^X (eV)	4.9		[84]
E_g^L (eV)	9.3		[84]
Bulk modulus, B (GPa)	228		$B_s = (C_{11}+2C_{12})/3$
Young's modulus (GPa)			$Y_0 = (C_{11}+2C_{12}) \times (C_{11}-C_{12})/(C_{11}+C_{12})$
Shear modulus (GPa)			$C' = (C_{11}-C_{12})/2$
Poisson's ratio, ν or σ_0			ν or $\sigma_0 = C_{12}/(C_{11}+C_{12})$
C_{11} (GPa)	348	304	The latter figures are from Ref. [84]
C_{12} (GPa)	168	160	
C_{44} (GPa)	135	193	
$m_e^*(\Gamma)$	0.25		[84]
$m_l^*(X)$	0.53		[84]
$m_t^*(X)$	0.31		[84]

See Table 2.18 for more details.

phase of GaN is tabulated in Table 1.18. Mechanical, phonon, properties of *epitaxial* AlN (deposited on silicon and sapphire substrates at ~325 K by ion beam assisted deposition (IBAD)) have been investigated by Ribeiro *et al.* Raman scattering measurements revealed interesting features related to the atomic composition and structure of the films [94]. Vibrational modes corresponding to 2TA(L) at ~230 cm^{-1}, 2TA(X) at ~304 cm^{-1}, 2TA(Σ) at ~435 cm^{-1}, TO(Γ) at 520 cm^{-1}, TA(Σ) + TO(Σ) at ~615 cm^{-1}, accidental critical points at ~670 and ~825 cm^{-1}, 2TO(Δ) at ~950 cm^{-1}, 2TO(L) at ~980 cm^{-1}, 2TO(Γ) at ~1085 cm^{-1}, 2TA(X) + 2TO(Γ) at ~1300 cm^{-1}, and 3TO(Γ) at ~1450 cm^{-1} have been observed. While identifying the vibrational modes, one should be wary of the peak at ~2330 cm^{-1} caused by the molecular nitrogen on

Table 1.15 Acoustic wave propagation properties in wurtzite AlN [36].

Wave propagation direction	Wave character	Expression for wave velocity	Wave velocity (in units of 10^5 cm s^{-1})
[1 0 0]	V_L (longitudinal)	$(C_{11}/\rho)^{1/2}$	11.27
	V_T (transverse, polarization along [0 0 1])	$(C_{44}/\rho)^{1/2}$	6.22
	V_T (transverse, polarization along [0 1 0])	$((C_{11}-C_{12})/2\rho)^{1/2}$	6.36
[0 0 1]	V_L (longitudinal)	$(C_{33}/\rho)^{1/2}$	10.97
	V_T (transverse)	$(C_{44}/\rho)^{1/2}$	6.22

For the crystallographic directions, see Ref. [44].

Table 1.16 Parameters related to thermal properties of wurtzitic AlN (in part after Ref. [36]).

Wurtzite polytype AlN	Value	Comments/references
Thermal expansion (K^{-1})	$\Delta a/a = \alpha_{\|\|} = \alpha_a = 4.2 \times 10^{-6}$, $\Delta c/c = \alpha_{ort} = \alpha_c = 5.3 \times 10^{-6}$	[48,85–87]
	$\Delta a/a = 2.9 \times 10^{-6}$, $\Delta c/c = 3.4 \times 10^{-6}$	[88]
	$\alpha_{ort} = \alpha_c = 5.27 \times 10^{-6}$, $\alpha_{\|\|} = \alpha_a = 4.15 \times 10^{-6}$	$T = 20$–$800\,°C$. X-ray, epitaxial layers, by Sirota and Golodushko [89], also see Ref. [48]
Thermal conductivity ($W\,cm^{-1}\,K^{-1}$)	$\kappa = 2.85$–3.2	[90]; later results by Slack *et al.* [91]
Thermal diffusivity ($W\,cm^{-1}\,°C^{-1}$)	2.85 at 300 K	[90]
Debye temperature (K)	950, 1150	
Melting point (K)	3273	[92]
	3023 (between 100 and 500 atm of nitrogen)	[78]
	3487 (2400 °C at 30 bar)	
Specific heat ($J\,g^{-1}\,°C^{-1}$)	0.6	See Figure 1.29 and the expressions below this table
Thermal diffusivity ($cm^2\,s^{-1}$)	1.47	
Heat of formation, ΔH_{298} ($kcal\,mol^{-1}$)	−64	
Heat of atomization, ΔH_{298} ($kcal\,mol^{-1}$)	−209.7	
Free energy, ΔG_{298} ($kcal\,mol^{-1}$)	−68.15	

For $293 < T < 1700$ K, $\Delta a/a_{300} = -8.679 \times 10^{-2} + 1.929 \times 10^{-4} T + 3.400 \times 10^{-7} T^2 - 7.969 \times 10^{-11} T^3$. For $293 < T < 1700$ K, $\Delta c/c_{300} = -7.006 \times 10^{-2} + 1.583 \times 10^{-4} T + 2.719 \times 10^{-7} T^2 - 5.834 \times 10^{-11} T^3$. The specific heat C_p of AlN for constant pressure: for $300 < T < 1800$ K, $C_p = 45.94 + 3.347 \times 10^{-3} T - 14.98 \times 10^5 T^{-2}$ ($J\,mol^{-1}\,K^{-1}$); for $1800 < T < 2700$ K, $C_p = 37.34 + 7.866 \times 10^{-3} T$ ($J\,mol^{-1}\,K^{-1}$). After Ref. [93]. Optical emission measurements indicate the FX_A transition at 6.023 with an associated binding energy of 63 meV, which sets the bandgap of Wz AlN at 6.086.

the surface of c-Si [95]. It is worth noting that, owing to the extremely weak Raman signal usually presented by AlN films, it is not uncommon to ascribe some of the features erroneously to AlN [96].

Conduction band first- and second-order pressure derivatives [36]:

$$E_g = E_g(0) + 3.6 \times 10^{-3} P - 1.7 \times 10^{-6} P^2 \text{ (eV)} \quad [121]$$
$$E_M = E_M(0) + 7.5 \times 10^{-4} P + 1.0 \times 10^{-6} P^2 \text{ (eV)}$$
$$E_L = E_L(0) + 8.0 \times 10^{-4} P + 6.9 \times 10^{-7} P^2 \text{ (eV)}$$
$$E_k = E_k(0) + 6.3 \times 10^{-4} P + 1.7 \times 10^{-6} P^2 \text{ (eV)}$$

where P is pressure in kbar.

Table 1.17 Parameters related to optical and electrical properties of wurtzitic AlN [97–102] (in part from Ref. [36]).

Wurtzite polytype AlN	Parameter	Comments/references
Bandgap energy (eV)	6.026 at 300 K	[103,104]
From the dichroism of the absorption edge, it follows that the $\Gamma_{1'}$ state lies slightly above the Γ_6 state (transition $E \parallel c$ ($\Gamma_{1'v} - \Gamma_{1c}$) at lower energy than transition $E \perp c$ ($\Gamma_{6v} - \Gamma_{1c}$)), both states being split by crystal field interaction [105]	6.2 eV at 300 K	Excitonic contribution near direct edge [105]
	6.23 at 77 K	Excitonic contribution near direct edge [105]
	6.28 at 300 K	Excitonic edge assuming exciton binding energy of 75 meV [106]
	6.086 at 5 K	With a free exciton binding energy of 63 meV [107,108]
	~6.0 at 300 K	
	~6.1 at 5 K	
Breakdown field ($\mathrm{V\,cm^{-1}}$)	$1.2–1.8 \times 10^6$	[36]
$\mathrm{d}E_g/\mathrm{d}P$ ($\mathrm{eV\,bar^{-1}}$)	3.6×10^{-3}	[109,110]
Conduction band energy separation between Γ and M–L valleys (eV)	~0.7	[78]
	~1	[52]
Conduction band energy separation between Γ and M–L valleys	0.6	[78]
Conduction band energy separation between M–L valleys degeneracy (eV)	~0.2	[52]
Conduction band energy separation between Γ and K valleys (eV)	~1.0	[78]
	~0.7	[52]
Conduction band K valley degeneracy (eV)	2	[78]; empirical pseudopotential calculations of Fritsch *et al.* [52] do not show degeneracy at this critical point
Valence band energy of spin–orbital splitting, E_{so} (eV)	0.019 at 300 K	
	0.036	[108]

Table 1.17 (*Continued*)

Wurtzite polytype AlN	Parameter	Comments/references
Valence band energy of crystal field splitting, E_{cr} (eV), Γ_7 on top of Γ_9	−0.225	[108]
Effective conduction band density of states (cm^{-3})	6.3×10^{18}	[78]
Effective valence band density of states (cm^{-3})	4.8×10^{20}	[78]
Index of refraction	n (3 eV) = 2.15 ± 0.05	
Dielectric constant (static)	9.14 at 300 K	By reflectivity [111]
	7.34	[78,112]
	8.5 ± 0.2 at 300 K	
	9.32 for $E//c$ (modeling)	[113]
	7.76 for $E\perp c$ (experiment)	[113]
Dielectric constant (high frequency)	4.6 at 300 K	[111]
	4.68	[78]
	4.77	
	4.84 at 300 K	Reflectivity
	4.35 for $E//c$ (modeling)	[113]
	4.16 for $E\perp c$ (experiment)	[113]
Infrared refractive index	2.1–2.2 at 300 K	Epitaxial films and monocrystal
	1.9–2.1 at 300 K	Polycrystalline films
	1.8–1.9 at 300 K	Amorphous films [87]
	3 for $E//c$ (modeling)	[113]
	2.8 for $E\perp c$ (experiment)	[113]
Effective electron mass, m_e	0.27 and $0.35m_0$	[14,114,115]
	$0.25–0.39m_0$	[107]
	$0.4m_0$ at 300 K	
	$m_e^{//} = 0.231 - 0.35m_0$	[52]
	$m_e^{\perp} = 0.242 - 0.25m_0$	
Effective hole masses (heavy)	$m_{hh}^{//} = 3.53m_0$ at 300 K	[116]
For k_z direction m_{hz} or $m_{hh}^{//}$	$2.02–3.13m_0$ at 300 K	[107]; from Mg binding energy
For k_x direction m_{hx} or $m_{hh}^{\perp}$	$m_{hh}^{\perp} = 10.42m_0$ at 300 K	[116]
	$m_{hh}^{//} = 1.869 - 4.41m_0$	[52]
	$m_{hh}^{\perp} = 2.18 - 11.14m_0$	[52]
Effective hole masses (light)	$3.53m_0$, $0.24m_0$	At 300 K [116]
For k_z direction m_{lz} or $m_{lh}^{//}$	$m_{lh}^{//} = 1.869 - 4.41m_0$	[52]
For k_x direction m_{lx} or $m_{lh}^{\perp}$	$m_{lh}^{\perp} = 0.24 - 0.350m_0$	[52]
Effective hole masses (split-off band)	$0.25m_0$ at 300 K	[116]
	$3.81m_0$ at 300 K	
For k_z direction m_{soz} or $m_{ch}^{//}$	$m_{ch}^{//} = 0.209 - 0.27m_0$	[52]
For k_x direction m_{sox} or $m_{ch}^{\perp}$	$m_{ch}^{\perp} = 1.204 - 4.41m_0$	[52]

(*Continued*)

Table 1.17 (*Continued*)

Wurtzite polytype AlN	Parameter			Comments/references
Effective mass of density of state, m_v	$7.26m_0$ at 300 K			[116]
Optical phonon energy (meV)	99.2			
$\nu_{TO}(E_1)$ phonon wave number (cm^{-1})[b]	895	614	608	First column [117]; second column [118]; third column [113]
$\nu_{LO}(E_1)$ phonon wave number (cm^{-1})	671.6	821	888.9	See Table 1.30 for more details
$\nu_{TO}(A_1)$ phonon wave number (cm^{-1})	888	514	667.2	
$\nu_{LO}(A_1)$ phonon wave number (cm^{-1})	659.3	663	909	
$\nu(E_2)$ phonon wave number (cm^{-1})	303[a]	426		
$n_{TO}(E_1)$ phonon wave number (cm^{-1})	657–673			[87,111,119,120]
$n_{TO}(A_1)$ phonon wave number (cm^{-1})	607–614 or 659–667			
$n_{LO}(E_1)$ phonon wave number (cm^{-1})	895–924			
$n_{LO}(A_1)$ phonon wave number (cm^{-1})	888–910			
$n^{(1)}(E_2)$ phonon wave number (cm^{-1})	241–252			
$n^{(2)}(E_2)$ phonon wave number (cm^{-1})	655–660			

The details of the energies of high symmetry points are given in Table 2.2. See Table 1.30 for additional details for phonon wave numbers. More details of effective masses can be found in Table 3.15. Temperature dependence of energy gap: $E_g = E_g(0) - 1.799 \times 10^{-3} T^2/(T + 1462)$ (eV) by Guo and Yoshida [103].

[a] Room-temperature Raman, tentative.

[b] For more details regarding vibrational modes, refer to Section 1.3.1.

Phase transition from the wurtzite phase to the rock salt structure (space group O_h^5; lattice parameter 4.04 Å) takes place at the pressure of 17 GPa (~173 kbar) [109,110].

Parameters associated with the electrical and optical properties of zinc blende AlN are listed in Table 1.18. For details regarding the Luttinger parameters for the valence band in zinc blende AlN, refer to Table 2.16. Parameters associated with the mechanical properties of wurtzitic InN are tabulated in Table 1.19.

For wurtzite crystal structure, the surfaces of equal energy in Γ valley should be ellipsoids, but effective masses in the z-direction and perpendicular directions are estimated to be approximately the same.

Table 1.18 Parameters related to optical and electrical properties of zinc blende AlN.

Zinc blende polytype of AlN	Value	Comments/references
Bandgap energy (eV)	4.2; 6.0	All at 300 K
	5.8	[52]
	All (theory)	
Dielectric constant (static)	9.56	[a]
Dielectric constant (high frequency)	4.46	[a]
Energy separation between	~0.7	[52]
Γ and X valleys E_Γ (eV)	0.5	[84]
Energy separation between	~2.3	[52]
Γ and L valleys E_L (eV)	3.9	[84]
Spin–orbit splitting in valence band, Δ_{so} or E_{so} (eV)	0.019	[84]
Deformation potential (eV)	−9	[84]
Effective electron mass, m_e	$0.23m_0$	[52]
Effective hole masses (heavy)	$m_{hh}^{[100]} = 1.02m_0$	[52]
	$m_{hh}^{[111]} = 2.64m_0$	
	$m_{hh}^{[110]} = 1.89m_0$	
Effective hole masses (light)	$m_{lh}^{[100]} = 0.37m_0$	[52]
	$m_{lh}^{[111]} = 0.30m_0$	
	$m_{lh}^{[110]} = 0.32m_0$	
Effective hole masses (split-off band), m_s, m_{ch}, or m_{so}	$0.54m_0$	[52]
Luttinger parameter γ_1	1.85	[52]
Luttinger parameter γ_2	0.43	
Luttinger parameter γ_3	0.74	

[a] C. Persson, and A. Ferreira da Silva, "Linear optical response of zinc-blende and wurtztie III-N (III = B, AI, Ga, and In)", Journal of Crystal Growth 305 pp. 408–413 (2007)

The parameters associated with thermal properties of wurtzitic InN are tabulated in Table 1.20.

The specific heat C_p of InN at constant pressure for $298\,K < T < 1273\,K$ [51] is $C_p = 38.1 + 1.21 \times 10^{-2} T\,(\mathrm{J\,mol^{-1}\,K^{-1}})$. Refer to Table 1.31 for a detailed treatment of mechanical properties of InN.

The parameters associated with electrical and optical properties of wurtzitic InN are tabulated in Table 1.21.

Available parameters associated with the mechanical properties of zinc blende InN, primarily calculated, are tabulated in Table 1.22. Other parameters dealing with electrical and optical properties of zinc blende InN, primarily calculated, are listed in Table 1.23.

Table 1.19 Parameters related to mechanical properties of wurtzitic InN (in part after Ref. [36]).

Wurtzite InN	Value		Comments/references
Group of symmetry	C_{6v}^4 ($P6_3mc$)		
Molar volume ($cm^3\,mol^{-1}$)	18.49		
Molar mass (g mol−1)	128.827		
Density ($g\,cm^{-3}$)	6.89		
	6.98		Measured by displacement
	6.81		X-ray, 298.15 K [122]
Lattice constants (Å)	$a = 3.548$		Epitaxial layers, X-ray [123];
	$a = 3.5446$		300 K [124]
	$a = 3.533$		
	$c = 5.760$		Epitaxial layers, X-ray [123];
	$c = 5.7034$		300 K [124]
	$c = 5.693$		
Bulk modulus B (GPa)	165		
	140		[124]
dB/dP	3.8		
Nanoindentation hardness(GPa)	11.2		[125]
Young's modulus (GPa)			Can be calculated using S parameters and Equation 2.10
Poisson's ratio, ν or σ_0			0.82, 0.68
Knoop's hardness (GPa)			
Deformation potential, E_{ds}	7.10 eV		Estimate
C_{11} (GPa)	223		[42]
C_{12} (GPa)	115		[42]
C_{13} (GPa)	92	$C_{31} = 70$	[42]
C_{33} (GPa)	224	205	[42]
C_{44} (GPa)	48		[42]

$E_g = E_g(0) + 3.3 \times 10^{-2} P$ (eV), where P is pressure in GPa [35,126]. For details of elastic constants and piezoelectric constants, see Table 2.19. $B_s = [C_{33}(C_{11} + C_{12}) - 2(C_{13})^2]/[C_{11} + C_{12} + 2C_{33} - 4C_{13}]$.

1.2 Gallium Nitride

Despite the fact that GaN has been studied far more extensively than the other group III nitrides, further investigations are still needed to approach the level of understanding of technologically important materials such as Si and GaAs. GaN growth often suffers from large background n-type carrier concentrations because of native defects and, possibly, impurities. The lack of commercially available native substrates

Table 1.20 Parameters related to thermal properties of wurtzitic InN (in part after Ref. [36]).

Wurtzite polytype InN	Value	Comments/references
Temperature coefficient	$dEg/dT = -1.8 \times 10^{-4}$ eV K^{-1}	
Thermal expansion	$\Delta a/a = 2.70 \times 10^{-6}$ K^{-1}; $\Delta c/c = 3.40 \times 10^{-6}$ K^{-1}	At 190 K
	$\Delta a/a = 2.85 \times 10^{-6}$ K^{-1}; $\Delta c/c = 3.75 \times 10^{-6}$ K^{-1}	At 260 K
	$\Delta a/a = 3.15 \times 10^{-6}$ K^{-1}; $\Delta c/c = 4.20 \times 10^{-6}$ K^{-1}	At 360 K
	$\Delta a/a = 3.45 \times 10^{-6}$ K^{-1}; $\Delta c/c = 4.80 \times 10^{-6}$ K^{-1}	At 460 K
	$\Delta a/a = 3.70 \times 10^{-6}$ K^{-1}; $\Delta c/c = 5.70 \times 10^{-6}$ K^{-1}	At 560 K
	$\alpha_a = 3.8 \times 10^{-6}$ K^{-1}; $\alpha_c = 2.9 \times 10^{-6}$ K^{-1}	[124]
Thermal conductivity	0.8 ± 0.2 W cm^{-1} K^{-1}	Estimate [127]
	0.45 W cm^{-1} °C^{-1}	
	1.76 W cm^{-1} °C^{-1}, 300 K (estimate for ideal InN)	
Heat of formation, ΔH_{298} (kcal mol^{-1}) (Wz)	−4.6	
Heat of atomization, ΔH_{298} (kcal mol^{-1})	−175	
Melting point	1373 K	[92]
	2146 K, vapor pressure 10^5 bar at 1100–1200 °C	
Debye temperature	660 K at 300 K	[124]
	370 K at 0 K	[128]
Specific heat (J mol^{-1} K^{-1})	$C_p = 38.1 + 1.21 \times 10^{-2} T$	[51]
Heat capacity, C_p (cal mol^{-1} K^{-1})	$9.1 + 2.9 \times 10^{-3} T$	298–1273 K
Entropy, S^0 (cal mol^{-1} K^{-1})	10.4	298.15 K
TSFC^w at formation, ΔH_f^0 (kcal mol^{-1})	−34.3, −30.5	Experimental 298.15 K
TSFC^a at formation, ΔS_f^0 (kcal mol^{-1} K^{-1})	−25.3	Experimental 298.15 K
TSFC^w at formation, ΔG_f^0 (kcal mol^{-1})	−22.96	Experimental 298.15 K
TSFC^w at fusion, ΔH_m (kcal mol^{-1})	14.0	Theoretical
TSFC^w at fusion, ΔS_m (cal mol^{-1} K^{-1})	10.19 cal mol^{-1} K^{-1}	Theoretical
N_2 equilibrium vapor pressure	1 atm	800 K
	10^5 atm	1100 K

[a]TSFC: thermodynamic state function changes.

exacerbates the situation. These, together with the difficulties in obtaining p-type doping, and the arcane fabrication processes caused the early bottlenecks stymieing progress. Information available in the literature on many of the physical properties of GaN is in some cases still in the process of evolution, and naturally controversial. This

Table 1.21 Parameters related to electrical and optical properties of wurtzitic InN (in part after Ref. [36]).

Wurtzitic InN	Value	Comments/references
Bandgap energy, E_g (300 K)	1.89 eV, 1.5 eV, 0.78 eV	See Section 1.3.1 for an expanded discussion
Electron affinity		
Dielectric constant (static)	15.3	300 K [124]
Dielectric constant (static, ordinary direction)	$\varepsilon_{0,ort} = 13.1$	300 K [128]
Dielectric constant (static, extraordinary direction)	$\varepsilon_{0,\parallel} = 14.4$,	300 K [128]
Dielectric constant (high frequency)	8.4	300 K, using the Lyddane–Sachs–Teller relation ($\varepsilon_0/\varepsilon_{high} = \omega_{LO}^2/\omega_{TO}^2$) [129,130]
	9.3	Heavily doped film, infrared reflectivity [131]
	5.8	[132]
Infrared refractive index	2.9	At 300 K [124]
	2.56	At 300 K and $\lambda = 1.0\,\mu m$, interference method; $n = 3$–$10^{20}\,cm^{-3}$ [131]
	2.93	At $\lambda = 0.82\,\mu m$ [131]
	3.12	At $\lambda = 0.66\,\mu m$ [131]
	Reported range: 2.80–3.05	
Energy separation between Γ and M–L valleys (eV)	2.9–3.9	300 K [124]
	~4.8	[52]
Energy separation between M–L valleys degeneracy	0.6	300 K [124]
	~0.7	[52]
Energy separation between Γ and A valleys (eV)	0.7–2.7	300 K [124]
	~4.5	[52]
Energy separation between A valley degeneracy	1	300 K [124]
	~0.6	[52]
Energy separation between Γ and Γ_1 valleys (eV)	1.1–2.6	300 K [124]
Energy separation between Γ_1 valley degeneracy (eV)	1	300 K [124]
Effective conduction band density of states	$9 \times 10^{17}\,cm^{-}$	300 K [124]
Effective valence band density of states	$5.3 \times 10^{19}\,cm^{-3}$	300 K [124]
Valence band crystal field splitting, E_{cr}	0.017 eV	300 K [124]

Table 1.21 (*Continued*)

Wurtzitic InN	Value	Comments/references
Valence band spin–orbital splitting, E_{so}	0.003 eV	300 K [124]
Index of refraction	~2.9 at 300 K	[124]
	2.56 at 300 K (interference method; $n = 3–10^{20}\,cm^{-3}$, $\lambda = 1.0\,\mu m$)	[131]
	2.93	[131]
	3.12	[131]
Effective electron mass, m_e^*	$0.11m_0$	[133]
	$m_e^{//} = 0.1 - 0.138m_0$	[52]
	$m_e^{\perp} = 0.1 - 0.141m_0$	[52]
Effective hole masses (heavy), m_h	$1.63m_0$ at 300 K	[32,134,135]
	$0.5m_0$ at 300 K	[136]
	$m_{hh}^{//} = 1.350 - 2.493m_0$	[52]
	$m_{hh}^{\perp} = 1.410 - 2.661\ m_0$	[52]
Effective hole masses (light), m_{lp}	$0.27m_0$ at 300 K	[32,134,135]
	$m_{lh}^{//} = 1.350 - 2.493m_0$	[52]
	$m_{lh}^{\perp} = 0.11 - 0.196m_0$	[52]
Effective hole masses (split-off band), m_s	$0.65m_0$ at 300 K	[32,134,135]
	$m_{ch}^{//} = 0.092 - 0.14m_0$	[52]
	$m_{ch}^{\perp} = 0.202 - 3.422$	[52]
Effective mass of density of state, m_v	$1.65m_0$ at 300 K	[134,135]
Optical LO phonon energy (meV)	73 at 300 K	[124]

The details of the energies of high symmetry points are given in Table 2.3. More details of effective masses can be found in Table 2.19.

Table 1.22 Available parameters for mechanical for zinc blende InN.

Zinc blende InN	Value	Comments/references
Lattice constant	$a = 4.98$ Å	
Density ($g\,cm^{-3}$)	6.97	Derived from X-ray data
Bulk modulus (GPa)	138–155, 145.6 [42]	$B_s = (C_{11} + 2C_{12})/3$
dB/dP		3.9–4.0
Young's modulus (GPa), Y_0 or E		$Y_0 = (C_{11} + 2C_{12})\cdot(C_{11} - C_{12})/(C_{11} + C_{12})$
Shear modulus (GPa)		$C' = (C_{11} - C_{12})/2$
Poisson's ratio, ν or σ_0		ν or $\sigma_0 = C_{12}/(C_{11} + C_{12})$
C_{11} (GPa)	187	See Ref. [42]
C_{12} (GPa)	125	See Table 1.31 for details
C_{44} (GPa)	86	

Table 1.23 Available electrical and optical properties of zinc blende InN, primarily calculated.

Zinc blende InN	Value	Comments/references
Bandgap energy, E_g (300 K)	2.2 eV	In the absence of any reliable data, the bandgap to a first extent can be assumed to be similar to that for Wz InN. See Ref. [137] for a detailed treatment
	1.5–2.1 (theory)	
	0.2 eV below the Wz polytype	[138]
Dielectric constant	8.4	LWL
	12.45	By $\frac{(2\varepsilon_0^{\perp}+\varepsilon_0^{//})}{3}$ of wurtzitic form (the spur)
Dielectric constant (high frequency)		Using Lyddane–Sachs–Teller relation ($\varepsilon_0/\varepsilon_{high}=\omega_{LO}^2/\omega_{TO}^2$)
Refractive index at LWL	2.88 ± 0.30	Theory
at 600–800 nm	2.90 ± 0.30	—
at 900–1200 nm	2.90	Transmission interference
at 900–1200 nm	3.05 ± 0.30	Transmission interference
at 620 nm	2.65	NIRSR
Density (g cm^{-3})	6.97	Derived from X-ray data
Energy separation between Γ and X_1^c valleys E_Γ (eV)	3	[52]
Energy separation between Γ and L valleys E_L (eV)	2.6	[52]
Spin–orbit splitting in valence band, Δ_{so} or E_{so} (eV)	0.006	[84]
Effective electron mass, m_e	$0.13m_0$	[52]
Effective hole masses (heavy)	$m_{hh}^{[110]}=2.12\ m_0$	[52]
	$m_{hh}^{[100]}=1.18\ m_0$	
	$m_{hh}^{[111]}=2.89\ m_0$	
Effective hole masses (light)	$m_{lh}^{[110]}=0.20\ m_0$	[52]
	$m_{lh}^{[100]}=0.21\ m_0$	
	$m_{lh}^{[111]}=0.19\ m_0$	
Effective hole masses (split-off band), m_s or m_{ch} or m_{so}	$0.36m_0$	[52]

LWL: long-wavelength limit; NIRSR: normal incidence reflectance of synchrotron radiation.

is in part a consequence of measurements being made on samples of widely varying quality. For this book, when possible we have disregarded the spurious determination. However, measurements are too few to yield a consensus, in which case the available data are simply reported.

The burgeoning interest in nitrides has led to substantial improvements in the crystal growth and processing technologies, thus overcoming many difficulties encountered earlier. Consequently, a number of laboratories consistently obtained high-quality GaN with room-temperature background electron concentrations as low as $5\times10^{16}\,cm^{-3}$. The successful development of approaches leading to p-type GaN has led to the demonstration of excellent p–n junction LEDs in the UV, violet, blue, green, and even yellow bands of the visible spectrum with brightness suitable for outdoor displays, CW lasers, and UV detectors, including the ones for the solar blind region. Moreover, power modulation doped field effect transistors (MODFETs) also generically referred to as heterojunction field effect transistors (HFETs) have been developed. What follows reports on the state of knowledge regarding the physical properties of GaN.

1.2.1 Chemical Properties of GaN

Since Johnson *et al.* [139] first synthesized GaN in 1932, a large body of information has repeatedly indicated that GaN is an exceedingly stable compound exhibiting significant hardness. It is this chemical stability at elevated temperatures combined with its hardness that has made GaN an attractive material for protective coatings. Moreover, owing to its wide energy bandgap, it is also an excellent candidate for device operation at high temperatures and caustic environments. Although the hardness may have initiated the interest in GaN, it is the excellent semiconducting features that have piqued the attention of researchers. While the thermal stability of GaN allows freedom of high-temperature processing, the chemical stability of GaN presents a technological challenge. Conventional wet etching techniques used in semiconductor processing have not been as successful for GaN device fabrication. For example, Maruska and Tietjen [140] reported that GaN is insoluble in H_2O, acids, or bases at room temperature, but does dissolve in hot alkali solutions at very slow rates. Pankove [141] noted that GaN reacts with NaOH forming a GaOH layer on the surface and prohibiting wet etching of GaN. To circumvent this difficulty, he developed an electrolytic etching technique for GaN. Low-quality GaN has been etched at reasonably high rates in NaOH [142,143], H_2SO_4 [144], and H_3PO_4 [145–147]. Although these etches are extremely useful for identifying defects and estimating their densities in GaN films, they are not as useful for the fabrication of devices [148]. Well-established chemical etching processes do help for the device technology development, and the status of these processes in the case of GaN can be found in Volume 2, Chapter 1. Various dry etching processes reviewed by Mohammad *et al.* [149] and Pearton *et al.* [150] are promising possibilities and are discussed in Volume 2, Chapter 1.

1.2.2 Mechanical Properties of GaN

GaN has a *molecular weight* of 83.7267 $g\,mol^{-1}$ in the hexagonal wurtzite structure. The lattice constant of early samples of GaN showed a dependence on growth conditions, impurity concentration, and film stoichiometry [151]. These observations were

attributed to a high concentration of interstitial and bulk extended defects. A case in point is that the lattice constants of GaN grown with higher growth rates were found to be larger. When doped heavily with Zn [152] and Mg [153], a lattice expansion occurs because at high concentrations the group II element begins to occupy the lattice sites of the much smaller nitrogen atom. At room temperature, the lattice parameters of GaN platelets [18] prepared under high pressure at high temperatures with an electron concentration of $5\times10^{19}\,\text{cm}^{-3}$ are $a = 3.1890 \pm 0.0003$ Å and $c = 5.1864 \pm 0.0001$ Å. The freestanding GaN with electron concentration of about $10^{16}\,\text{cm}^{-3}$, originally grown on sapphire (0 0 0 1) by hydride vapor phase epitaxy (HVPE) followed by liftoff, has lattice constants of $a = 3.2056 \pm 0.0002$ Å and $c = 5.1949 \pm 0.0002$ Å. For GaN powder, a and c values are in the range of 3.1893–3.190 and 5.1851–5.190 Å, respectively. Experimentally observed c/a ratio for GaN is 1.627, which compares well with 1.633 for the ideal case, and the u parameter calculated using Equation 1.1 is 0.367, which is very close to the ideal value of 0.375.

For more established semiconductors with the extended defect concentration from low to very low, such as Si, GaAs, and so on, the effect of doping and free electrons on the lattice parameter has been investigated rather thoroughly. In bulk GaN grown by the high-pressure technique, the lattice expansion by donors with their associated free electrons has been investigated [18]. However, large concentration of defects and strain, which could be inhomogeneous, rendered the studies of this kind less reliable in GaN layers. In spite of this, the effect of Mg doping on the lattice parameter in thin films of GaN has been investigated. Lattice parameters as large as 3.220–5.200 Å for a and c values, respectively, albeit not in all samples with similar hole concentrations, have been reported [154]. For GaN bulk crystals grown with high-pressure techniques and heavily doped (a small percentage) with Mg, the a and c lattice parameters were measured to be 3.2822–5.3602 Å [155]. Suggestions have been made that the c parameter of implanted GaN layers increases after implantation and languishes after annealing [156]. However, the a parameter could not be precisely measured because sharp off-normal diffraction peaks are needed to determine this parameter accurately.

For the zinc blende polytype, the calculated lattice constant, based on the measured Ga−N bond distance in Wz GaN, is $a = 4.503$ Å. The measured value for this polytype varies between 4.49 and 4.55 Å, while that in Ref. [18] is 4.511 Å, indicating that the calculated result lies within the acceptable limits [157]. A high-pressure phase transition from the Wz to the rock salt structure has been predicted and observed experimentally. The transition point is 50 GPa and the experimental lattice constant in the rock salt phase is $a_0 = 4.22$ Å. This is slightly different from the theoretical result of $a_0 = 4.098$ Å obtained from first-principles nonlocal pseudopotential calculations [158].

Tables 1.6 and 1.10 compile some of the known properties of Wz GaN. Parameters associated with electrical and optical properties of Wz GaN are tabulated in Table 1.11. The same parameters associated with the zinc blende phase of GaN are tabulated in Table 1.12.

The bulk modulus of Wz GaN, which is the inverse of compressibility, is an important material parameter. Various forms of X-ray diffraction with the sample being under pressure can be used to determine the lattice parameters. Once the

lattice parameters are determined as a function of pressure, the pressure dependence of the unit cell volume can be obtained and fitted with an *equation of state* (EOS), such as the Murnaghan's EOS [159], and based on the assumption that the bulk modulus has a linear dependence on the pressure:

$$V = V_0\left(1 + \frac{B'P}{B_0}\right)^{-1/B'}, \tag{1.10}$$

where B_0 and V_0 represent the *bulk modulus* and the unit volume at ambient pressure, respectively, and B' the derivative of B_0 versus pressure. X-ray diffraction leads to the determination of the isothermal bulk modulus, whereas the Brillouin scattering leads to the adiabatic one. Nevertheless, in solids other than molecular solids, there is no measurable difference between the two thermodynamic quantities [160].

The bulk modulus (B) of Wz GaN has been calculated from first principles [161] and the first-principle orthogonalized *linear combination of atomic orbitals* (LCAO) method [158], leading to the values of 195 and 203 GPa, respectively. Another estimate for B is 190 GPa [158]. These figures compare well with the value of 194.6 GPa estimated from the elastic stiffness coefficient [79] and a measured value for 245 GPa [6].

The bulk modulus is related to the *elastic constants* through

$$B = \frac{(C_{11} + C_{12})C_{33} - 2C_{13}^2}{C_{11} + C_{12} + 2C_{33} - 4C_{13}} \tag{1.11}$$

and the range of bulk modulus values so determined is from about 173 to 245 GPa [160].

Using the room-temperature elastic constants of single-crystal GaN calculated by Polian *et al.* [38] yields an adiabatic bulk modulus, both *Voigt and Reuss* averages, of 210 GPa [91].

Earlier experimental investigations of the elastic constants of Wz GaN were carried out by Savastenko and Sheleg [162] using X-ray diffraction in powdered GaN crystals. The estimates of the *Poisson's ratio* from the early elastic coefficients ($\nu = C_{13}/C_{11} + C_{12}$) [162] and its measured [26] values of 0.372 (for $\nu\langle 0001\rangle = (\Delta a/a_{\mathrm{relax}})/(\Delta c/c_{\mathrm{relax}})$) and 0.378 (for $\nu\langle 0001\rangle = (\Delta a/a_0)/(\Delta c/c_0)$), respectively, are in good agreement (to avoid confusion the R value is defined as $R = -2C_{31}/C_{33}$). The experiments were performed on GaN layers on sapphire substrates because of X-ray diffraction. However, the results obtained later point to a Poisson's ratio of more near 0.2 as tabulated in Table 1.6 and depend on crystalline direction. The Poisson's ratio for the ZB case can be calculated from the elastic coefficients for that polytype as ν or $\sigma_0 = (C_{12}/C_{11} + C_{12})$ leading to values of about 0.352 as tabulated in Table 1.8. The Poisson's ratio varies along different crystalline directions as tabulated in Table 1.13 for AlN. It should be noted that there is still some spread in the reported values of elastic stiffness coefficients, as discussed in detail in the polarization sections of Section 2.12. More importantly, Kisielowski *et al.* [39] pointed out that expression

$$(\nu - 1)\langle 0001\rangle = (\Delta a/a_{\mathrm{relaz}})/(\Delta c/c_{\mathrm{relax}}), \tag{1.12}$$

where $\Delta a = a_{meas} - a_{relax}$ and $\Delta c = c_{meas} - c_{relax}$, should be used to calculated the Poisson's ratio, ν. Doing so leads to a Poisson's coefficient of $\nu_{GaN} = 0.2$–0.3.

Chetverikova *et al.* [163] measured the *Young's modulus* and Poisson's ratio of their GaN films. From the elastic stiffness coefficients, Young's modulus $E_{\langle 0001 \rangle}$ is estimated to be 150 GPa [157,162]. Sherwin and Drummond [164] predicted the elastic properties of ZB GaN on grounds of values for those Wz GaN samples reported by Savastenko and Sheleg [162]. The elastic stiffness coefficients and the bulk modulus are compiled in Table 1.24. Considering the wide spread in the reported data more commonly used figures are also shown.

Wagner and Bechstedt [178] calculated the elastic coefficients of Wz GaN using a pseudopotential plane wave method and pointed out the discrepancies among the results from different calculations and measurements tabulated in Table 1.24. It is argued that reliable values produce $2C_{13}/C_{33} = 0.50$–0.56 and $\nu = 0.20$–0.21 [178]. The agreement between *ab initio* calculations [42,178] and some measure-

Table 1.24 Experimental and calculated elastic coefficients (C_{ij}), bulk modulus (B) and its pressure derivative (dB/dP), and Young's modulus (E or Y_0) and (in GPa) of Wz GaN and ZB GaN (in part from Ref. [160]).

Technique	C_{11}	C_{12}	C_{13}	C_{33}	C_{44}	B_0	B'	E
X-ray [162]	296	130	158	267	24.1	195		150
XAS						245	4	
EDX						188	3.2	
ADX						237	4.3	
Brillouin [38]	390	145	106	398	105	210		356
Brillouin	374	106	70	379	101	180		
Brillouin [166]	365	135	114	381	109	204		329
Brillouin [28]	373	141	80.4	387	94	192		362
Brillouin [169]	315	118	96	324	88	175		281
Brillouin [170]	373	141	80	387	94	192		362
Ultrasonic [171]	377	160	114	209	81.4	173		161
Ultrasonic [165]	370	145	110	390	90	208		343
Single crystal X-ray						207		
Most commonly used values	380	110			105			
PWPP [42]	367	135	103	405	95	202		363
FP-LMTO [165]	396	144	100	392	91	207		355
Kim [168]	431	109	64	476	126	201		461
PWPP (Wagner)	C_{11}	515–C_{11}	104	414		207		373
ZB GaN	253–264	153–165			60–68	200–237	3.9–4.3	

The room-temperature elastic constants of single-crystal GaN have been determined by Polian *et al.* [38] yielding an adiabatic bulk modulus, both Voigt and Reuss, averages, of 210 GPa. The term $B' = dB/dP$ represents the derivative of B_0 versus pressure. EDX: energy dispersive X-ray; ADX: angular dispersive X-ray diffraction; XAS: X-ray absorption spectroscopy; PWPP: plane wave pseudopotential; FP-LMTO: full-potential linear muffin–tin orbital.

ments [38,165,166] is satisfactory. However, several calculations [167,168] and measurements [28,169–171] suffer from deviations in one or more of the values of elastic constants. The results from Savastenko and Sheleg [162] show excessive deviation for all the elastic constants and, therefore, should be avoided completely. The results from surface acoustic wave measurements of Deger *et al.* [165] on epitaxial epilayers have been corrected for piezoelectric stiffening and, therefore, are among the most reliable.

The vibrational properties of nitrides can best be described within the realm of mechanical properties. These vibrations actually serve to polarize the unit cell [172]. Phonons can be discussed under mechanical and optical properties. Here an arbitrary decision has been made to lump them with the mechanical properties of the crystal. Using GaN as the default, a succinct discussion of vibrational modes, some of which are active Raman modes, some are active in infrared (IR) measurements, and some are optically inactive called the silent modes, is provided [173]. Vibrational modes, which go to the heart of the mechanical properties, are very sensitive to crystalline defects, strain, and dopant in that the phonon mode frequencies and their frequency broadening can be used to glean very crucial information about the semiconductor. The method can also be applied to heterostructures and strained systems. Electronic Raman measurements can be performed to study processes such as electron–phonon interaction in the CW or time-resolved schemes. Time-resolved Raman measurements as applied to hot electron and phonon processes under high electric fields have important implication regarding carrier velocities. A case in point regarding GaN is treated in this context in Volume 3, Chapter 3.

The wurtzite crystal structure has the $C_{6\nu}^{4}$ symmetry and the group theory predicts the existence of the zone center optical modes A_1, $2B_1$, E_1, and $2E_2$. In a more simplified manner, one can consider that the stacking order of the Wz polytype is AaBb while that for the ZB variety is AaBbCc. In addition, the unit cell length of the cubic structure along [1 1 1] is equal to the width of one unit bilayer, whereas that for the hexagonal structure along [0 0 0 1] is twice that amount. Consequently, the phonon dispersion of the hexagonal structure along [0 0 0 1] ($\Gamma \rightarrow$ A in the Brillouin zone) is approximated by folding the phonon dispersion for the ZB structure along the [1 1 1] ($\Gamma \rightarrow$ L) direction [174], as shown in Figure 1.12. Doing so reduces the TO phonon mode at the L point of the Brillouin zone in the zinc blende structure to the E_2 mode at the Γ point of the Brillouin zone in the hexagonal structure. This vibrational mode is denoted as E_2^H with superscript H depicting the higher frequency branch of the E_2 phonon mode. As indicated in the figure there is another E_2 mode at a lower frequency labeled as E_2^L. This has its genesis in zone folding of the transverse acoustic (TA) mode in the zinc blende structure. It should be noted that in the hexagonal structure there is anisotropy in the macroscopic electric field induced by polar phonons. As a result, both the TO and LO modes split into the axial (or A_1) and planar (or E_1) modes where atomic displacement occurs along the *c*-axis or perpendicular to the *c*-axis, respectively. This splitting is not shown in Figure 1.12 as it is very small, just a few meV, near zone center; phonon dispersion curves for GaN including the splitting of the A_1 and E_1 modes can be found in Volume 3, Figure 3.84.

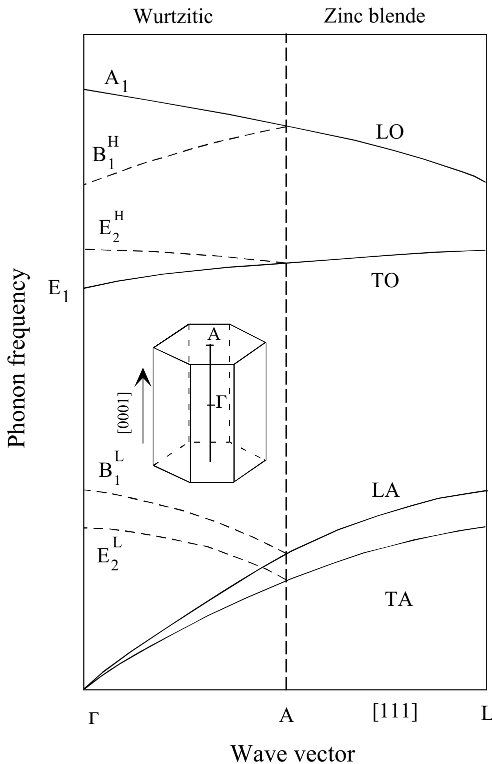

Figure 1.12 Schematic depiction of the phonon dispersion curves for ZB and Wz structures. Also shown are the Γ and A points of the zone in relation to the real space hexagonal structure. Phonon branches along the [1 1 1] direction in the ZB structure are folded to approximate those of the wurtzite structure along the [0 0 0 1] direction, because the unit cell length of the cubic structure along the [1 1 1] direction is equal to the width of one unit bilayer, while that for the hexagonal structure along the [0 0 0 1] directions is twice that amount. Patterned after Ref. [174].

As discussed below, in the context of hexagonal structures, group theory predicts eight sets of phonon normal modes at the Γ point, namely $2A_1 + 2E_1 + 2B_1 + 2E_2$. Among them, one set of A_1 and E_1 modes are acoustic, while the remaining six modes, namely $A_1 + E_1 + 2B_1 + 2E_2$, are optical modes. As shown in Figure 1.12, one A_1 and one B_1 mode (B_1^H) derive from a singly degenerate LO phonon branch of the zinc blende system by zone folding, whereas one E_1 and one E_2 mode (E_2^H) derive from a doubly degenerate TO mode in the cubic system.

The first-order phonon Raman scattering is due to phonons near the Γ point zone center, that is, with wave vector $k \approx 0$, because of the momentum conservation rule in the light scattering process. Raman measurements typically are employed to probe the vibrational properties of semiconductors. When performed along the direction perpendicular to the *c*-axis or the (0 0 0 1) plane, the nomenclature used to describe this configuration is depicted as $Z(XY, XY)\overline{Z}$. Here, following Porto's notation [175] A(B, C)D is used to describe the Raman geometry and polarization, where A and D

represent the wave vector direction of the incoming and scattered light, respectively, whereas B and C represent the polarization of the incoming and scattered light. In Raman scattering, all the above-mentioned modes, with the exception of B_1 modes, are optically active. Because of their polar nature, the A_1 and E_1 modes split into longitudinal optical (A_1-LO and E_1-LO) meaning beating along the *c*-axis, and transverse optical (A_1-TO and E_1-TO), meaning beating along the basal plane. To reiterate, the A_1 and B_1 modes give atomic displacements along the *c*-axis, while the others, E_1 and E_2, give atomic displacements perpendicular to the *c*-axis, meaning on the basal plane. Here, the A_1 and E_1 modes are both Raman and IR active whereas the two E_2 modes are only Raman active and the two B_1 modes are neither Raman nor IR active, meaning silent modes. In the $Z(XY, XY)\overline{Z}$ configuration, only the E_2^1 (or E_2^L or E_2 low), E_2^2 (or E_2^H or E_2 high), and A_1(LO) modes should be observable. In particular, in $Z(X, X)\overline{Z}$ and $Z(Y, Y)\overline{Z}$ geometries, all three modes are observable, while in $Z(X, Y)\overline{Z}$ or $Z(Y, X)\overline{Z}$ geometries only E_2 modes are detected [175]. The details of the mode–Raman configuration relationship are tabulated in Table 1.25. Shown in Figure 1.13 are the modes in the Raman backscattered geometries in relation to hexagonal crystalline orientation that can be used to sense the various phonon modes indicated.

The acoustic modes, which are simple translational modes, and the optical modes for wurtzite symmetry are shown in Figure 1.14. The calculated phonon dispersion curves [57] for GaN are shown in Figure 1.15. There is another way to describe the number of vibrational modes in zinc blende and wurtzitic structures, which is again based on symmetry arguments. In the wurtzite case [66], the number of atoms per unit cell $s = 4$, and there are total of 12 modes, the details of which are tabulated in Table 1.26. This table also holds for the zinc blende polytypes with $s = 2$. This implies a total of six modes in zinc blende as opposed to 12 in wurtzite, three of which are acoustical (1 LA and 2 TA) and the other three are optical (1 LO and 2 TO) branches. These phonon modes for a wurtzite symmetry, specifically the values for wurtzite GaN, are listed in Table 1.27 obtained from Refs [56,157,176,177] along with those obtained from first-principles pseudopotential calculations [161,178]. Also listed are TO and LO optical phonon wave numbers of ZB GaN [25,179].

Table 1.25 Raman measurement configuration needed to observe the phonon modes in hexagonal nitrides.

Mode	Configuration
A_1(TO), E_2	$X(Y, Y)\overline{X}$
A_1(TO)	$X(Z, Z)\overline{X}$
E_1(TO)	$X(Z, Y)\overline{X}$
E_1(TO), E_1(LO)	$X(Y, Z)Y$
E_2	$X(Y, Y)Z$
E_2	$Z(Y, X)\overline{Z}$
A_1(LO), E_2	$Z(Y, Y)\overline{Z}$

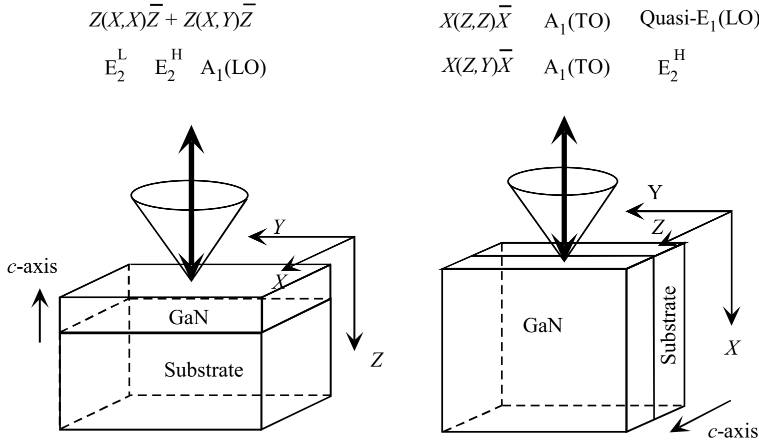

Figure 1.13 Schematic representation of two Raman configurations with incident and scattered light directions in the backscattering geometry for $Z(X,X)\overline{Z}+Z(X,Y)\overline{Z}$ configuration to sense E_2^L, E_2^H, and A_1(LO) modes, $X(Z,Z)\overline{X}$ configuration to sense A_1(TO) and quasi-E_1(LO) modes, and $X(Z,Y)\overline{X}$ configuration to sense A_1(TO) and E_2^H modes.

Owing to the presence of elastic strain, thin epilayers have different phonon energies compared to the bulk samples. In the general case, strain can give rise to a shift and splitting of phonon modes. However, for uniaxial strain along the *c*-axis or biaxial strain in the *c*-plane, the crystal retains its hexagonal symmetry resulting in only a shift of the phonon frequencies. The strain effects on GaN optical phonon energies have been studied experimentally [181] and theoretically [178]. Within a perturbative approach, the change in the frequency of a given phonon λ under symmetry-conserving stress can be expressed in terms of the two strain components, ε_{xx} and ε_{zz}, representing perpendicular and parallel to the *z*-axis, respectively, as $\Delta\Omega_\lambda = 2\,a_\lambda\varepsilon_{xx} + b_\lambda\varepsilon_{zz}$, where a_λ and b_λ are the corresponding deformation potential constants. The derivation of strain values from the Raman measurements of phonon frequencies is straightforward, once the phonon deformation potentials are known. Davydov *et al.* [181] combined high-resolution X-ray diffraction (HRXRD) measurements and Raman spectroscopy results to determine the phonon deformation potentials in GaN epitaxial layers grown on 6H-SiC. The strain components were obtained by comparing the lattice constants of the epitaxial layers with those of the strain-free GaN ($a_0 = 3.1880$ Å, $c_0 = 5.18\,561$ Å). The Raman spectrum of a strain-free 300 μm thick GaN layer grown on sapphire was used as a reference. Also, using their relation to the hydrostatic pressure coefficients [6] through the bulk elastic coefficients, the sets of phonon deformation potentials were derived for most of zone center optical phonons. As seen in Table 1.27, except for the A_1-TO mode, the phonon energies and the deformation potentials reported by Davydov *et al.* [181] agree well with the pseudopotential plane wave calculations reported by Wagner and Bechstedt [178]. Wagner and Bechstedt argue that the published conversion factors

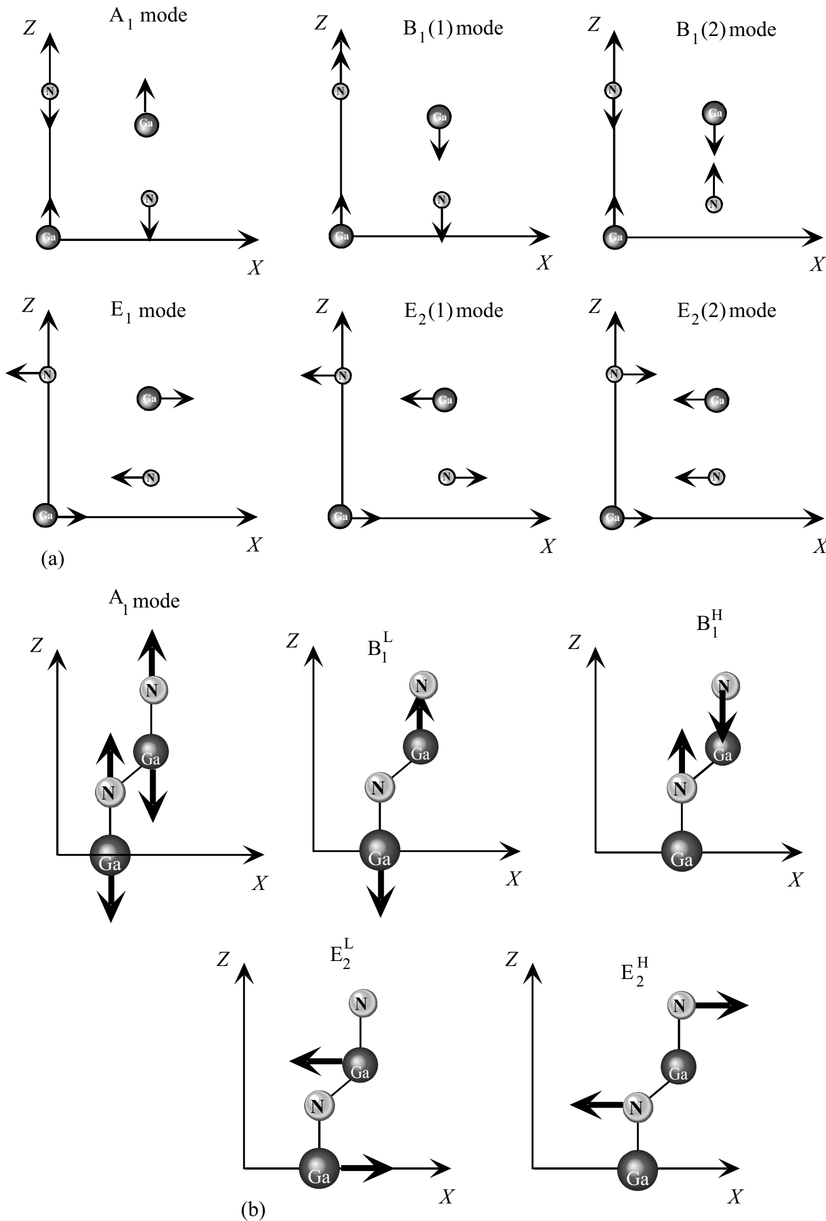

Figure 1.14 Atomic vibrations in Wz GaN. The larger atom represents Ga while the smaller one is for N. $X = (1\,0\,0)$, $Y = (0\,1\,0)$, and $Z = (0\,0\,1)$ represent the optical polarization directions: (a) for general wave vector and (b) for zone center phonons.

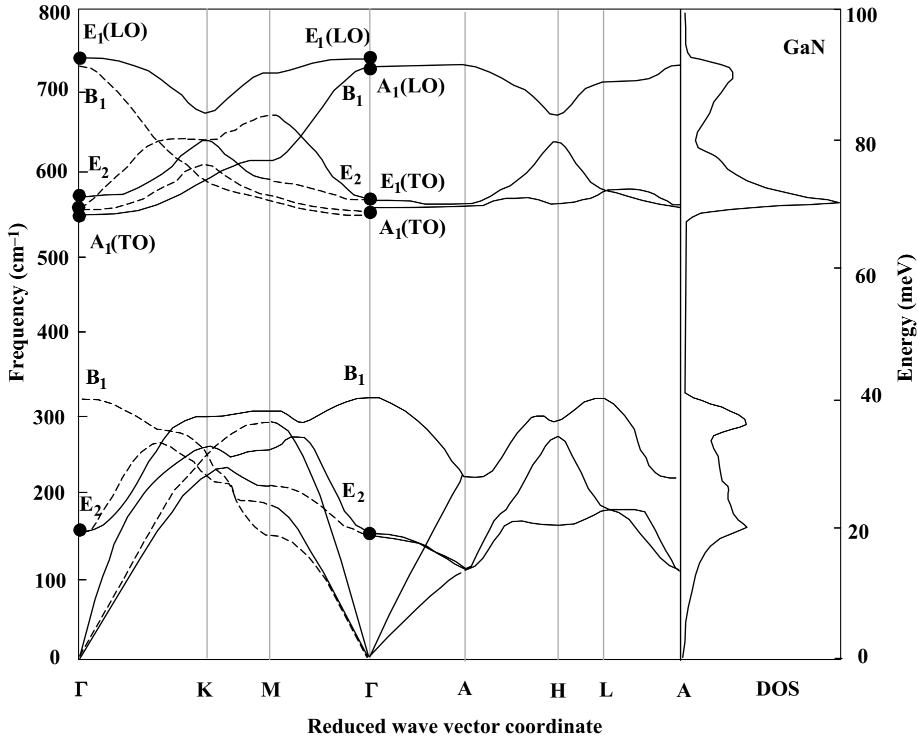

Figure 1.15 Calculated phonon dispersion curves and phonon density of states for hexagonal bulk GaN. The solid and dashed lines correspond to the Λ_1(or T_1) and Λ_2 (or T_2) irreducible representations (following Ref. [180]), respectively. Note how close the E_1(LO) and A_1(LO) modes are, making high-quality samples with sharp modes imperative for their experimental delineation [169].

Table 1.26 Acoustic and optical phonon modes in a crystal with wurtzite symmetry such as GaN, AlN, and InN, where *s* represents the number of atoms in the basis.

Mode type	Number of modes
LA	1
TA	2
Total acoustic modes	3
LO	$s-1$
TO	$2s-2$
All optical modes	$3s-3$
All modes	$3s$

The *s* parameter for wurtzite symmetry is 4. This table is also applicable to the zinc blende case but with $s=2$.

Table 1.27 (a) Zone center optical phonon wave numbers (in units of cm^{-1}) of GaN obtained from Raman scattering at 300 K compiled by Akasaki and Amano [157] (Wz) and Huang *et al*. [177] (Wz template). Also shown are the calculated values. (b) Measured phonon wave numbers (in units of cm^{-1}) for wurtzitic GaN. (c) Zinc blende phase phonon wave numbers for zinc blende GaN [179] (theory [59]).

(a)

					Deformation potentials – Wz			
			Wz relaxed		Raman [181]		Calculated [178]	
Phonon mode	**Wz [157,177]**	**Wz template [177]**	**[169]**	**Wz unstrained (calculated) [178]**	a_λ	b_λ	a_λ	b_λ
E_1-TO	556–559	558.5	558.8	568	-820 ± 25	-680 ± 50	−717	−591
A_1-TO	533–534	532.5	531.8	540	-630 ± 40	-1290 ± 80	−640	−695
E_1-LO	741–741	745.0	741	757			−775	−703
A_1-LO	710–735	737.0	734	748			−664	−695
E_2^L	143–146		144	142	115 ± 25	-80 ± 35	75	4
E_2^H	560–579		567.6	576	-850 ± 25	-920 ± 60	−742	−715
B_1^L				337			−334	−275
B_1^H				713			−661	−941

Table 1.27 (*Continued*)

(b)

Phonon mode	Wz unstrained (measured) (collected in Refs [174,178], but based on Refs [6,169])
E_1-TO	558.8
A_1-TO	531.8
E_1-LO	741
A_1-LO	741
E_2^L	144
E_2^H	567.6
B_1^L	
B_1^H	

(c)

Mode		Mode		
LO(Γ) (cm^{-1})	748 [59]	LO(L) (cm^{-1})	675 [59]	
TO(Γ) (cm^{-1})	562 [59]	TO(L) (cm^{-1})	554 [59]	
LO(X) (cm^{-1})	639 [59]	LA(L) (cm^{-1})	296 [59]	
TO(X) (cm^{-1})	558 [59]	TA(L) (cm^{-1})	144 [59]	
LA(X) (cm^{-1})	286 [59]	TO (cm^{-1})	558 [179]	560 [58]
TA(X) (cm^{-1})	207 [59]	LO (cm^{-1})	730 [179]	750 [58]

GaN on sapphire, about 50–70 μm thick, at 300 K.

between the luminescence or Raman shifts and the corresponding biaxial stress are seldom directly measured data. They are either obtained using elastic constants or are constructed from deformation potentials, which have been obtained by means of additional hydrostatic pressure coefficients. Owing to these varying procedures and different sets of parameters used to extract the conversion coefficients from the raw experimental data, discrepancies in the experimental reports of deformation potentials are present.

1.2.3 Thermal Properties of GaN

The lattice parameter of semiconductors depends on temperature and is quantified by *thermal expansion coefficient* (TEC), which is defined as $\Delta a/a$ or α_a and $\Delta c/c$ or α_c, for in-plane and out-of-plane configurations, respectively. It depends on stoichiometry, extended defects, and free-carrier concentration. As in the case of the lattice parameter, a scatter exists in TEC particularly for nitrides as they are grown on foreign substrates with different thermal and mechanical properties. Measurements made over the temperature range of 300–900 K indicate the mean coefficient of thermal expansion of GaN in the *c*-plane to be $\Delta a/a = \alpha_a = 5.59 \times 10^{-6}\,\mathrm{K}^{-1}$. Similarly, measurements over the temperature ranges of 300–700 and 700–900 K, respectively, indicate the mean coefficient of thermal expansion in the *c*-direction to be $\Delta c/c = \alpha_c = 3.17 \times 10^{-6}$ and $7.75 \times 10^{-6}\,\mathrm{K}^{-1}$, respectively [140]. Sheleg and Savastenko [49] reported a TEC near 600 K for perpendicular and parallel to the *c*-axis of $4.52 \pm 0.5 \times 10^{-6}$ and $5.25 \pm 0.05 \times 10^{-6}\,\mathrm{K}^{-1}$, respectively. Leszczynski and Walker [182] reported α_a values of 3.1 and 6.2 $10^{-6}\,\mathrm{K}^{-1}$ for the temperature ranges of 300–350 and 700–750 K, respectively. The α_c values in the same temperature ranges, in order, were 2.8 and 6.1 $10^{-6}\,\mathrm{K}^{-1}$.

In a similar vein, GaN and other allied group III nitride semiconductors are grown at high temperatures and also subjected to increased junction temperatures during operation of devices such as amplifiers and light emitting devices. As such, the structures are subjected to thermal variations as well. In this context, it is imperative to have knowledge of the thermal expansion coefficients, which are termed as TEC. Assuming that these figure remain the same with temperature, the linear expansion coefficients for the *a* and *c* parameters are tabulated in Tables 1.10 and 1.28 for heteroepitaxial GaN. However, it is instructive to know the temperature dependence of these parameters, which is shown in Figure 1.16.

Being grown on various substrates with different thermal expansion coefficients leads to different dependencies of the lattice parameter on temperature. Temperature dependence of GaN lattice parameter has been measured for a bulk crystal (grown at high pressure) with a high free-electron concentration ($5 \times 10^{19}\,\mathrm{cm}^{-3}$), a slightly strained homoepitaxial layer with a low free-electron concentration (about $10^{17}\,\mathrm{cm}^{3}$), and a heteroepitaxial layer (also with a small electron concentration) on sapphire [88]. The results of such study are tabulated in Table 1.28.

It can be seen that the bulk sample with a high free-electron concentration exhibits a thermal expansion that is about 3% higher as compared to the homoepitaxial layer.

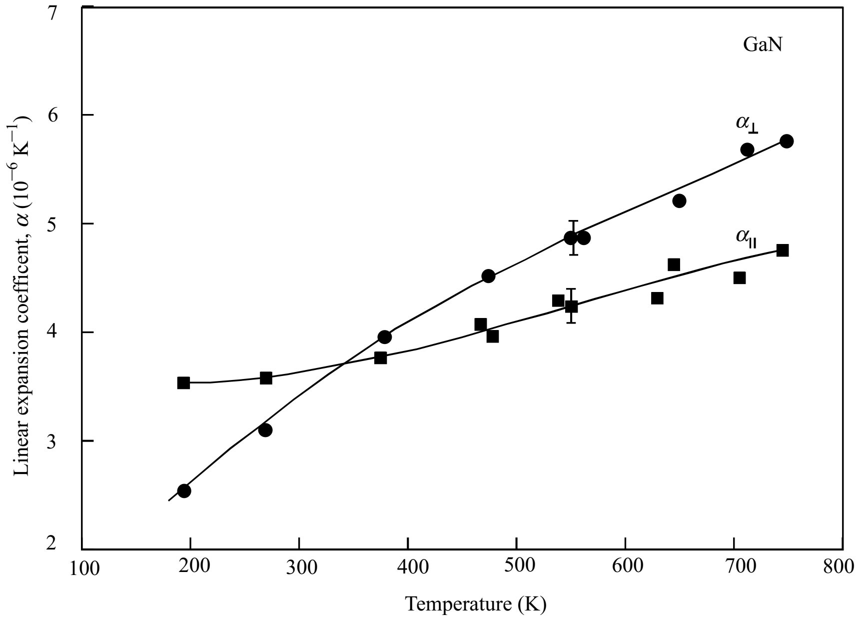

Figure 1.16 Wz GaN coefficient of linear thermal expansion versus temperature for basal plane ($\alpha_{||}$), *a* parameter, and out of the basal plane ($\alpha_\perp$), *c* parameter, directions [49].

As for the case of the heteroepitaxial layer on sapphire, the thermal expansion of the substrate affects the dependence of the lattice parameter on temperature.

Various spectroscopic techniques, such as Auger electron spectroscopy, X-ray photoemission spectroscopy (XPS), and electron energy loss spectroscopy (EELS) have been very useful for the study of surface chemistry of GaN. Building on earlier investigations of the thermal stability of GaN by Johnson *et al.* [139] and employing

Table 1.28 Lattice parameters for GaN samples at various temperatures (lattice parameters *c* were measured with accuracy of 0.0002 Å, lattice parameter *a* with accuracy of 0.0005 Å) [88].

T (K)	GaN bulk, $n = 5 \times 10^{19}$ cm^{-3}		Homoepitaxial GaN on conductive GaN substrate		GaN on sapphire	
	c (Å)	*a* (Å)	*c* (Å)	*a* (Å)	*c* (Å)	*a* (Å)
20	5.1836	3.1867	5.1822	3.1867		
77	5.1838	3.1868	5.1824	3.1868	5.1846	3.1842
295	5.1860	3.1881	5.1844	3.1881	5.1865	3.1859
500	5.1885	3.1903	5.1870	3.1903	5.1888	3.1886
770	5.1962	3.1945	5.1944	3.1945	5.1952	3.1941

the aforementioned techniques, the thermal stability and dissociation of GaN have been examined further. As indicated earlier, the materials characteristics depend, to a large extent, on defects and impurities, which in turn depend somewhat on growth conditions. Because of this the materials, obtained from various sources, studied in various laboratories exhibit different characteristics. This led to inconsistent results from different laboratories. While some experimental studies on GaN stability conducted at high temperatures suggested that significant weight losses occur at temperatures as low as 750 °C, others contradicted this proposition and suggested that no significant weight loss should occur even at a temperature of 1000 °C. Sime and Margrave [183] followed the investigation by Johnson *et al.* [139] by studying the evaporation of GaN and Ga metal in the temperature range 900–1150 °C under atmospheric pressure in N_2, NH_3, and H_2 environments with an emphasis on the formation and decomposition equilibrium.

The *heat of evaporation* was determined and the existence of $(GaN)_x$ polymers in the gas phase was suggested. Morimoto [184] and Furtado and Jacob [185] observed that GaN is less stable in an HCl or H_2 atmosphere than in N_2. Some controversy exists regarding the process steps that dictate the decomposition of GaN. Using mass spectroscopy, Gordienko *et al.* [186] noted that $(GaN)_2$ dimers are the primary components of decomposition. Others [187,188] found only $N_2{}^+$ and Ga^+ to be the primary components in the vapor over GaN. On the basis of measurements of the apparent vapor pressure, Munir and Searcy [189] calculated the *heat of sublimation* of GaN to be 72.4 ± 0.5 kcal mol^{-1}. Thurmond and Logan [190] determined the equilibrium N_2 pressure of GaN as a function of temperature by measuring the partial pressure ratios existing in a (H_2CNH_3) gas mixture streaming over Ga and GaN. Thermal stability of GaN was taken up later by Karpinski *et al.* [191] with a detailed investigation of the problem at high temperatures and under pressure up to 60 kbar by employing a tungsten carbide anvil cell activated by a gas pressure technique.

The bond strength in gallium nitride is high with bonding energy of 9.12 eV/molecule [192], particularly as compared to the more conventional semiconductors such as GaAs, which has a bonding energy of 6.5 eV/atom pair. As a result, the free energy of GaN is very low in relation to the reference states of the free N and Ga atoms. However, the N_2 molecule is also strongly bonded with 4.9 eV/atom. Therefore, the free energies of the constituents of GaN (Ga and N_2) at their normal states are close to that of the GaN crystal as illustrated in Figure 1.17, where the free energy of GaN (1 mol) and the free energy of the sum of its constituents ($Ga + 1/2N_2$) are shown as a function of temperature and N_2 pressure. As the temperature increases, the Gibbs free energy, $G(T)$, of the constituents decreases faster than $G(T)$ of the GaN crystal. More importantly, GaN becomes thermodynamically unstable at high temperatures. The crossing of $G(T)$ curves determines the equilibrium temperature where GaN coexists with its constituents at a given N_2 pressure. The application of pressure increases the free energy of the constituents more than $G(T)$ of the GaN crystal, which causes the equilibrium point to shift to higher temperatures, increasing the range of GaN stability.

The data on phase diagrams of GaN are limited and contradictory by reason of high *melting temperatures* (T_m) and high *nitrogen dissociation pressures* ($P_{N_2}^{dis}$). Dissociation

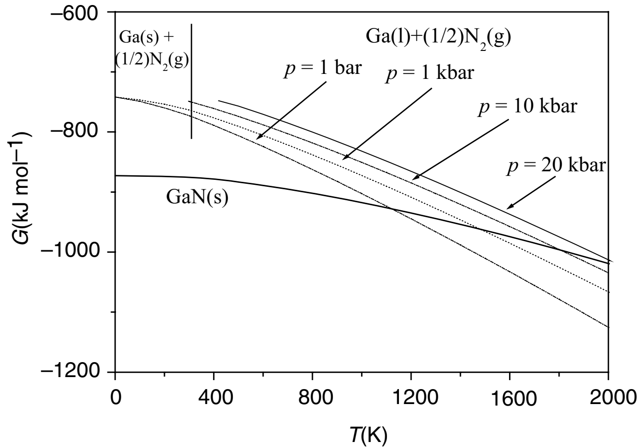

Figure 1.17 Gibbs free energy of GaN and its constituents as a function of temperature and pressure [192].

pressure of MN, where M stands for Al, Ga, and In, and N for nitrogen, is defined as the nitrogen pressure at the thermal equilibrium of the reaction [193]: MN(s) = M(l) + $1/2N_2$(g), where s, l, and g stand for solid, liquid, and gas states, respectively. Reported values for $P^{dis}_{N_2}$ for GaN [193] show large discrepancies [191,194]. Specifically, in the high-pressure range, the partial pressure, p, versus the inverse temperature, $1/T$, curve of Karpinski *et al.* deviates markedly from the linear dependence proposed by Thurmond and Logan as shown in Figure 1.18. Despite the discrepancies, there is a good agreement in the Gibbs free energy with ΔG^0 $32.43T - 3.77 \times 10^4 \pm 700\,\text{cal mol}^{-1}$ for GaN synthesis between the two references. The value of enthalpy ΔH^0 ($-37.7\,\text{kcal mol}^{-1}$) is in good agreement as well with that estimated by Madar *et al.* [194].

The stars in Figure 1.18 indicate the melting point of AlN at $T^M_{AlN} = 3487$ K, GaN at $T^M_{GaN} = 2791$ K, and InN at $T^M_{InN} = 2146$ K. The GaN and InN melting points so indicated may underestimate the real values, as perhaps a sufficient overpressure was not maintained. Line fits correspond to $8.3 \times 10^9 \exp(-5.41\,\text{eV}/kT)$, 1.5×10^{14} $\exp(-3.28\,\text{eV}/kT)$, and $7.9 \times 10^{17} \exp(-2.78\,\text{eV}/kT)$ bar for AlN, GaN, and InN, respectively. The data over the larger temperature range are those compiled by Ambacher [196]. The results of Madar *et al.* [194], Thurmond and Logan [190], and Karpinski *et al.* [191] are also shown in a limited temperature range. For GaN (see Figure 1.18), the nitrogen dissociation pressure equals 1 atm at approximately 850 °C and 10 atm at 930 °C. At 1250 °C, GaN decomposed even under pressure of 10 000 bar of N_2. The turning over of the partial pressure for GaN and InN at temperatures approaching the melting point may need to be reexamined. What is clear, however, is that GaN and particularly InN have very high partial pressures that make it imperative to maintain high fluxes of N during growth. It should, therefore, come as no surprise that the incorporation of nitrogen is not a trivial problem at high temperatures. For the pressures below equilibrium at a given temperature, the thermal dissociation occurs at a slow and apparently constant rate suggesting a diffusion-controlled

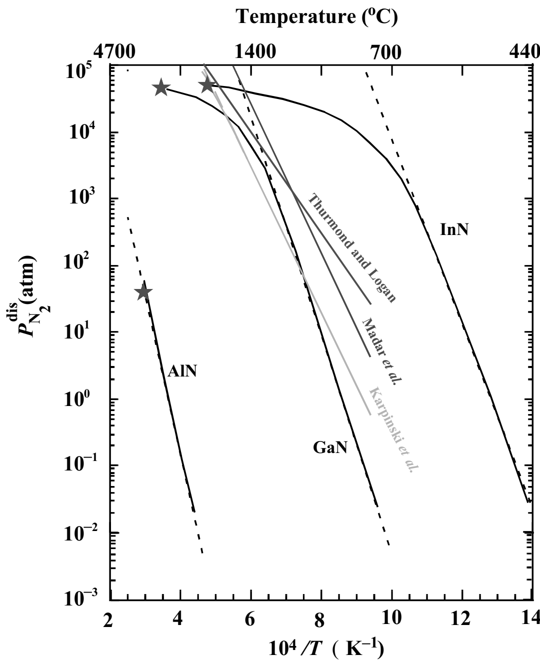

Figure 1.18 Equilibrium N_2 pressure over the MN(s) + M(l) systems corresponding to GaN (M = Al, Ga, In) reported and/or compiled by Slack and McNelly[195], Madar *et al.* [194], Thurmond and Logan [190], Karpinski *et al.* [191], and Ambacher [196]. The melting points of the three binaries are indicated by stars. The desorption activation energies, E_{MN}, determined by straight line fits to the data points are 3.5 eV (336 kJ mol^{-1}), 3.9 eV (379 kJ mol^{-1}), and 4.3 eV (414 kJ mol^{-1}) for InN, GaN, and AlN, respectively. Caution should be exercised as there is significant deviation from the activation line for GaN and InN. This may simply be a matter of not being able to maintain sufficient pressure on GaN and InN at very high temperatures to reach the real melting point.

process of dissociation. Expanded equilibrium vapor pressure data inclusive of GaAs and InP in addition to the three nitride binaries reported by Matsuoka [197] are shown in Figure 1.19. Melting points and other thermodynamic characteristics of III-N compounds are given in Tables 1.10, 1.16, and 1.20 as compiled by Popovici and Morkoç [198] as well as those collected from various sources as indicated in the pertinent tables.

Investigations utilizing epitaxial thin films of GaN, as well as AlN and InN, have been conducted by Ambacher *et al.* [199], who heated the samples in vacuum and recorded the partial pressure of relevant gases with a quadrupole mass spectrometer. Desorption spectra were then analyzed [200] to find the binding energies of various desorbed species as well as the thermal stability of the sample for a given thermal treatment. As expected, the nitrogen partial pressure increases exponentially above $T_E = 850\,°C$ for GaN underscoring the point that the decomposition temperature in vacuum is much lower than the melting point shown in Figure 1.18. The rate of

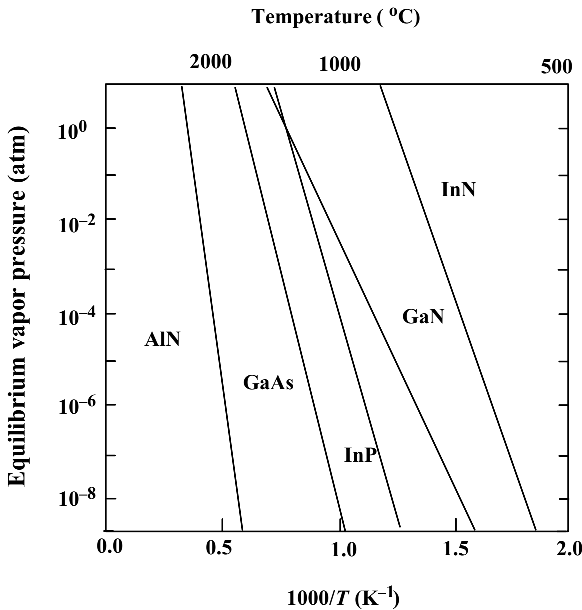

Figure 1.19 Equilibrium vapor pressure of N_2 over AlN, GaN and InN, the sum of As_2 and As_4 over GaAs, and the sum of P_2 and P_4 over InP [197].

nitrogen evolution Φ(N) was set equal to the rate of decomposition, and the slope of ln [Φ(N)] versus $1/T$ gives the effective activation energy of the decomposition in vacuum as compared to those shown in Figure 1.18. The decomposition rate equals the desorption of one monolayer every second ($\Phi_N = 1.5 \times 10^{15}\,\text{cm}^{-2}\,\text{s}^{-1}$) at 970 °C, and the activation energy of the thermally induced decomposition is determined to be $E_{MN} = 3.9$ eV (379 kJ mol^{-1}) for GaN.

Despite some disagreement, as mentioned above, investigations of the equilibrium nitrogen overpressure versus temperature, P_{N_2}–T, for GaN [92,190,201], including a very complete and consistent set of data obtained by Karpinski *et al.* [191,202] have set the stage for bulk template growth as well as setting benchmarks for growth of GaN by nonequilibrium methods. Those authors employed direct synthesis and decomposition experiments and used the gas pressure technique (for pressures up to 20 kbar) and the high-pressure anvil method beyond the reach of gas pressure technique (up to 70 kbar). The results of these experiments are shown in Figure 1.20 [203,204]. The message in the form of N_2 partial pressure is that one must stay below the decomposition curve. This means that the selection of GaN synthesis temperature directly depends on the pressure that the vessel can provide. For example, if a pressure of 20 kbar is all that is available, then the temperature should be kept below about 1660 ° C. For a review of the stability of GaN as well as the growth GaN templates, the reader is referred to Ref. [192].

As alluded to earlier, nitride semiconductors in general and GaN in particular are considered for high-power/high-temperature electronic and optoelectronic devices

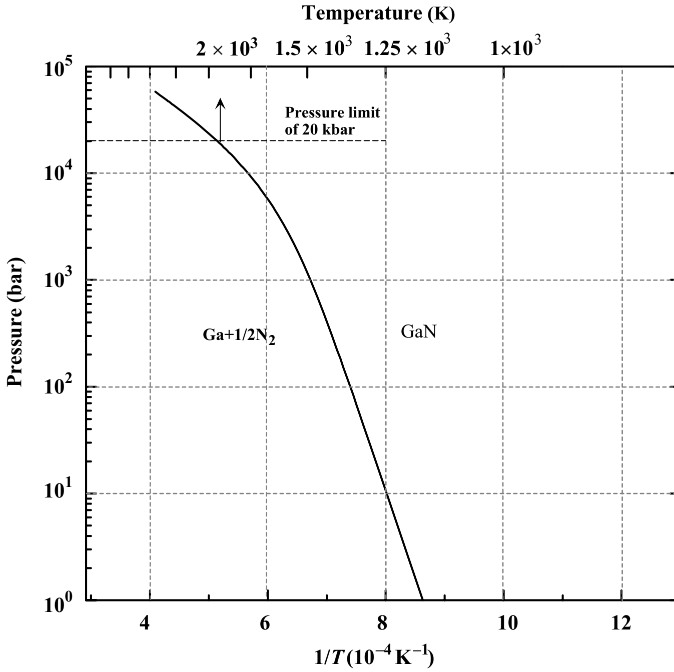

Figure 1.20 N_2 partial pressure as a function of temperature GaN. Ref. [192], originally in Refs [203,204].

where thermal dissipation is a key issue. Device applications assure that the *thermal conductivity* (κ) is an extremely important material property. Thermal conductivity is a kinetic property determined by contributions from the vibrational, rotational, and electronic degrees of freedom, and as such it is related to the mechanical properties of the material. However, for convenience, this property is generally categorized under the thermal properties of nitrides in this book. The electronic thermal conductivity contribution is negligible for carrier concentrations $\leq 10^{19}\,\text{cm}^{-3}$. The heat transport is predominantly determined by phonon–phonon Umklapp scattering, and phonon scattering by point and extended defects such as vacancies (inclusive of the lattice distortions caused by them), impurities, and isotope fluctuations (mass fluctuation) as elaborated on by Slack *et al.* [91]. For pure crystals, phonon–phonon scattering, which is ideally proportional to T^{-1} above the Debye temperature, is the limiting process.

The lattice contribution (phonon scattering) to the thermal conductivity, κ, in a pure solid is obtained from the kinetic theory as [205]

$$\kappa_{\text{lattice}}(T) = \frac{1}{3} v_{\text{s}} C_{\text{lattice}}(T) L(T), \tag{1.13}$$

where T is the temperature, v_{s} is the velocity of sound (nearly independent of temperature), $C_{\text{lattice}}(T)$ is the lattice specific heat, and $L(T)$ is the phonon mean free length. In nearly all materials, the thermal conductivity, $\kappa(T)$, first increases with temperature, reaches a maximum ($\kappa_{\max}$) at some characteristic temperature T_{ch}, and

then decreases. At low temperatures, L is relatively long and is dominated by extrinsic effects such as "defects" and/or finite crystal size and $C_{\text{lattice}}(T) \sim (T/\theta_D)^3$, where θ_D is the Debye temperature. As the temperature increases, $C_{\text{lattice}}(T)$ begins to saturate and the intrinsic temperature-dependent Umklapp processes become dominant, leading to a decrease in L.

The other contribution, the electronic contribution, to the thermal conductivity is negligible for carrier concentrations $\leq 10^{19}\,\text{cm}^{-3}$. It can be expressed as [206]

$$\kappa_{\text{electr}}(T) = \frac{\pi^2 n k_B^2 T \tau_{\text{electr}}}{3 m_c^*}, \tag{1.14}$$

where n is the carrier density, k_B is the Boltzmann constant, τ_{electr} is the scattering time of the electrons, and m_c^* is the conduction band effective mass.

The first measurements of κ of GaN were by Sichel and Pankove [207] on "bulk" GaN (400 μm of material grown by HVPE) as a function of temperature (25–360 K): $\kappa \cong 1.3\,\text{W cm}^{-1}\,\text{K}^{-1}$ (along the c-axis) at 300 K. This room-temperature value measured is a little smaller than the value of $1.7\,\text{W cm}^{-1}\,\text{K}^{-1}$ predicted in 1973 [77] and much smaller than the $\kappa \sim 4.10\,\text{W cm}^{-1}\,\text{K}^{-1}$ calculated by Witek [208]. Using the elastic constants reported by Polian *et al.* [38], Slack *et al.* [91] calculated a Debye temperature of 650 K, which led to a more recent thermal conductivity at 300 K for GaN of $\kappa = 2.27\,\text{W cm}^{-1}\,\text{K}^{-1}$, assuming that there is no isotope scattering in GaN. This is very close to the measured values in high-quality freestanding GaN samples, the electrical properties of which are discussed in Volume 2, Chapter 3 and optical properties of which are discussed in Volume 2, Chapter 5.

Using a steady-state four-probe method and a high-quality freestanding GaN template, Slack *et al.* [91] measured a value for κ of $2.3\,\text{W cm}^{-1}\,\text{K}^{-1}$ at room temperature, which increased to over $10\,\text{W cm}^{-1}\,\text{K}^{-1}$ at 77 K. The method holds for four-probe thermal measurement, where the term "four probe" is analogous to the four-probe electrical measurement method. Namely, a heater is attached on the end of the sample – sandwiched in a copper clamp so that the heat flows through the entire width of the sample, not just the surface –supplying a heat current Q (analogous to an electrical current I). Two thermocouple junctions are attached along the length of the specimen by two little copper clamps separated by a distance L, the schematic representation of which is shown in Figure 1.21.

The heat current Q creates a temperature gradient of ΔT across the wafer. The κ value is calculated using $\kappa = (P/\Delta T)(L/A)$, where P is the power (=voltage × current) supplied to the heater and A represents the cross-sectional area of the sample. Although the technique sounds simple, its accuracy depends very critically on making sure that the heat conduction is through the specimen and along the direction in which the temperature gradient is measured. To make certain that heat is transferred in the said direction only, the radiation losses must be minimized as well as making sure that the electrical wires used do not remove heat. To this end, the sample is placed in a turbo pumped vacuum to eliminate conduction and convection through the surrounding medium. Heat losses via conduction through the wires are minimized using long (10 cm), thin (<100 μm) wires of low thermal conductivity, typically chromel/constantan thermocouple and heater wires. Radiation losses are

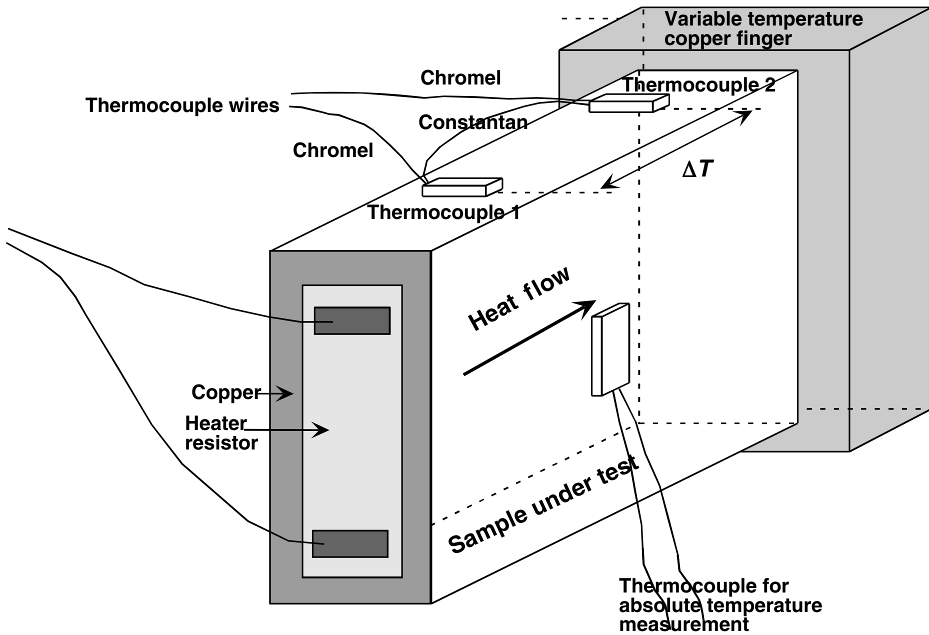

Figure 1.21 Schematic representation of the four-probe thermoelectric measurement setup used to measure the thermal conductivity of freestanding GaN [91].

minimized by surrounding the sample with a heat shield anchored thermally to the cold tip of the cryostat. By carefully designing this shield, Slack *et al.* [91] were able to reduce the total heat loss to the order of 1–2 mW K^{-1} at room temperature. Because the radiation losses follow T^3 dependence, they die off rather quickly below room temperature. For a sample with a thermal conductivity of 1 W cm^{-1} K^{-1}, cross section of 1×3 mm^2, and thermocouple probe separation of 5 mm, the thermal conductance is about 60 mW K^{-1}, so the heat losses are less than 5%. Fortunately, for wide bandgap semiconductors such as GaN the thermal conductivities are high enough so that the heat conduction is mainly through the sample, reducing the measurement error. Just as a reference point, for samples of lower thermal conductance (either lower conductivity or thinner), the heat losses can become important near room temperature. Thus, the samples for lower thermal conductivity materials (e.g., glasses or thermoelectric alloys) usually need to be short with large cross-sectional areas. The temperature-dependent thermal conductivity so measured for freestanding GaN is shown in Figure 1.22. From that temperature dependence and assuming the heat dissipation is through acoustic phonons, a *Debye temperature* of $\theta_D \approx 550$ K was deduced, which compares with 650 K reported by Slack *et al.* [91].

As can be seen in Figure 1.22, the measured thermal conductivity of GaN in the temperature range of 80–300 K has a temperature power dependence of -1.22. This slope is typical of pure adamantine crystals below the Debye temperature indicating acoustic phonon transport where the phonon–phonon scattering is a combination of

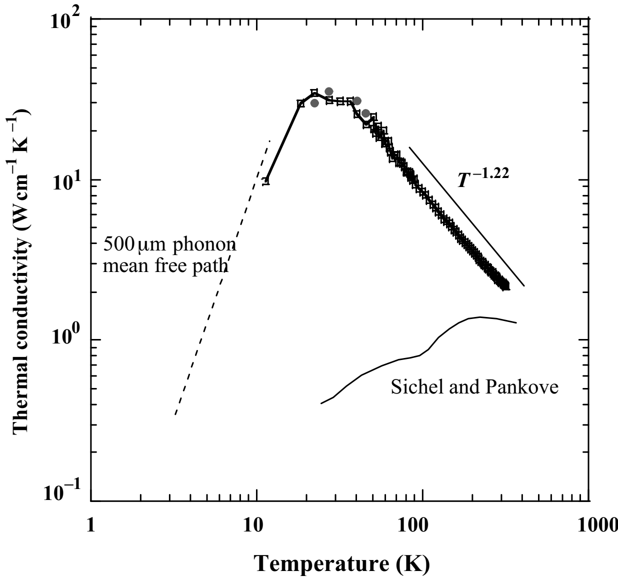

Figure 1.22 The thermal conductivity of 200 μm thick freestanding GaN sample (Samsung) as a function of temperature. The dashed line indicates calculation using the boundary scattering limit for a phonon mean free path of 500 μm. Also shown is the $T^{-1.22}$dependence between about 80 and 300 K, and earlier results of Sichel and Pankove [207] measured using a 400 μm HVPE sample. Courtesy of Slack and Morelli [91].

acoustic–acoustic and acoustic–optic interactions. This temperature dependence strongly suggests that the thermal conductivity depends mainly on intrinsic phonon–phonon scattering and not on phonon–impurity scattering. Keep in mind that the net electron concentration in the measured film is about $10^{16}\,cm^{-3}$ and the hole concentration is in the $10^{15}\,cm^{-3}$ range. In addition, the dislocation density is low, about $10^{6}\,cm^{-2}$. It should be pointed out that the thermal conductivity degrades with increased dislocation density, particularly above $10^{7}\,cm^{-2}$, with a slope of 0.4 W $cm^{-1}\,K^{-1}$ per decade dropping down to slightly above 1 W $cm^{-1}\,K^{-1}$ for a dislocation density of mid-$10^{9}\,cm^{-2}$. The dashed curve at low temperatures in Figure 1.22 has been calculated for boundary scattering assuming a mean free path of 500 μm [91]. The mean free path is comparable with the average sample diameter, which indicates that impurity scattering in this region is not dominant either.

The thermal conductivity of GaN is a tensor quantity and has two principal values $\kappa_{\perp}$ and $\kappa_{||}$ perpendicular and parallel to the *c*-axis, respectively, that is, in-plane and out-of-plane values. The anisotropy in the sound velocity, which relates to the phonon propagation velocity, has been calculated by Polian *et al.* [38] in the form of $v_{\perp} = 5.56 \times 10^{5}\,cm\,s^{-1}$ and $v_{||} = 5.51 \times 10^{5}\,cm\,s^{-1}$ for in-plane and out-of-plane directions, respectively. These values are smaller than the measured values, reported by Deger *et al.* [165], of $v_{\perp} = 8.02 \times 10^{5}\,cm\,s^{-1}$ and $v_{||} = 7.79 \times 10^{5}\,cm\,s^{-1}$ for in-plane

and out-of-plane directions, respectively. The in-plane and out-of-plane sound velocities reported in Ref [36] are tabulated in Tables 1.7 and 1.9 for wurtzitic and zinc blende phases of GaN. Because the difference is negligible and the anharmonicity producing the phonon–phonon scattering is not discernible, one can conclude that in-plane thermal conductivity measurements are a good representative of κ in GaN [91].

A newer method, named the scanning thermal microscopy (SThM) [209], has been developed to measure thermal conductivity and is purported to provide nondestructive, absolute measurements with a high spatial/depth resolution of about 2–3 μm. Thermal imaging is achieved using a resistive thermal element incorporated at the end of a cantilever/AFM-type feedback as shown in Figure 1.23. The resistive tip forms one element of a Wheatstone bridge as shown in Figure 1.24. The spatial/depth resolution is estimated to be ~2–3 μm for GaN and AlN. Upon contact with the sample, the tip tends to cooldown due to heat conduction into the sample, which is related to its thermal conductivity, κ. The bridge circuit applies a compensating voltage (U_{out}) to maintain its target operating temperature. The feedback signal for constant resistance is a measure of the thermal conductivity of the material with which the tip is in contact, specifically V_{out}^2 is proportional to κ because power dissipation is the mechanism here. Measurements of the absolute values of κ are based on a calibration procedure. This simply comprises calibrating the feedback signal, V_{out}^2, for a constant thermal element resistance against that for samples with known conductivities such as GaSb, GaAs, InP, Si, and Al metal, as shown in Figure 1.25. The influence of the surface roughness on the effective thermal conductivity is of concern. For a perfectly flat surface,

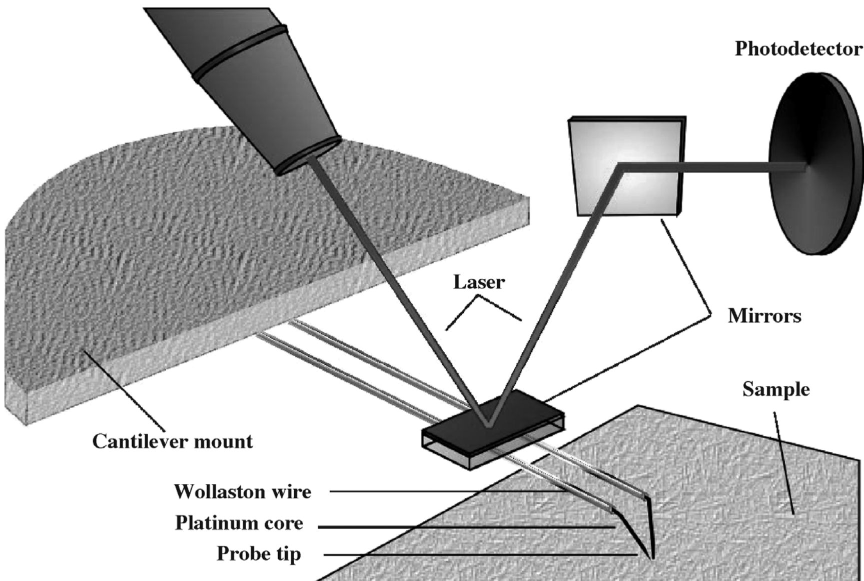

Figure 1.23 An artist's view of the scanning thermal microscope. Patterned after D.I. Florescu and F.H. Pollak. (Please find a color version of this figure on the color tables.)

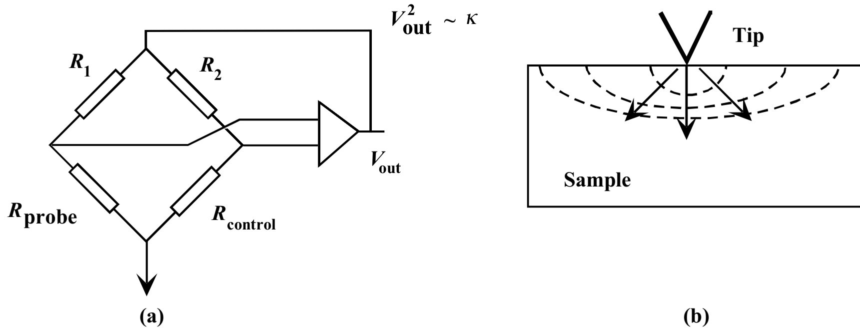

Figure 1.24 (a) Wheatstone bridge arrangement in which the tip temperature is kept constant before and after contact with the material whose thermal conductivity is being measured. The feedback signal U_{out} is related to thermal conductivity, κ. A calibration against known samples such as Si, GaAs, GaP, and so on, leads to absolute values of κ. (b) Schematic diagram of heat dissipation into the sample from the tip. Courtesy of D.I. Florescu and F.H. Pollak.

the contact between the probe tip (radius of curvature ~1 fm) and the sample surface is very small. For rough surfaces, however, the tip could impinge on a valley- or hillocklike feature with the valley/hillock leading to increased/decreased thermal signal accompanied by a corresponding change in the measured effective thermal conductivity.

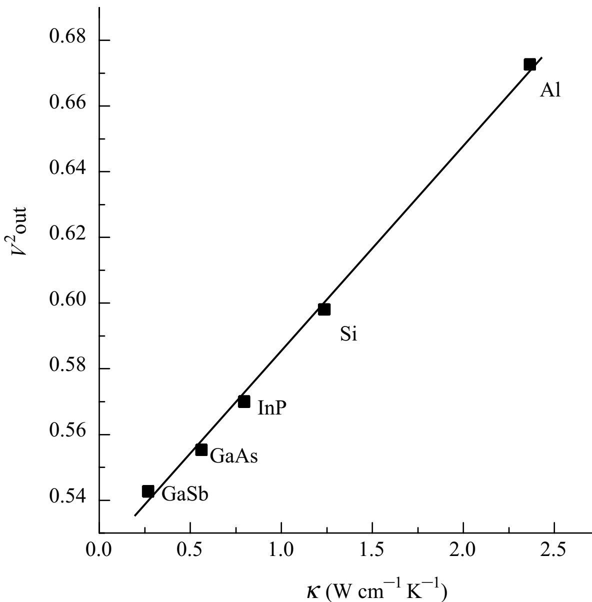

Figure 1.25 The feedback signal, V^2_{out}, which is a measure of the thermal conductivity of the material under test, for a constant thermal element resistance for samples with known conductivities such as GaSb, GaAs, InP, Si, and Al metal. Courtesy of D.I. Florescu and F.H. Pollak.

The SThM method has been applied to the measurement of the room-temperature thermal conductivity on both fully and partially coalesced epitaxial lateral overgrown GaN/sapphire (0 0 0 1) samples [209]. As expected, a correlation between low threading dislocation density and high thermal conductivity values was established. The reduction in the thermal conductivity with increased dislocation density is expected as threading dislocations degrade the sound velocity and increase the phonon scattering in the material. In fact, due to the high defect concentrations in early films, the thermal conductivity value measured was 1.3 $W cm^{-1} K^{-1}$ [207]. Using this method, the highest GaN κ values, 2.0–2.1 $W cm^{-1} K^{-1}$, were found in the regions of the samples that were laterally grown and thus contained the lowest density of threading dislocations. This compares with a value of 2.3 $W cm^{-1} K^{-1}$ in a freestanding sample measured by the steady-state four-probe method discussed earlier. Even then, it falls short of the predictions by Witek [208].

An explanation for the dramatic increase from to $\kappa \sim 1.3\, W cm^{-1} K^{-1}$ for the early samples to 2.3 $W cm^{-1} K^{-1}$for the freestanding sample, as iterated above is most likely related to extended defect concentration (D_d) and the differences in background doping. The effect of dislocation density on the thermal conductivity has been calculated by Kotchetkov *et al.* [210]. The dislocation density in the thick film measured by Sichel and Pankove was between 10^9 and $10^{10} cm^{-2}$, while the freestanding sample exhibited densities of less than $10^6 cm^{-2}$ near the top surface (Ga-polarity) and $10^7 cm^{-2}$ near the bottom surface (N-polarity). Kotchetkov *et al.* showed that κ remains fairly independent of D_d up to some characteristic value D_d^{char} after which it decreases about a factor of 2 for every decade of increase in D_d.

The thermal conductivity has also been correlated to doping levels in HVPE n-GaN/sapphire (0 0 0 1) by SThM on two sets of samples [211,212]. In both sets of data, the thermal conductivity decreased linearly with $\log n$, n being the electron concentration, the variation being about a factor of 2 decrease in κ for every decade increase in n. Significantly, it was concluded that the decrease in the lattice contribution to κ, due to increased phonon scattering from impurities and free electrons, predominates the increase in the electronic contribution. Also, a correlation between the film thickness and the improved thermal conductivity was found, which is consistent with the observed general reduction of both extended (dislocations) and point defects with film thickness [212].

The κ values at 300 K before and after plasma-induced effects on a series of n-GaN/sapphire (0 0 0 1) samples fabricated by HVPE were also measured [213]. The sample thicknesses were $50 \pm 5\, \mu m$ and the carrier concentrations were $\sim 8 \times 10^{16} cm^{-3}$, as determined by Hall effect measurements. The thermal conductivity before treatment was found to be in the 1.70–1.75 $W cm^{-1} K^{-1}$ range, similar to that previously reported for HVPE material with this carrier concentration and thickness [211,212]. The κ value was reduced, however, when the samples were processed under constant Ar gas flow and pressure for a fixed period of time (5 min). The only variable processing parameter was the DC bias voltage (125–500 V). After the initial 125 V procedure, κ exhibited a linear decrease with the DC voltage in the investigated range. At 125 V, the thermal conductivity was only slightly less ($\kappa \sim 1.65\, W cm^{-1} K^{-1}$)

than the untreated case. The values of κ had dropped to $\sim 0.3\,\mathrm{W\,cm^{-1}\,K^{-1}}$ for the 500 V case.

To a first extent, the temperature dependence of the specific heat of Wz GaN (C_p) at constant pressure can be expressed by phenomenological expression [51]. In this vein, the specific heat C_p of Wz GaN at constant pressure for 298 K < T < 1773 K can be expressed as

$$\begin{aligned} C_P(T) &= 9.1 + (2.14 \times 10^{-3}T)(\mathrm{J\,mol^{-1}\,K^{-1}}), \\ C_p &= 38.1 + 8.96 \times 10^{-3}T\ (\mathrm{cal\,mol^{-1}\,K^{-1}}) \quad (1\,\mathrm{cal} = 4.186\,\mathrm{J}). \end{aligned} \tag{1.15}$$

However, this expression is very simplistic, as will be seen below. As already mentioned, free electrons (very effective at low temperatures), impurities, defects (inclusive of point defects), and lattice vibrations contribute to specific heat. If GaN with negligible free-electron concentration and defects were available, only the lattice contribution would be considered, which is also the case in texts [214]. The specific heat of Wz GaN has been studied by Koshchenko *et al.* [215] in the temperature range of 5–60 K and also by Demidienko *et al.* [216] in the temperature range of 55–300 K and discussed by Krukowski *et al.* [88,127]. The Debye expression for the temperature dependence of specific heat in a solid at a constant pressure (C_p) can be expressed as [214]

$$C_p = 18R\left(\frac{T}{\theta_D}\right)^3 \cdot \int_0^{x_D} \frac{x^4 e^x}{(e^x - 1)^2}\,dx, \tag{1.16}$$

where $x_D \equiv \theta_D/T$ and $R = 8.3144\,\mathrm{J\,mol^{-1}\,K^{-1}}$ is the molar gas constant. The coefficient in front of the term R has been multiplied by 2 to take into account the two constituents making up the binary GaN. By fitting the measured temperature-dependent heat capacity to the Debye expression, one can obtain the *Debye temperature* θ_D specific to heat capacity. The experimental data of Demidienko *et al.* and Krukowski *et al.* are plotted in Figure 1.26. Also shown in the figure is the calculated specific heat using the Debye expression for Debye temperatures of 500, 600, 700, and 800 K. It is clear that the quality of the data and/or sample prevents attainment of a good fit between the experimental data and Equation 1.16. Consequently, a Debye temperature with sufficient accuracy cannot be determined. It is easier to extract a Debye temperature using data either near very low temperatures or well below the Debye temperature where the specific heat has a simple cubic dependence of temperature [214]:

$$C_p = 234R\left(\frac{T}{q_D}\right)^3. \tag{1.17}$$

Unfortunately, the GaN samples contain large densities of free carriers and defects that compromise the application of the Debye specific heat expression. Consequently, a good fit to the data is not obtained and the Debye temperature so extracted is not as dependable as desired.

There is a spread in the reported Debye temperatures for GaN, θ_D, in the range of about 600 to 700 K. Slack [77] estimated a value of 600 K at 0 K by utilizing the more established Debye temperatures for BeO and AlN. This compares with 550 K deduced

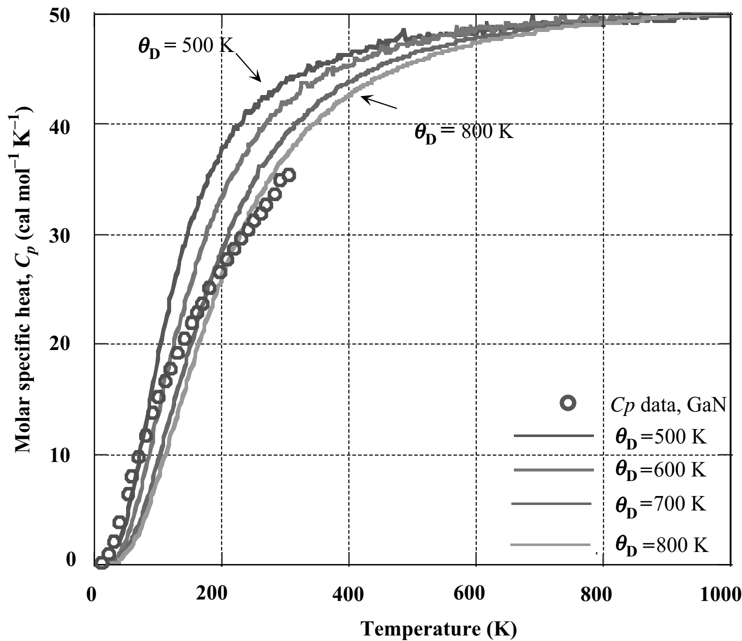

Figure 1.26 Molar specific heat at constant pressure, C_p (cal mol^{-1} K^{-1}), of GaN versus temperature. Open circles represent the experimental data. The solid lines are calculation based on the Debye model for Debye temperatures, θ_D, of 500, 600, 700, and 800 K. Unfortunately, it is difficult to discern a Debye temperature that is effective over a wide temperature range because a large concentration of defects and impurities is present in GaN. However, a value of 600 K estimated by Slack is used commonly. The data are taken from Refs [215,216], as compiled in Ref. [88]. (Please find a color version of this figure on the color tables.)

from heat transfer due to acoustic phonons, as mentioned above. Because the samples used in these measurements contained defects and large density of free electrons, the dispersion among the data and Debye expression is attributed to defects at high temperatures and free electrons at low temperatures. Elastic properties of GaN can also be used to deduce the Debye temperature. In this vein, Raman scattering measurements yielded a Debye temperature of $\theta_D = 650$ K [38]. Calculations since the estimate of Slack [77] yielded a range of 620–690 K [88].

Thermodynamic properties of Wz GaN have been reported by Elwell and Elwell [217]. From the reaction

$$\mathrm{Ga(s)} + 1/2\mathrm{N_2(g)} = \mathrm{GaN(s)}, \tag{1.18}$$

the *heat of formation* of Wz GaN was calculated to be $\Delta H_{298\,\mathrm{K}} = -26.4$ kcal mol^{-1} [217], or as the standard heat of formation $\Delta H = -37.7$ kcal mol^{-1} [194]. The equilibrium vapor pressure of N_2 over solid GaN has been found to be 10 MPa at 1368 K and 1 GPa at 1803 K [202]. A thorough description of the GaN phase diagram including the equilibrium vapor pressure of N_2 over GaN as well as AlN and InN has been presented by Porowski and Grzegory [218] (1 cal = 4.186 J).

1.3 Aluminum Nitride

AlN exhibits many useful mechanical and electronic properties. For example, hardness, high thermal conductivity, resistance to high temperature and caustic chemicals combined with, in noncrystalline form, a reasonable thermal match to Si and GaAs in somewhat relaxed terms, make AlN an attractive material for electronic packaging applications. The wide bandgap is also the reason for AlN to be touted as an insulating material in semiconductor device applications. Piezoelectric properties make AlN suitable for surface acoustic wave device applications [219]. However, the majority of interest in this semiconductor in the context of electronic and optoelectronic device arena stems from its ability to form alloys with GaN producing AlGaN and allowing the fabrication of AlGaN/GaN and AlGaN/InGaN-based electronic and optical devices, the latter of which is active from the green wavelengths well to the ultraviolet. AlN also forms a crucial component of the nitride-based AlInGaN quaternary, which makes tuning of the bandgap independent of composition to some extent. This way, lattice-matched conditions to the underlying epitaxial structure can be maintained while being able to adjust the bandgap.

AlN is not a particularly easy material to investigate because of the high reactivity of aluminum with oxygen in the growth vessel. Early measurements indicated that oxygen contaminated material can lead to errors in the energy bandgap and, depending on the extent of contamination, in the lattice constant. Only recently achieved contamination-free deposition environments coupled with advanced procedures have allowed researchers to consistently grow improved-quality AlN. Consequently, many of the physical properties of AlN have been reliably measured and bulk AlN synthesized.

1.3.1 Mechanical Properties of AlN

When crystallized in the hexagonal wurtzite structure, the AlN crystal has a molar mass of 40.9882 g mol^{-1}, restated for convenience. The cubic form is hard to obtain and thus will be ignored. The point group symmetry for the wurtzite structure in the Schoenflies notation is C_{6v}^4 ($P6_3mc$ in the Hermann–Mauguin notation), restated for convenience. Reported lattice parameters range from 3.110 to 3.113 Å for the a parameter (3.1106 Å for bulk, 3.1130 Å for powder, and 3.110 Å for AlN on SiC), and from 4.978 to 4.982 Å for the c parameter. The c/a ratio thus varies between 1.600 and 1.602. The deviation from that of the ideal wurtzite crystal ($c/a = 1.633$) is probably because of the lattice stability and ionicity. The u parameter for AlN is 0.3821, which is larger than the calculated value of 0.380 using Equation 1.1. This means that the interatomic distance and angles differ by 0.01 Å and 3°, respectively, from the ideal [16].

Whereas the metastable zinc blende polytype AlN has a value of $a = 4.38$ Å [220], the rock salt structure has a value of $a = 4.043$–4.045 Å at room temperature [5,221]. Table 1.13 summarizes some of the observed structural properties of AlN.

Early investigations of the elastic properties of AlN were carried out on sintered polycrystalline specimens, owing to the unavailability of large single crystals. This, however, paved the way to more refined measurements as single crystalline AlN became available. The measured *bulk modulus B*, which is related to elastic stiffness coefficients through Equation 1.11, and *Young's modulus* Y_0 or E are compiled in Table 1.29 along with the entire set of elastic stiffness coefficients. The latter were obtained by fitting the results of surface acoustic wave measurements made on epitaxial AlN films and by Brillouin scattering measurements made on an AlN single crystal [160]. Wagner and Bechstedt [178] suggested that reliable values for the elastic constants should produce $2C_{13}/C_{33} = 0.5–0.6$ and $\nu = 0.18–0.21$. The *ab initio* calculations [42,178] and some measurements [83,165] provide similar results. However, the values from some of the calculations [165,222] and measurements [169,223] should be used with caution because of the large deviations in one or more coefficients. Surface acoustic wave measurements of Deger *et al.* [165] are very reliable because they include the correction for piezoelectric stiffening. Bulk modulus values range from 159.9 GPa, measured by an ultrasonic method, to 237 GPa, measured by Brillouin scattering. The range for the same from calculations is 111–239 GPa [160]. Young's modulus is measured as 374 GPa for single-crystal AlN [82] and 295 GPa for AlN thin films [224].

The hardness of AlN has been measured to be ≈12 GPa on the basal plane (0 0 0 1) using a Knoop diamond indenter [225]. Some anisotropy in *Knoop's hardness* has been observed for the indent direction perpendicular to the *c*-axis with measured values in

Table 1.29 Experimental bulk modulus and elastic coefficients (in GPa) of AlN (from Ref. [160] and references therein).

Method	C_{11}	C_{12}	C_{13}	C_{33}	C_{44}	B	B'	E or Y_0
Ultrasonics [223]	345	125	120	395	118	201		334
Ultrasonic						159.9	5.2	308
Ultrasonic [165]	410	140	100	390	120	209		354
ADX						207.9	6.3	
Brillouin [83]	410.5	148.5	98.9	388.5	124.6	210.1		354
Brillouin [169]	419	177	140	392	110	237		326
EDX						185	5.7	
Hardness [82]						220		374
PWPP [42]	396	137	108	373	116	207		329
FP-LMTO [165]	398	140	127	382	96	218		322
HF [222]	464	149	116	409	128	231		365
PWPP [178]	C_{11} FIX THIS	538	113	370		210		322
Zinc blende HF [222]	348	168			135	228		$Y_0 = (C_{11} + 2C_{12}) \times (C_{11} - C_{12})/(C_{11} + C_{12})$

ADX: angular dispersive X-ray diffraction; EDX: energy dispersive X-ray; PWPP: plane wave pseudopotential; FP-LMTO: full-potential linear muffin–tin orbital; HF: Hartree–Fock.

the range of 10–14 GPa [81]. More recent nanoindentation measurements on single-crystal AlN revealed a hardness of 18 GPa [82].

The phonon structure of AlN has been the subject of numerous investigations. As in the case of GaN, the phonon dispersion spectrum of Wz AlN has 12 branches, 3 acoustic, and 9 optical ones [226]. LO and TO phonon energies have been obtained from fits to infrared reflectivity measurements, the results of which are tabulated in Table 1.30. Raman-active optical phonon modes belong to the A_1, E_1, and E_2 group representations. Several Raman scattering studies on AlN have been conducted, and the measured phonon energies are listed in Table 1.30 along with the calculated values by Wagner and Bechstedt [178]. The shift of phonon energies with strain was studied experimentally by Gleize *et al.* [227] and theoretically by Wagner and Bechstedt [178]. Gleize *et al.* [227] investigated strained 500 nm thick AlN layers grown on 6H-SiC. Using the strain values deduced from high-resolution X-ray diffraction and phonon frequency shifts measured by micro-Raman spectroscopy, the deformation potentials were obtained for most of the zone center optical phonons of Wz AlN. The determination of the deformation potentials is based on the knowledge of the ideal equilibrium state of the material from which strains and phonon shifts are defined. Additionally, hydrostatic pressure coefficients and elastic constants of the bulk material are also needed for extracting the deformation potentials from the raw experimental data. The deviations in the published data originate from the fact that different sets of parameters are typically used for this purpose. Table 1.30 lists the phonon deformation potentials from Gleize *et al.* [227] along with the results from pseudopotential plane wave calculations of Wagner and Bechstedt [178], which produced slightly lower values.

The frequencies or energies of vibrational modes are very sensitive to the strain state of the samples. Strain inhomogeneities and imperfections cause the linewidths in Raman observable mode to be broad reducing the accuracy of central frequency determination. Tischler and Freitas Jr [228] utilized freestanding and high-quality AlN oriented along the (0 0 0 1) plane, as characterized by X-ray with full width half maximum (FWHM) of 36–54 arcsec. Listed in Table 1.30 are also the data of Tischler and Freitas Jr, which by virtue of the high quality of sample should be used as standard. Tischler and Freitas Jr [228] also estimated the linewidths of the Raman modes by fitting the data with Lorentzian peaks from which the phonon decay times were deduced by relying on the uncertainty principle in the form of $\Delta E/\hbar = \Gamma/\hbar = 1/\tau$, where ΔE, Γ, and τ represent the error bar for the energy and linewidths, and the phonon decay time, respectively. The phonon decay times so deduced are in the range of 0.7 ps for E_1(LO) to 5.3 ps for E_2^1.

To get a flavor of the range of experiments regarding the mechanical properties, including vibrational phonon properties, of *epitaxial* AlN, a mention of the investigations on AlN deposited on silicon and sapphire substrates at ~325 K by IBAD undertaken by Ribeiro *et al.* [230] is made. Raman scattering measurements revealed interesting vibrational features related to the atomic composition and structure of the films. Features related to crystalline (c-) Si and corresponding to 2TA(L) at ~230 cm^{-1}, 2TA(X) at ~304 cm^{-1}, 2TA(Σ) at ~435 cm^{-1}, TO(Γ) at 520 cm^{-1}, TA(Σ) + TO (Σ) at ~615 cm^{-1}, accidental critical points at ~670 and ~825 cm^{-1}, 2TO(Δ) at

Table 1.30 Optical phonon energies and phonon deformation potentials for AlN.

Mode	Wz (Raman) unstrained [228]		Wz (Raman range) (cm^{-1})		Wz unstrained (calculated)	Deformation potentials			
						Raman [227]		Calculated [178]	
	(meV)	(cm^{-1})	Ref. [157]	Ref. [229]	(cm^{-1}) [178]	a_λ	b_λ	a_λ	b_λ
E_1-TO	82.8	667.2	667–673	668	677	-982 ± 83	-901 ± 145	−835	−744
A_1-TO	75.4	608.5	614–667	608	618	-930 ± 94	-904 ± 163	−776	−394
A_1-LO	75.4	888.9		890					
E_1-LO	112.8	909.6	895–921		924			−867	−808
E_2^1 (E_2 low)	30.5	246.1		246					
E_2^2 (E_2 high)	81.2	655.1		655					

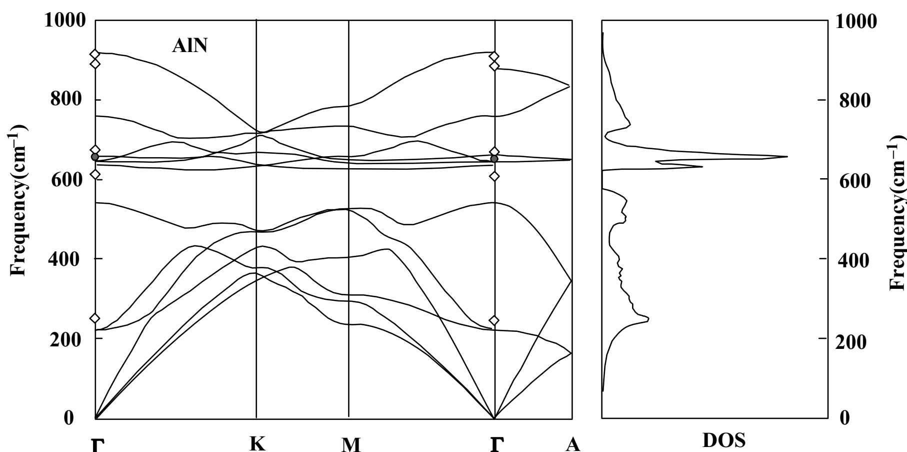

Figure 1.27 Phonon dispersion curves and phonon density of states for Wz AlN reported in Ref. [234]. The data points have their roots in Ref. [83] and are discussed and compared with the *ab initio* calculations in Ref. [233].

$\sim$950 cm^{-1}, 2TO(L) at $\sim$980 cm^{-1}, 2TO(Γ) at $\sim$1085 cm^{-1}, 2TA(X) + 2TO (Γ) at $\sim$1300 cm^{-1}, and 3TO(Γ) at $\sim$1450 cm^{-1} have been observed. A very narrow peak seen at $\sim$2330 cm^{-1} has been attributed to molecular nitrogen on the surface of c-Si [231]. It is worth noting that because of the extremely weak Raman signal usually presented by low quality AlN films, some of the previously reported features have been erroneously identified [232]. Misidentification of some vibration modes could lead to incorrect interpretations of the crystalline quality of AlN films.

As in the case of GaN, the acoustic modes are simple translational modes, whereas the optical modes for wurtzite symmetry are more complex as shown in Figure 1.12. The calculated phonon dispersion curves [233,234] along with the phonon density of states for wurtzitic AlN are shown in Figure 1.27.

1.3.2
Thermal and Chemical Properties of AlN

Single crystalline forms of this compound either in the epitaxial form or bulk form represent the focus of this treatment. In its most commonly available form, AlN is an extremely hard ceramic material with a melting point higher than 2000 °C. In single crystalline form, the melting of AlN was measured to be 2750–2850 °C at nitrogen pressures of 100 and 200 atm (or bar) [235]. The melting temperatures for various nitrides were also determined by Van Vechten [236], who made use of a semiempirical theory for electronegativity and concluded that the melting point of AlN is close to 3487 K. Slack and McNelly [195] calculated the N_2 equilibrium pressures over liquid Al to be 1, 10, and 100 bar at 2563, 2815, and 3117 °C, respectively, as shown in Figure 1.18 in the context of the GaN discussion.

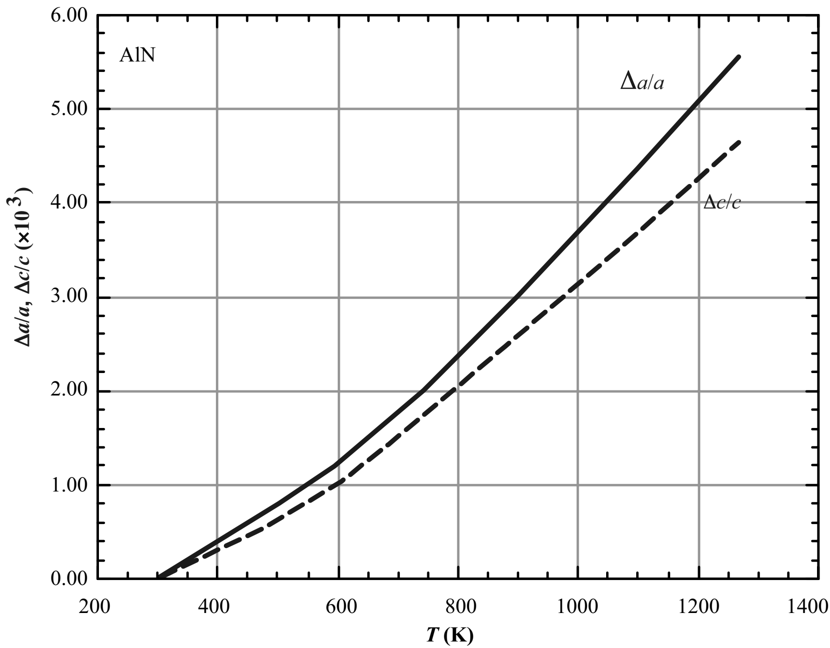

Figure 1.28 Variation of the thermal expansion coefficient of AlN with temperature in the c-plane and in the c-direction [86,87,225].

Using X-ray techniques across a broad temperature range (77–1269 K), it was noted by Slack and Bartram [85] that the thermal expansion of AlN is isotropic with a room-temperature value of $2.56\times10^{-6}\,\mathrm{K}^{-1}$. The thermal expansion coefficients of AlN measured by Yim and Paff [237] have mean values of $\Delta a/a = 4.2\times10^{-6}\,\mathrm{K}^{-1}$ and $\Delta c/c = 5.3\,10^{-6}\,\mathrm{K}^{-1}$. The dependence of the thermal expansion coefficient on temperature in the c-plane and in the c-direction is shown in Figure 1.28, which can be fitted by the following polynomials (for $293 < T < 1700$ K):

$$\begin{aligned}\Delta a/a_0 = & -8.679\times10^{-2} + 1.929\times10^{-4}T + 3.400 \\ & \times10^{-7}T^2 - 7.969\times10^{-11}T^3\end{aligned} \tag{1.19}$$

and

$$\begin{aligned}\Delta c/c_0 = & -7.006\times10^{-2} + 1.583\times10^{-4}T + 2.719 \\ & \times10^{-7}T^2 - 5.834\times10^{-11}T^3,\end{aligned} \tag{1.20}$$

where a_0 and c_0 represent the 300 K lattice parameters. For AlN powder, Krukowski *et al.* [88] reported the expansion coefficient for the a parameter to be $2.9\times10^{-6}\,\mathrm{K}^{-1}$, and the same for the c parameter to be $3.4\times10^{-6}\,\mathrm{K}^{-1}$.

The specific heat of AlN has been discussed extensively. Mah *et al.* [238] approximated the specific heat C_p of AlN in the temperature interval 298–1800 K as

$$\begin{aligned}C_p = & \,45.94 + 3.347\times10^{-3}T - 14.98 \\ & \times10^{-5}T^{-2}\,\mathrm{J\,mol^{-1}\,K^{-1}} \quad (1\,\mathrm{cal} = 4.186\,\mathrm{J}).\end{aligned} \tag{1.21}$$

The same for the higher temperature range of 1800–2700 K was approximated by Glushko *et al.* [239] as

$$C_p = 37.34 + 7.86 \times 10^{-3} T \text{ J mol}^{-1}\text{ K}^{-1} \quad (1\text{ cal} = 4.186\text{ J}) \tag{1.22}$$

relying on the following points: the specific heat $C_p = 51.5\text{ J mol}^{-1}\text{ K}^{-1}$ at $T = 1800$ K, and an estimated value, $C_p = 58.6\text{ J mol}^{-1}\text{ K}^{-1}$ at $T = 2700$ K, as outlined by Krukowski *et al.* [88].

Specific heat obtained from the above approximations coupled with the measured values for a constant pressure from the literature has been tabulated [88], a plot of which is shown in Figure 1.29 along with the calculated specific heat using Equation 1.16 for Debye temperature values of 800–1100 K with 50 K increments. The best fit between the data and the Debye specific heat expression for insulators

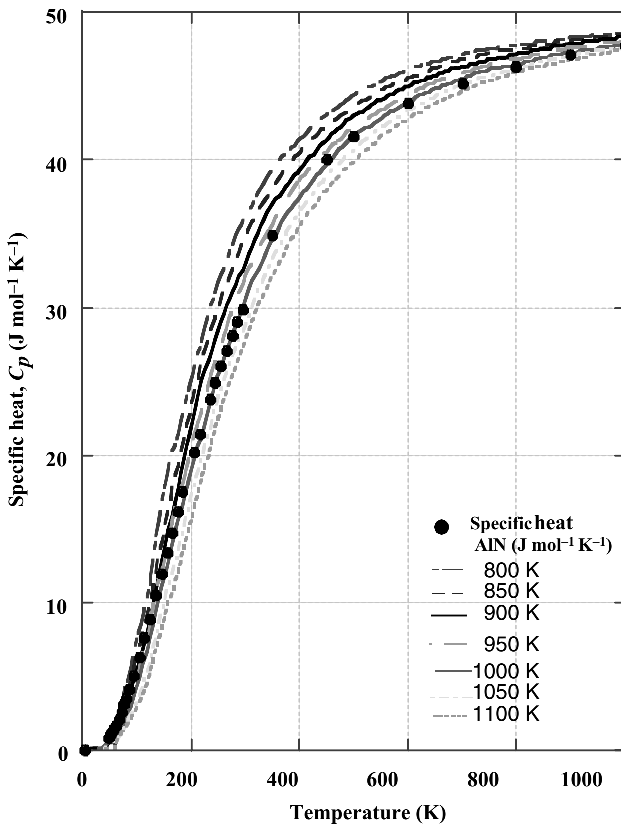

Figure 1.29 Molar specific heat at constant pressure, C_p (J mol^{-1} K^{-1}, 1 cal = 4.186 J), of AlN versus temperature. Open circles represent the experimental data. The solid lines are calculation based on the Debye model for Debye temperatures, θ_D, in the range of 800–1100 K with 50 K increments. The data can be fit with Debye expression for $\theta_D = 1000$ K, which compares with 950 K reported by Slack *et al.* The data are taken from Ref. [88]. (Please find a color version of this figure on the color tables.)

indicates a Debye temperature of 1000 K, which is in good agreement with 950 K reported by Slack *et al.* [240]. Compared to the GaN figure, the Debye temperature so obtained for AlN appears more dependable owing to a much better fit.

The equilibrium N_2 vapor pressure above AlN is relatively low compared to that above GaN that makes AlN easier to be synthesized. The calculated temperatures at which the equilibrium N_2 pressure reaches 1, 10, and 100 atm are 2836, 3088, and 3390 K, respectively [195]. Details of the thermodynamic properties of AlN can be found in Refs [87,88].

Similar to GaN, albeit to a lesser extent, AlN exhibits inertness to many chemical etches. A number of AlN etches have been reported in the literature. However, molten salts such as KOH or NaOH at elevated temperatures such as 50–100 °C, lower than what is required for GaN by as much as 200 °C, etch AlN at appreciable rates. The surface chemistry of AlN has been investigated by numerous techniques including Auger electron spectroscopy, XPS, ultraviolet photoemission spectroscopy (UPS), ultraviolet photoelectron spectroscopy, and electron spectroscopy. One of these investigations by Slack and McNelly [195] indicated that the AlN surface grows an oxide 50–100 Å thick when exposed to ambient air for about a day. However, this oxide layer was protective and resisted further decomposition of the AlN samples. Details can be found in Refs [87,157].

The *thermal conductivity* κ of AlN at room temperature has been predicted as $\kappa = 3.19\,\mathrm{W\,cm^{-1}\,K^{-1}}$ [77,241]. Values of κ measured at 300 K are 2.5 [241] and $2.85\,\mathrm{W\,cm^{-1}\,K^{-1}}$ [85]. The predicted values are near $3.2\,\mathrm{W\,cm^{-1}\,K^{-1}}$ in an O-free simulated material but are based on measurements in AlN containing O [77]. A more recent prediction for the value in AlN is $5.4\,\mathrm{W\,cm^{-1}\,K^{-1}}$, which is much larger than any measured value [208]. The measured thermal conductivity as a function of temperature in bulk AlN containing some amount of O is plotted in Figure 1.30a and b. Also shown is a series of samples with estimated concentrations of O showing an overall reduction in the thermal conductivity with O contamination. The calculation results of Slack *et al.* for impurity- and defect-free AlN are shown as well. In the temperature range of interest where many of the devices would operate, the thermal conductivity in the sample containing the least amount of O assumes a $T^{-1.25}$ dependence.

In freestanding and 300–800 μm thick AlN samples grown by HVPE, originally on Si(1 1 1) substrates, values in the range of $3.0\text{–}3.3\,\mathrm{W\,cm^{-1}\,K^{-1}}$ were measured by the SThM method [242]. The dislocation density in these freestanding AlN templates was about $10^8\,\mathrm{cm^{-2}}$ [243].

1.3.3 Electrical Properties of AlN

Owing to the low intrinsic carrier concentration and the deep native defect and impurity energy levels, the electrical characterization of AlN has usually been limited to resistivity measurements. One such measurement by Kawabe and coworkers [244] on transparent AlN single crystals yielded resistivities $\rho = 10^{11}\text{–}10^{13}\,\Omega\,\mathrm{cm}$, a value consistent with other reports [245–247]. However, it was found that impure crystals,

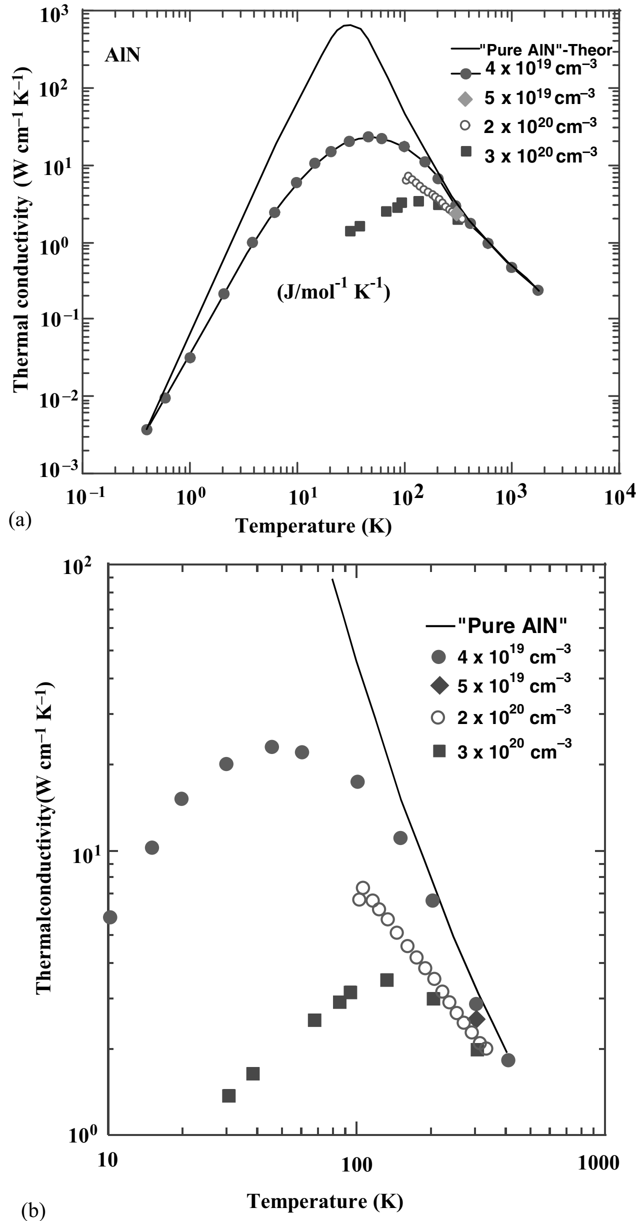

Figure 1.30 (a) Thermal conductivity of single-crystal AlN. The solid line alone indicates the theory whereas the others represent measurements of AlN with various concentrations of O. The lower the O concentration, the higher the thermal conductivity. The theoretical data are from Ref. [77], the data for the lowest O concentration are from Ref. [241], and the data for the other samples are from Ref. [91]. (b) The thermal conductivity of AlN in a limited temperature range of common interest that underscores the detrimental effect of O on the thermal conductivity [240].

which exhibited a bluish color possibly because of the presence of Al_2OC, have resistivities of $\rho = 10^3–10^5\ \Omega\,cm$, much lower than those reported by Chu *et al.* [248], who were purportedly able to obtain both n- and p-type AlN by introducing Hg and Se, respectively. However, they failed to determine the net carrier concentrations owing to very high resistivities. The n-AlN films grown by Rutz [249] had a quite low resistivity ($\rho = 10^3\ \Omega\,cm$), which is comparable to those of Kawabe *et al.* [81]. Although Rutz [249] did not determine the source of the electrons, Rutz *et al.* [250] observed an interesting transition in their AlN films in which the resistivity abruptly decreased by two orders of magnitude with an increase in the applied bias. This observation found applications to switchable resistive memory elements that are operated at 20 MHz.

The insulating nature of these early films hindered meaningful studies of their electrical transport properties. With the availability of refined growth techniques, AlN, presently grown with much improved crystal quality, shows both n- and p-type conductions. This has rejuvenated efforts to measure both electron and hole Hall mobilities. Edwards *et al.* [251] and Kawabe *et al.* [252] carried out some Hall measurements in p-type AlN producing a very rough estimate of the hole mobility $\mu_p = 14\ cm^2\,V^{-1}\,s^{-1}$ at 290 K. The predictions for the Hall mobility in the entire range of AlGaN alloy including the binary end points are treated in Volume 2, Chapter 3. Not all the parameters needed for the calculations are known precisely, reducing the confidence in predicted values somewhat. As in the case for GaN, the room-temperature mobility is dominated by the polar optical phonon scattering.

1.3.4 Brief Optical Properties of AlN

Investigations of the optical absorption coefficient, α, of AlN at room temperature were reviewed as early as 1976 by Slack and McNelly [195]. Harris and Youngman [253] have reviewed photoluminescence and cathodoluminescence characteristics of AlN. Because the AlN lattice has a very large affinity to oxygen, it is almost impossible to eliminate oxygen contamination in AlN that affects observations. Commercially available AlN powder is said to contain about 1–1.5 at.% oxygen. Some oxygen is dissolved in the AlN lattice, with the remainder forming an oxide coating on the surface of each powder grain.

After irradiation with ultraviolet light, AlN doped with oxygen was found to emit a series of broad luminescence bands at near-ultraviolet frequencies at room temperature no matter whether the sample was powdered, single crystal, or sintered ceramic. Pacesova and Jastrabik [254] observed two broad luminescence lines centered in the vicinity of 3.0 and 4.2 eV and more than 0.5 eV wide for samples contaminated at about 1 to 1.5 at.% oxygen. Youngman and Harris [255] and Harris *et al.* [256] investigated the luminescence characteristics of polycrystalline-sintered AlN samples and noted a continuous shift of the peak position in the ultraviolet luminescence line as a function of oxygen content up to a critical concentration of about 0.75 at.%. The luminescence lines beyond this limit of oxygen concentration remained stationary.

Epitaxial layers of about 1 μm or less in thickness on sapphire substrates led to observation of donor bound excitons with phonon replicas and some deep emission [257]. Cathodoluminescence spectra obtained in reactive MBE (RMBE), using ammonia as the nitrogen source, show a sharp band edge peak, which is tentatively assigned to the optical recombination of a donor bound exciton (D^0, X), sometimes accompanied by weak one and two longitudinal optical phonon replicas. Also observed is a broad band with maximum in the range 320–370 nm, although some variation of this low-energy peak has been reported. The 6 K CL spectrum of the near band edge region shows a sharp and strong peak at 2068 Å in addition to two weak peaks on its low-energy side, which are not observed for all samples. The symmetric [0 0 0 2] X-ray diffraction peak is narrow and the linewidth of the prominent near band edge CL peak is 23 meV.

Bulk single crystalline AlN has also been investigated for its CL emission properties. In addition to the near band edge emission at about 6 eV, the ultraviolet oxygen luminescence peak at 4.0 eV was also observed. In the investigation of Youngman and Harris [255], 4.64 eV photons were used to specifically explore the below the band transitions such as the peak near 4 eV. That investigation showed a blue shift with increased O concentration in the peak under question. With the availability of high-quality AlN substrates, presumably high-quality epitaxial AlN layers have been grown on them and characterized for their optical properties by CL at 5 K [107]. In this particular work, the CL measurements were carried out at different temperatures for a fixed electron beam energy density value. The beam current was held at 5 μA and the voltage at 10 kV. The energy density was about 700 W cm^{-2}. Some six emission lines between the energies of 5.98 and 6.03 eV have been delineated in the low-temperature near-band edge emission spectra of those AlN films. In addition to unidentified neutral donor and possibly acceptor bound exciton lines, free exciton A and its excited state, and free exciton B were observed. The availability of A exciton ground and excited states led to a binding energy of 63 meV that gives a low-temperature bandgap of 6.086 eV for this material. The provisionally accepted value for the bandgap of this material is 6.2 eV (which is questionable now that the lower value is supported by measurements performed in homoepitaxial layers).

In terms of absorption, Yim *et al.* [246] characterized AlN by optical absorption determining the room-temperature bandgap to be direct with a value of 6.2 eV. It should be pointed out that this early figure is not consistent with measurements performed later on using high-quality samples as discussed in the previous paragraph. Perry and Rutz [258] performed temperature-dependent optical absorption and determined a bandgap of 6.28 eV at 5 K compared to their room-temperature value of 6.2 ± 0.1 eV. We should point again that it has been lowered to slightly over 6 eV at low temperatures in high-quality samples. Several groups have reported comparable values whereas others have produced questionable values considerably below 6.2 eV, probably due to oxygen contamination or nonstoichiometry. In addition to the band edge absorption, a much lower energy absorption peak at 2.86 eV (although some variation in the peak position has been recorded from 2.8 to 2.9 eV) is likely owing to nitrogen vacancies or nonstoichiometry as proposed by Cox *et al.* [245]. Yim *et al.* [237] also observed a broad emission spectrum range of 2–3 eV with a peak at about 2.8 eV.

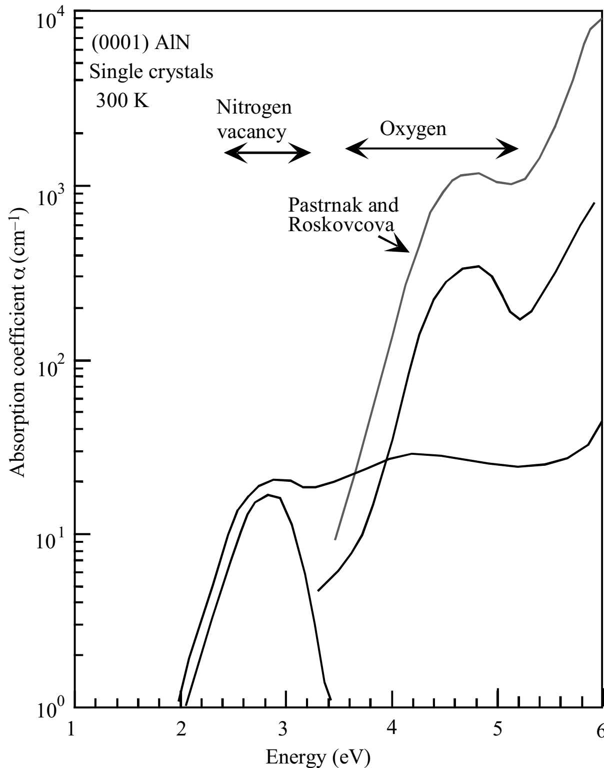

Figure 1.31 Room-temperature absorption spectra of several AlN films of varying thicknesses whose principal absorption edge occurs at 6.2 eV. The bump near 4.5–4.8 eV in the data is attributed to the oxygen absorption bands. The one at about 2.8 eV is attributed to N vacancies [245–247,259–261]. The ones not marked as Pastrnak and Roskovcova [259] are from Slack *et al.* [91].

This peak does not correlate with the presence of oxygen. The oxygen absorption region lies between 3.5 and 5.2 eV, as originally found by Pastrnak and Roskovcova [259–261]. The exact position of this particular peak appears to change with the oxygen content from 4.3 eV at low oxygen content to 4.8 eV at high oxygen content. The results of the studies on the room-temperature absorption coefficient, α, are shown in Figure 1.31 for three different crystals along with the results of Pastrnak and Roskovcova [259]. Low-temperature and room-temperature absorption data taken at 2 K in a thin film on double side polished sapphire are shown in Figure 1.32.

In the only optical study of AlN impurities, Karel and coworkers [262–266] reported on the luminescence of Mg and rare earth centers in AlN.

Measurements of the *refractive index* of AlN have been carried out in amorphous, polycrystalline, and single-crystal epitaxial thin films. The values of the refractive index, n, are in the range of 1.99–2.25 with several groups reporting $n = 2.15 \pm 0.05$.

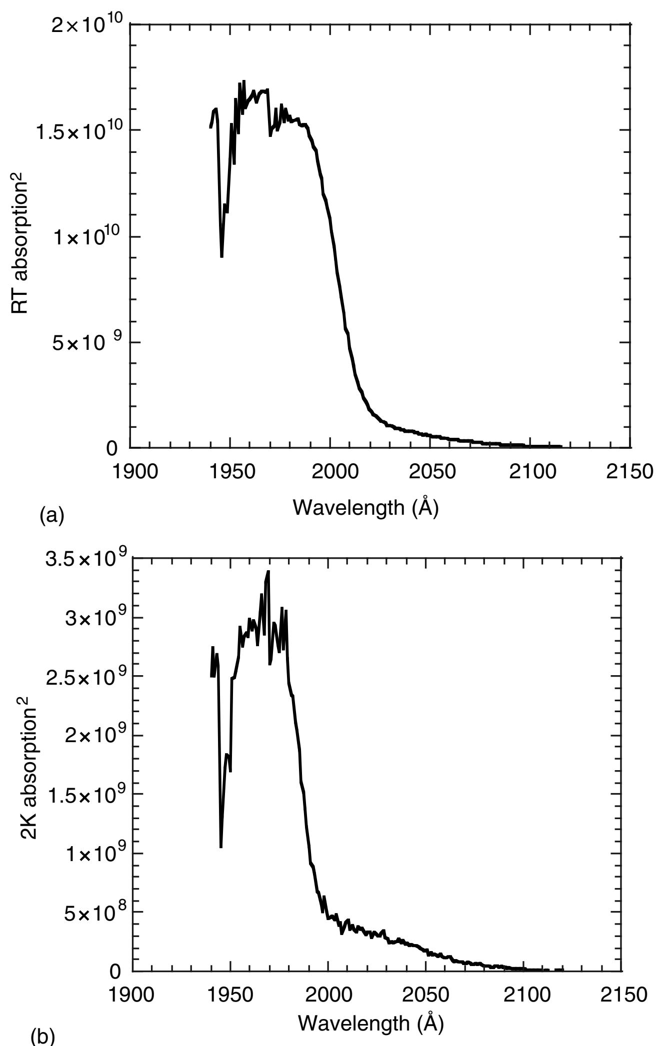

Figure 1.32 Room-temperature (a) and 2 K (b) absorption spectrum of a thin AlN film grown on double side polished *c*-plane sapphire by RF MBE. The data were taken at the University of Pittsburgh by Song Bay and W.J. Choyke using a sample prepared in author's laboratory.

These values are found to increase with increasing structural order, varying between 1.8 and 1.9 for amorphous films, 1.9–2.1 for polycrystalline films, and 2.1–2.2 for single-crystal epitaxial films. The spectral and polarization dependence of the index of refraction has been measured and showed a near-constant refractive index in the wavelength range of 400–600 nm. Some of these measurements also indicate that, in the long-wavelength range, the *dielectric constant* of AlN (ε_0) lies in the range of

8.3–11.5, and that most of the values fall within $\varepsilon_0 = 8.5 \pm 0.2$. Other measurements in the high-frequency range produced dielectric constants of 4.68 and $\varepsilon_\infty = 4.84$. AlN has also been examined for its potential for second harmonic generation.

Synchrotron radiation studies of AlN single crystals up to 40 eV have been performed, which resulted in the observation of an 8 eV luminescence peak. The same peak was also found in vacuum–ultraviolet reflection measurements.

1.4 Indium Nitride

InN forms the third binary anchor of the nitride family and was first synthesized in 1938 [267]. Compared to the other two, GaN and AlN, it is very difficult to form in high quality because of an inherent reason. The disparity in size, electronegativity, and very high vapor pressure of N over In imposes intractable tasks on the crystal grower [197,268]. The very early attempts explored absorption properties of polycrystalline InN films grown by DC discharge [269], reactive cathodic sputtering [270], or RF sputtering [271], and somewhat later RF deposition [272]. Inclusive properties of InN grown by various methods have been discussed in a review [273]. Essentially, the early results suggested a bandgap $E_g = 1.8$–2.0 eV at room temperature. Those techniques gradually gave way to more refined growth methods such as MBE and OMVPE. The stoichiometry, however, has always been a pestering issue and will always remain so, which appears to have been one of the sources of controversy as to InN's true bandgap following the longstanding value of about 1.89 eV. An inordinate number of reports adorned many reputable journals and filled the programs in technical meetings wherein researchers in great numbers argued that the true bandgap of InN is actually 0.7–0.8 eV. In fact, lower values such as 0.65 [274] and 0.67 eV [275] have also been reported. What appeared to be experimentally impeccable results made the theorists to reexamine and redebate their band structure calculations [138,276]. The previously accepted larger value for the bandgap was explained away by O contamination and Moss–Burstein shift [277] because of high electron concentrations inherent to this semiconductor. Excellent reviews chronicling the developments in InN and controversy surrounding its bandgap are available in the literature [278,279].

Owing in part to visceral difficulties touched upon above and its bandgap, regardless of the controversy, InN has received nowhere near the attention given to GaN and AlN. Reiterating, the problems with InN are difficulties in growing high-quality crystalline InN samples, poor luminescence properties of InN, and the existence of alternative well-characterized semiconductors such as AlGaAs and (Ga, Al)AsP, which have energy bandgaps close to that of the old value of InN bandgap (1.89 eV) and InGaAs close to that of the new InN bandgap. Setting the bandgap aside, which is the holy grail of optoelectronic devices, InN possesses the largest room-temperature mobility among all the nitride-based semiconductors. Predictions point to InN being a superior channel layer with its higher mobility for field effect transistors, a topic that will receive more coverage in the pages to follow.

Just when the data and calculations appear to indicate the bandgap of InN to be close to 0.7–0.8 eV [30], there came the reports casting doubt on the accuracy of the small bandgap. The controversy regarding the true bandgap of InN brought this semiconductor, from "obscurity to controversy," in the words of Scott Butcher, who is one of the pioneers involved in InN studies of and instrumental in determining the 1.89 eV bandgap [278]. The controversy is actually not limited to just the bandgap. It spans the whole gambit of its properties including the lattice constant, the effective electron mass, not to mention the hole mass, which is simply left in the dark, the role of hydrogen and oxygen, nonstoichiometry-induced defects, and point and extended defects. Returning to the controversy surrounding the bandgap of InN, proponents of the smaller bandgap argue that the measured larger bandgap from absorption data is most likely skewed by Moss–Burstein shift and/or O contamination. They are also quick to argue that emission near 1.8–1.9 eV has not been observed casting doubt on its accuracy. The opponents of the larger bandgap put forward arguments ranging from Mie resonance owing to scattering or absorption of light in InN-containing clusters of metallic In [280] to In-rich nonstoichiometry-induced defects active near the 0.7–0.8 eV region [281]. In the efforts of the authors of Ref. [280], microcathodoluminescence studies coupled with imaging of metallic In have shown that bright infrared emission at 0.7–0.8 eV arises in the close vicinity of In inclusions and is likely associated with surface states at the metal/InN interfaces. Employing thermally detected optical absorption measurements, Shubina *et al.* [280] suggested that a true bandgap near 1.5 eV, reserving a more accurate figure for the bandgap until after more detailed measurements are carried out. The presence of In inclusions would also make suspect the mobility and doping level data published for this material. In fact, metal inclusions placed by design in GaAs have been shown to skew the electron mobility [282]. Setting this issue aside for now and referring the reader to Chapter 2 for bandgap-related discussion and Chapter 3 for growth-related discussion, let us segue into the discussion of InN properties.

As mentioned, the energy bandgap of InN corresponds to a portion of the electromagnetic spectrum in which alternative and well-developed semiconductor technologies are already available. Consequently, practical applications of InN are more or less restricted to its alloys with GaN and AlN or related heterostructures. The growth of high-quality InN and the enumeration of its fundamental physical properties remain for the present a purely scientific enterprise except of course their impact on the properties of the ternaries it makes with GaN and AlN. InN is not different from GaN and AlN in the sense that it suffers from the same lack of a suitable substrate material and, in particular, a high native defect concentration. All these have hindered its progress. In addition, because of its rather poor thermal stability InN cannot be grown at the high temperatures required by CVD growth processes. As InN rapidly dissociates at high temperatures, even as low as 600 °C, an extraordinarily high nitrogen overpressure would be required to stabilize the material up to the melting point, which is practically impossible. The large disparity of the atomic radii of In and N is another factor that increases the difficulty in obtaining InN of good quality. Notwithstanding the aforementioned characterization, the seminal work of Tansley and Foley [271] first characterized many of the fundamental physical properties of InN.

Tables 1.19–1.22 list the physical properties of InN. It has proved difficult to grow high-quality single crystalline material that would enable detailed optical, structural, and electrical measurements to be performed. Given the fact that the growth of bulk single-crystal InN films using equilibrium techniques is unlikely, attention turned to the deposition of thin films using nonequilibrium techniques. All of the early data summarized below under various properties, unless otherwise specified, were obtained from highly conductive n-type polycrystalline InN grown by nonequilibrium techniques.

There have been several studies that report rapid dissociation of InN at temperatures above 500 °C. Because no high-quality InN has yet been grown, the resistance of the high-quality material to chemical etching is unknown. Successful etching of single crystalline InN films in a hot $H_3PO_4 : H_2SO_4$ solution has been measured as was surface oxidation.

1.4.1 Crystal Structure of InN

To reiterate, indium nitride normally crystallizes in the wurtzite (hexagonal) structure. The zinc blende (cubic) form has been reported to occur in films containing both polytypes. Because of the absence of good-quality single-crystal films, early studies dealing with the crystal structure of InN were limited to mainly less than ideal thin films, particularly the ordered polycrystalline films with crystallites in the thickness range of 50–500 nm. Basically, the measurements confirm that, although InN normally crystallizes in the Wz structure, it occasionally also crystallizes in the zinc blende (cubic) polytype.

Thermal instability of InN forbids growth at high temperatures and a large lattice mismatch with most available substrates inevitably leads to less than perfect structural quality of the epitaxial films grown by any method although the electron mobility in MBE-grown layers have improved considerably. A study based on XRD analysis has provided important insights into the dependence of the structural properties on the degree of lattice mismatch and film thickness of InN [283] on three different kinds of substrates, namely sapphire, GaN, and AlN. Significant improvement in the structural quality of the InN films, which do suffer from the residual strain, was observed on GaN templates. Below a thickness of 1200 Å, the InN film is composed of grain islands with different crystal orientations. Above this thickness, screw dislocations are nucleated, relieving the strain and leading to a reduction of the observed mosaicity in the surface morphology as grains with the same orientation grow with film thickness exceeding 1200 Å.

1.4.2 Mechanical Properties of InN

The measured InN lattice parameters using powder technique are in the range of $a = 3.530–3.548$ Å and $c = 5.704–5.960$ Å with a consistent c/a ratio of about 1.615 ± 0.008. This c/a ratio is close to the more optimistic value of 1.633 determined

from layers especially grown under significant precautions, best possible growth conditions, and presumably with reduced nitrogen vacancies [284]. Another value of the c/a ratio of 1.612 has also been reported using powder diffractometry [29]. There is no reliable experimental u parameter for InN. An examination of the reported data indicates an unacceptably large scatter. This is possibly caused by nitrogen deficiency because nitrogen atoms are closely packed in (0 0 0 1) planes. The single reported measurement yields a lattice constant of $a_0 = 4.98$ Å in zinc blende (cubic) form InN occurring in films containing both polytypes [284]. While the cubic polytype of InN yields a molecular cell volume of 30.9 Å^3, the hexagonal polytype gives a molecular cell volume of 31.2 ± 0.2 Å^3.

The experimental density of InN deduced from Archimedean displacement measurements is 6.89 g cm^{-3} at 250 °C [285]. This is comparable with 6.81 g cm^{-3} estimated from X-ray data. In a hexagonal structure, the second-order *elastic moduli* are C_{11}, C_{12}, C_{13}, C_{33}, and C_{44}. The only report on InN elastic coefficients is by Savastenko and Sheleg [162], but their results are lower than the values calculated by the linear muffin–tin orbital (LMTO) and the plane wave pseudopotential (PWPP) methods and are suggested to be completely unreliable [178]. Table 1.31 summarizes the measured and the calculated elastic coefficients for both Wz and ZB InN. Because these figures depend on the lattice constants that are within some 10%, values of other nitrides can be used as a first approximation when absolutely needed [271,286]. The bulk modulus has been calculated from first principles by the local-density approximation [287] and by the LMTO method [288] suggesting bulk modulus $B = 165$ GPa. The results of other calculations for bulk modulus are shown in Table 1.31. Most of the properties of InN are tabulated in Tables 1.19–1.22.

As in the cases of Wz GaN and Wz AlN, Wz InN has 12 phonon modes at the zone center (symmetry group: C_{6v}), 3 acoustic and 9 optical ones with the acoustic

Table 1.31 Theoretical and experimental elastic coefficients and bulk modulus (in GPa) of the various forms of InN [160].

Method	Structure	C_{11}	C_{12}	C_{13}	C_{33}	C_{44}	B	$dB/dP = B'$
X-ray [162]	Wz	190	104	121	182	10	139	
LMTO [24]	Wz	271	124	94	200	46		
PWPP [42]	Wz	223	115	92	224	48	141	
PWPP [42]	ZB	187	125			86	145.6	
PWPP	ZB						155	4
LMTO	Wz						165	
PWPP	Wz						166	3.8
PWPP	ZB						138	3.9
ADX	Wz						125.5	12.7
LMTO	Wz						165	
PWPP	Wz						139	
PWPP	ZB						140	

ADX: angular dispersive X-ray diffraction; PWPP: plane wave pseudopotential; LMTO: linear muffin–tin orbital.

branches near zero at $k = 0$. The infrared active modes are of the E_1(LO), E_1(TO), A_1(LO), and A_1(TO) type. Raman spectroscopy studies [289,290] have yielded four optical phonons characteristic for InN with wave numbers 190 cm^{-1} (E_2), 400 cm^{-1} (A_1), 490 cm^{-1} (E_1), and 590 cm^{-1} (E_2) in InN layers grown by atomic layer epitaxy (ALE). Moreover, a TO mode has been observed at 478 cm^{-1} (59.3 meV) by reflectance and 460 cm^{-1} (57.1 meV) by transmission measurements [286]. From other reflectance data, the existence of a TO phonon mode at 478 cm^{-1}, consistent with Ref. [286], and an LO mode at 694 cm^{-1} was deduced [291].

1.4.3 Thermal Properties of InN

The linear *thermal expansion coefficients* measured at five different temperatures between 190 and 560 K [292] indicate that both along the parallel and perpendicular directions to the *c*-axis of InN these coefficients increase with increasing temperature. Thermal conductivity derived from the Leibfried–Schloman scaling parameter, assuming that the *thermal conductivity* is limited by intrinsic phonon–phonon scattering, is about $0.80 \pm 0.20\ W\,cm^{-1}\,K^{-1}$.

Using InN microcrystals prepared by microwave nitrogen plasma, the specific heat of InN has been measured with differential scanning calorimeter with a precision better than 1% [88,293]. The data have been fit to the Debye equation, Equation 1.16, as shown in Figure 1.33a. An expanded view of the experimental data over a temperature range of 150–300 K is given in Figure 1.33b. Below 200 K, a Debye temperature of 600 K appears to fit the data well, tabulated in Table 1.32. However, above 200 K a Debye temperature of 700 K fits the data better. This paradox indicates the poor quality of InN and significant contribution by nonvibrational modes, as the Debye theory is developed for a perfect dielectric. Others [88] argue that the Debye temperature of $\theta_D = 660$ K, albeit in a relatively small range, describes InN best.

As shown in Figure 1.18, the melting point of InN, T^M_{InN}, is 2146 K and the line fit to the partial pressure data for N indicates a temperature dependence of 7.9×10^{17} exp $(-2.78\ eV/kT)$ bar for InN. As can be seen in Figure 1.18, the nitrogen partial pressure increases exponentially above $T_E = 630\ ^\circ C$ for InN, illustrating that the decomposition temperature in vacuum is much lower than the melting point achievable under high pressures. To determine the effective decomposition activation energy more precisely, the nitrogen flux was calculated from the measured nitrogen pressure [196,199]. The rate of nitrogen evolution $\Phi(N)$ is equal to the rate of decomposition and the slope of $\ln[\Phi(N)]$ versus $1/T$ in Figure 1.18 gives the effective activation energy of decomposition in vacuum, E_{MN}. The decomposition rate is that corresponding to desorption of one monolayer in 1 s, in other words, $\Phi_N = 1.5 \times 10^{15}$ $cm^{-2}\,s^{-1}$, at 795 °C. The activation energy of the thermally induced decomposition is determined as $E_{MN} = 3.5$ eV (336 kJ mol^{-1}) for InN (M is for metal and N is for nitrogen). This indicates temperature limits for high-temperature or high-power devices. This together with the reported small values of InN bandgap does not bode well for power devices based on InN alone. Of course, the picture is different if this

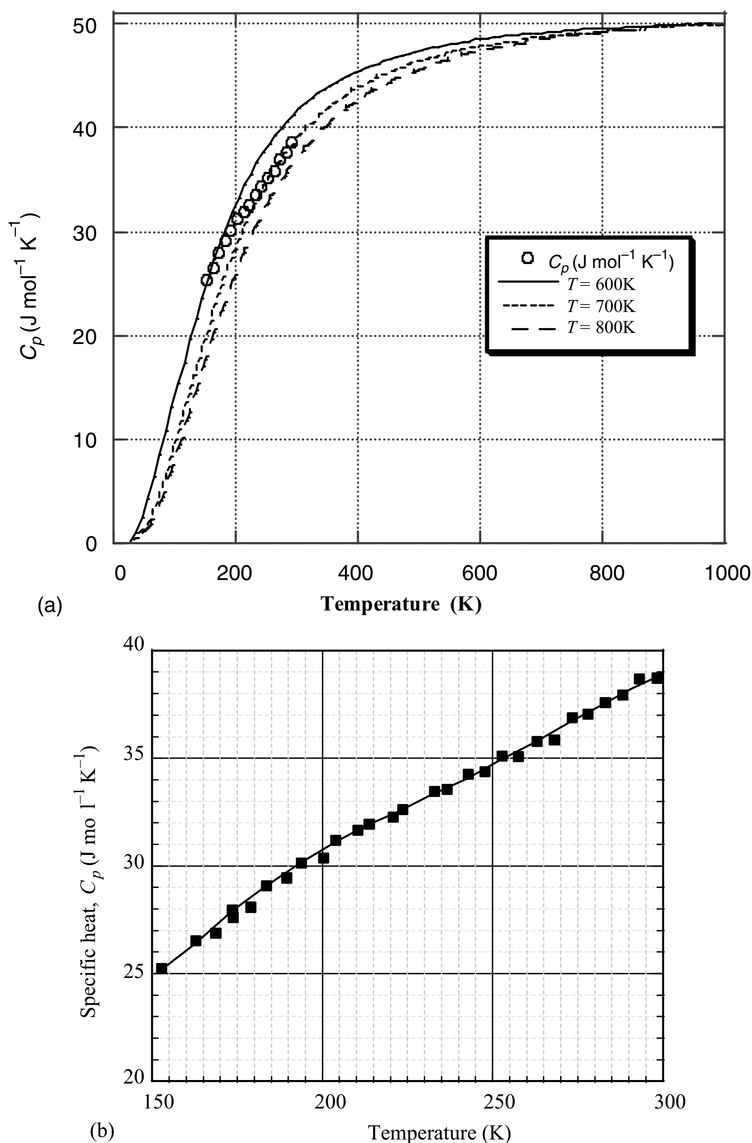

Figure 1.33 (a) The specific heat of InN with experimental data points, albeit in a small range, and the 600, 700, and 800 K Debye temperature fits. Data from Refs [88,127]. (b) Experimental specific heat of InN in a temperature range of 150–300 K [88,127].

material is used in conjunction with GaN if the associated technological difficulties can be overcome.

While the heat capacity of InN is $9.1 \pm 2.9 \times 10^{-3}$ cal mol^{-1} K^{-1}) at temperatures between 298 and 1273 K, the entropy is 10.4 cal mol^{-1} K^{-1} at 298.15 K. The

Table 1.32 Specific heat, C_p, of InN at constant pressure [88,127].

T (K)	C_p (J mol^{-1} K^{-1})
153	25.38
163	26.54
173	27.96
183	29.12
193	30.15
203	31.18
213	31.95
223	32.59
233	33.50
243	34.26
253	35.17
263	35.81
273	36.97
283	37.61
293	38.65

equilibrium partial pressure of N_2 above InN is about 1 atm at 800 K and it increases exponentially with temperature to 105 atm at 1100 K.

1.4.4
Brief Electrical Properties of InN

It is fair to state that reliable experimental data for the true electron mobility in InN is waiting to be obtained. As mentioned repeatedly, InN suffers from the lack of a suitable substrate material and high native defect concentrations that limit its quality. In addition, a large disparity of the atomic radii of In and N makes it more difficult to obtain InN of high quality. As a result, nitrogen vacancies are thought to lead to large background electron concentrations in InN. Because of all these factors, the electron mobilities obtained from various films vary very widely, as can be inferred from Table 1.33. The electron mobility in InN can be as high as 3000 cm^2 V^{-1} s^{-1}, perhaps even much higher, at room temperature [294]. A study of the electron mobility of InN as a function of the growth temperature indicates that the mobility of ultrahigh-vacuum electron cyclotron resonance radio-frequency magnetron sputtering (UHV ECR-RMS) grown InN can be as much as four times the mobility of conventionally grown (vacuum deposition) InN [295]. The dependence of the electron concentration and mobility on the InN film thickness grown on AlN and GaN buffer layers by plasma-enhanced MBE is shown in Figure 1.34.

Hall measurements in InN films grown on AlN buffer layers [300] that are in turn grown on sapphire indicated electron mobility to be 1310 cm^2 V^{-1} s^{-1} at room temperature [307] for MBE-grown and 830 cm^2 V^{-1} s^{-1} for OMVPE-grown material [304]. As discussed in Section 3.5 in conjunction with growth-related issues,

Table 1.33 A compilation of electron mobilities obtained in InN on different substrates and for various deposition conditions in InN as compiled in part in Ref. [296].

n-type carrier concentration (cm^{-3})	Carrier mobility ($cm^2 V^{-1} s^{-1}$)	Substrate	Deposition technique
$5–8 \times 10^{18}$	250 ± 50	Sapphire, silicon, various metals	Reactive sputtering
10^{20}	20	Sapphire	Reactive evaporation
$3–10 \times 10^{18}$	20–50	Glass, fused quartz	Reactive sputtering
$1–200 \times 10^{18}$	3	Fused quartz	Reactive sputtering
$2–80 \times 10^{20}$	35–50	Sapphire	CVD
5×10^{18}	20	Glass, NaCl	Reactive sputtering
6×10^{20}	2	Fused quartz	Cathodic sputtering
6×10^{16}	2	Glass, silicon, 304 stainless steel	RF ion plating
$7–70 \times 10^{16}$	730–3980	Glass, silicon	Reactive sputtering
3×10^{16} at 150 K	5000 at 150 K	Glass, silicon	Reactive sputtering
10^{20}	10	Glass	Reactive DC magnetron sputtering
4.8×10^{20}	38	Sapphire	Magnetron sputtering
$1–8 \times 10^{20}$	50	Sapphire	Plasma-assisted MOVPE
$1–10 \times 10^{20}$	50	Sapphire	MOVPE
$2–3 \times 10^{20}$	20–60	Sapphire, silicon, mica	Reactive RF magnetron sputtering
2×10^{20}	~100	GaAs	ECR-assisted MOMBE
10^{20}[ae]	220[a]	GaAs	Plasma-assisted MBE
2.0×10^{20}	100	GaAs	ECR-MOMBE [297]
5.98×10^{18}	363	Glass	Reactive RF magnetron sputtering [298]
5.0×10^{19}	700	Sapphire	MOVPE [299]
3.0×10^{18}	542	Sapphire	Migration-enhanced epitaxy [300]
8.8×10^{18}	500	Sapphire	MOMBE [301]
$2–3 \times 10^{18}$	800	Sapphire	MBE [302]
$\sim 10^{19}$	306	Glass, KBr	RF reactive ion sputtering [303]
1.0×10^{19}	830	Sapphire	RF MBE [304]
4×10^{17}	2100	Sapphire	MBE on thick HVPE GaN [305]
1.4×10^{18}	1420	Sapphire	Plasma-assisted MBE [306]
5×10^{16} (3×10^{16} at 150 K)[b]	2700 (5000 at 150 K)[b]		Sputtering [308]

[a] Zinc blende polytype.
[b] Have not yet been reproduced by others.

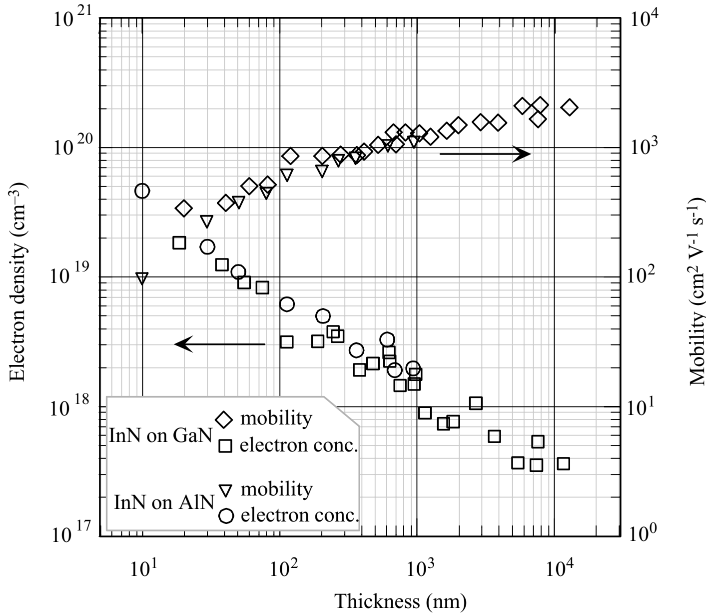

Figure 1.34 Electron density and mobility as a function of InN thickness. Samples grown on a GaN buffer are indicated by diamond and square symbols, and on an AlN buffer are indicated by circles and inverted triangles. The diamond and inverted triangle symbols indicate the electron mobility, whereas the squares and circle symbols indicate the electron concentration, all measured at room temperature. Courtesy of W.J. Schaff.

room-temperature mobilities increased to 2000 cm^2 V^{-1} s^{-1} in MBE-grown InN films. Some directions, such as the insertion of low-temperature intermediate layers or AlN buffer layers have been pointed out for improvement. Very high inadvertent donor concentrations, $>10^{18}$ cm^{-3}, seem to be one of the major problems for further progress. O_N and Si_{In} have been proposed to be the likely dominant defects responsible for high electron concentration based on their low formation energies. Additionally, H has been proposed [307] as the dominant impurity candidate for the state-of-the-art MBE-grown InN. Assuming that the measurements were performed flawlessly and interpreted, there clearly seems to be some way to go to reach the goal of a mobility of 2700 cm^2 V^{-1} s^{-1} at an electron concentration of 5×10^{16} cm^{-3} reported for RF reactive ion sputtered growth of InN nearly a few decades earlier [308].

Ensemble Monte Carlo calculations have been the popular tool to investigate the carrier velocity field characteristics theoretically. Although early application of this method to InN was done by O'Leary *et al.* [309], a more detailed calculation based on the full details of the conduction band structure appeared later in a paper by Bellotti *et al.* [310]. A peak electron drift velocity of 4.2×10^7 cm s^{-1} has been predicted at an electric field of 65 kV cm^{-1}, substantially higher than that in GaN,

with a noticeable anisotropy for field direction parallel or perpendicular to the basal plane. The velocity is seen to decrease to $3.4\times10^7\,\mathrm{cm\,s^{-1}}$ with an increase of field to $70\,\mathrm{kV\,cm^{-1}}$ and reach a value of 2.0×10^7–$1.0\times10^7\,\mathrm{cm\,s^{-1}}$ at the onset of impact ionization, for field directions parallel and perpendicular to the basal plane, respectively. The calculated low-field mobility is $\sim3000\,\mathrm{cm^2\,V^{-1}\,s^{-1}}$. This study claims to report the first calculation of high-field electron transport in InN. Electron–phonon coupling would hurt the high-field velocity as it seems to be the case in GaN, see Volume 3, Chapter 3 for details.

Another interesting aspect of electron transport is its transient behavior, which is relevant to short channel devices with dimensions smaller than 0.2 μm, where a significant overshoot is expected [311] to occur in the electron velocity over the steady-state drift velocity. In yet another calculation, Foutz *et al.* [311] found that of the three III nitride binaries, GaN, InN, and AlN, this overshoot is most pronounced in InN and occurs above a critical field of $65\,\mathrm{kV\,cm^{-1}}$. The peak velocity at this field is $4.2\times10^7\,\mathrm{cm\,s^{-1}}$ and the velocity overshoot is retained over longer distances as compared to that for GaN and AlN.

1.4.5
Brief Optical Properties of InN

As mentioned in the opening statements for Section 1.4, while the bandgap value reported in the early stages of InN development dating back to as early as 1980s, a controversy developed as to the true value of the InN bandgap developed. This is detailed in Section 2.9.2. However, a brief treatment is provided here for completeness. Excellent reviews chronicle and detail the evolution of the controversy in InN [278,279]. A number of groups have described optical measurements performed on InN [25,313,314]. Early values of the room-temperature InN direct bandgap ranged from 1.7 to 2.07 eV. A value of 1.89 eV was measured by optical absorption by Tansley and Foley [308], who also measured the infrared absorption of InN and observed an unidentified donor level approximately 50–60 meV below the conduction band edge. Reflectance spectroscopy on single-crystal material, using synchrotron radiation over the range 2–20 eV[315], later extended to 130 eV [316], was performed to determine the optical parameters of InN.

A few studies of the interband optical absorption performed on InN thin films deposited by sputtering techniques [271] and OMVPE [103], were found consistent with a fundamental energy gap of about 2 eV. However, weak photoluminescence peaks with energies ranging from 1.81 to 2.16 eV were observed for InN grown on Si substrates later on [317]. In one such case, an emission centered at 1.86 eV at a temperature below 20 K was seen, whereas the reflectance measurement showed a strong plasma reflection at 0.7 eV, corresponding to an effective mass of $0.12m_0$. Another branch of studies shows that in improved InN films a strong photoluminescence transition at energies around 1 eV [30,318,319] appears. Observing that the position of the photoluminescence energy agrees with the onset of strong absorption, the optical transition at about 1 eV has been attributed to the fundamental bandgap [319].

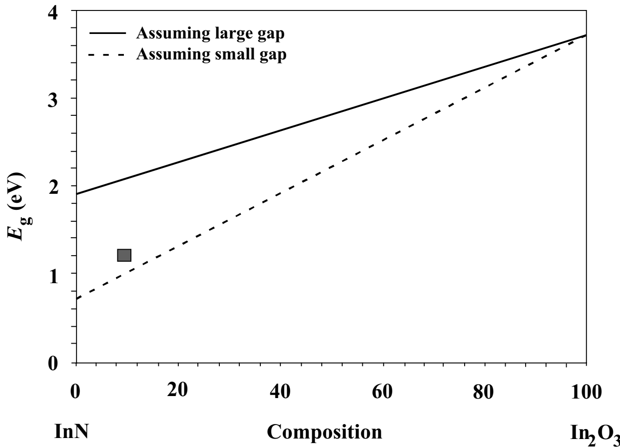

Figure 1.35 Vegard's law plot of InN–In_2O_3 pseudobinary alloy system with both 0.7 and 1.9 eV bandgaps shown (dashed lines and solid line, respectively) versus O composition reaching In_2O_3, which has a bandgap of 3.75 eV reported in Ref. [320]. Also shown is the calculated (using LCAO) bandgap with 10% oxygen if O-free bandgap is 0.7 eV [278,322].

Following the wide acceptance of the above-mentioned data by the community, a couple of crystal growth groups, often in collaborations with others who focused on characterization, began to question the nearly 1.9–2.0 eV bandgap, because the newer and supposedly more improved samples showed a strong emission at much smaller energies, primarily around 0.7–0.8 eV. Those latter groups argued that the early samples did not show efficient PL near the band edge and had to have been contaminated with O to support the earlier measurements. One should, however, keep in mind that In_2O_3 has a bandgap of 3.75 eV [320], and if the Vegard's law is applicable it would take some 35% O in InN to boost its bandgap from say 0.8 to 1.9 eV, which is substantial, as shown in Figure 1.35. Also shown is the bandgap of InN for 10% O contamination assuming an O-free bandgap of 0.7 eV [321,322]. Not only large amounts O is needed, but also that O must form an alloy with InN. Clearly, the assignment of the 1.9 eV bandgap to O, on the premise that the bandgap for O-free InN is 0.7–0.8 eV, requires large amounts of O, which is not supported by experiments, as discussed in detail in Section 2.10.1.

To account for the 1.9 eV measured bandgap, the proponents of the 0.7 eV bandgap also suggested that the former result could be accounted for by Moss–Burstein blue shift owing to high electron concentration. This effect relates to semiconductors where the electron concentration is larger than the density of states and the Fermi level is actually in the conduction band itself. The extent of the penetration naturally depends on the electron concentration. Consequently, the measured apparent optical gap is skewed upward. This possibility was suggested in 1974 by Trainor and Rose [323] and has been the topic of an extensive study using In_2O_3 as the model wide bandgap material [320]. What accompanies the Moss–Burstein shift is the

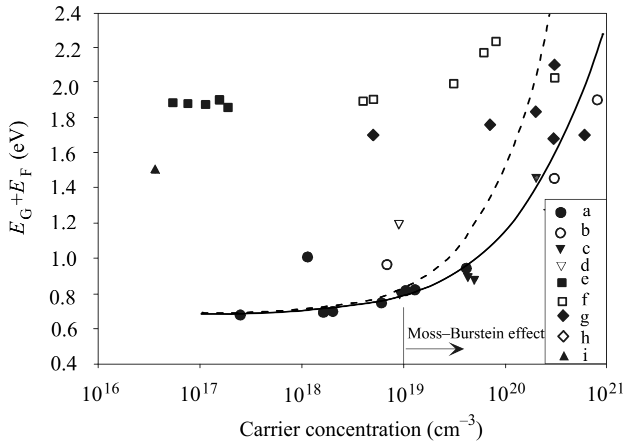

Figure 1.36 The measured bandgap of InN (combination of the bandgap and the Moss–Burstein shift) deduced from absorption measurements versus the carrier concentration reported by various groups. The solid line shows the expected blue shift in the bandgap because of Moss–Burstein shift. Solid and dashed lines indicate nonparabolic and parabolic theories, respectively. (a) Ref. [341]; (b) Ref. [324]; (c) Refs [274,318]; (d) Ref. [331]; (e) Ref. [271]; (f) Refs [303,325]; (g) Refs [131,272,326,327]; (h) Ref. [328]; (i) Ref. [329]. Collated by Butcher and Tansley [278,279].

bandgap renormalization, which is a red shift, caused by tail states extending into the bandgap and counters the former effect to some extent. Here too there is a controversy in that the samples of older times did not indicate large Moss–Burstein effect, which has been attributed by the proponents of the 0.7 eV bandgap, as having been heavily reduced owing to band tail states.

Butcher [278] collated the apparent bandgap (presumably a combination of the bandgap with its band tailing and Moss–Burstein effect) measured by optical absorption and the electron concentration data for a large group of samples as shown in Figure 1.36. Although an argument for Moss–Burstein effect can be made for samples with high carrier concentrations, the same cannot be applied to a good many samples exhibiting the large bandgap while having low carrier concentration. To be thorough, one should recognize that many of the InN samples contained in Figure 1.36 with low carrier concentrations are heavily compensated, casting some amount of uncertainty as well. Turning the argument around and assuming that the large bandgap data are more dependable, the low bandgap data could be explained with some defect level in In-rich material or by Mie resonant absorption due to In inclusions. These are discussed in Section 2.10.1.

After discussing the controversy regarding the bandgap and making many references to the low bandgap measured in InN, let us briefly discuss the data obtained in layers grown by MBE under In-rich conditions, which exhibit the so-called small bandgap. The optical absorption data in InN, purportedly having 0.7–0.8 eV bandgap, show an onset at ~0.78 eV not near 1.9–2.0 eV, as shown in

Figure 1.37a. The absorption coefficient increases gradually with increasing photon energy and at the photon energy of 1 eV it reaches a value of more than $10^4\,cm^{-1}$. This high value is consistent with an interband absorption in semiconductors. Moreover, the integrated PL intensity increased linearly with excitation intensity over three orders of magnitude, lending more credence to the notion that the observed nonsaturable peak relates to the fundamental interband transition. The absorption squared versus the energy plots used to obtain the apparent bandgap in a semiconductor with very high carrier concentration underestimates the bandgap owing to band tailing. Briot *et al.* [330,331] estimated a bandgap near 1.2 eV from the absorption data while taking the large carrier concentration of $10^{19}\,cm^{-3}$ into account. This, however, does not account for the large discrepancy between the 0.7–0.8 eV group and 1.8–2.0 eV group.

The free-electron concentration in this sample was measured by Hall effect to be $5\times10^{18}\,cm^{-3}$. Figure 1.37a also shows that the samples exhibit intense room-temperature luminescence at energies close to the optical absorption edge. Additionally, the 77 K photoreflectance (PR) spectrum exhibits a transition feature at 0.8 eV with a shape characteristic for direct gap interband transitions. Consistent with the absorption data, no discernible change in the PR signal near 2 eV is seen. The simultaneous observations of the absorption edge and PL and PR features at nearly the same energy led Wu *et al.* [30] to argue that this energy position of $\sim$0.78 eV is the fundamental bandgap of InN. This value is very close to the fundamental gap for InN reported by the other group, Davydov *et al.* [319], in favor of the smaller bandgap for InN. Tsen *et al.* [332] studying nonequilibrium optical phonons in a high-quality single-crystal MBE-grown InN with picosecond Raman spectroscopy reached the conclusion that their results are not consistent with the large bandgap of InN. Using the possible phonon emission allowed by energy and momentum conservations for a range of excitation photon energies, they argued that their observations are consistent with the small bandgap of InN. The basis of the argument is that if the bandgap energy were 1.89 eV, no nonequilibrium phonons could be observed, contradicting the observation of Tsen *et al.* [332], details of which are discussed in Section 2.10.1.

Figure 1.37b shows the room-temperature electron mobility, the peak energy of PL, and the transition energy determined by PR as functions of electron concentration, showing that the transition energies increase with increasing free-electron concentration. This indicates that the transitions from higher energy occupied states in the conduction band contribute significantly to the PL spectrum. The PL energy as a function of pressure shows a linear pressure coefficient of 0.6 $meV\,kbar^{-1}$, which is considerably smaller than that for other III–V compounds. For comparison, the pressure coefficient of GaN is 4.3 $meV\,kbar^{-1}$ [333], $Al_xGa_{1-x}N$ is 4.1 $meV\,kbar^{-1}$ for $0.12 < x < 0.6$ [334], and GaAs is 11 $meV\,kbar^{-1}$ [335], as compiled by Wu *et al.* [30]. The sapphire substrate on which the InN layer is grown has a larger bulk modulus than InN, which will reduce hydrostatic pressure transmission to the InN film providing that the film remains coherently strained. Using experimental elastic constants for sapphire and theoretical elastic constants for InN, Wu *et al.* [30] estimated the correction factor for coherently strained InN on sapphire to be 1.45, leading to between 0.6 and 0.9 $meV\,kbar^{-1}$ for the bandgap change. More work is needed to shed light on this unusually low pressure dependence although

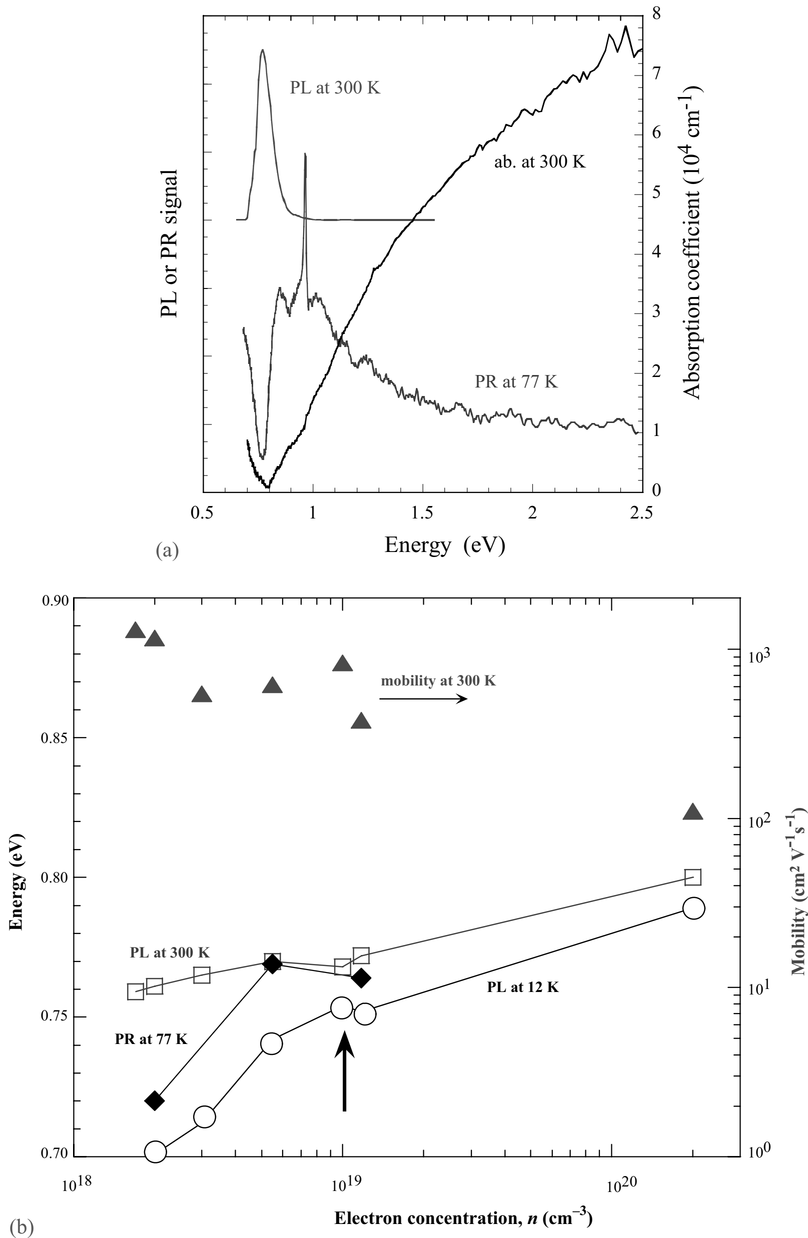

Figure 1.37 (a) Optical absorption (300 K), PL (300 K), and PR (77 K) spectra of a typical InN sample. This sample is undoped with room-temperature electron concentration of 5.48×10^{18} cm^{-3}. The spike on the PR spectrum at 0.97 eV is an artifact due to the light source used in the PR measurement. (b) Room-temperature mobility, PL peak energy (300 and 12 K), and the critical energy determined by PR (77 K) as a function of free-electron concentration. The sample with $n = 1 \times 10^{19}$ cm^{-3} (indicated by an arrow) is the Ritsumeikan sample.

studies of InGaN showing smaller pressure dependence as the InN concentration is increased are consistent with data on InN [336].

Tyagai *et al.* [337] performed reflection and transmission measurements in InN with electron concentration larger than $10^{20}\,\mathrm{cm}^{-3}$. They were able to estimate an effective mass of $m_e^* = 0.11m_0$ and an index of refraction of $n = 3.05 \pm 0.05$, which is in reasonable agreement with the value measured by Tsen *et al.* [332]. The long-wavelength limit of the *refractive index* was reported to be 2.88 ± 0.15. The temperature dependence of the InN bandgap indicates a bandgap blue shift of 23 meV from 300 to 77 K [291,338]. Inushima *et al.* [132] reported the effective mass to be $0.24m_0$ in InN grown by UV-assisted atomic layer epitaxy under atmospheric pressure. Using infrared spectroscopic ellipsometry, Kasic *et al.* [339] arrived at a value of $m^* = 0.14m_0$ in an MBE-grown InN layer having an electron concentration of $n = 2.8 \times 10^{19}\,\mathrm{cm}^{-3}$. Using surface reflection of extrinsic semiconductors in the infrared region by the free-carrier plasma, used earlier for GaN [340], Wu *et al.* [341] determined the effective mass of the free carriers to be $0.07m_0$ at the bottom of the conduction band. This method hinges on the knowledge of the plasma frequency, electron concentration, and optical dielectric constant through the relation

$$m^* = \frac{ne^2}{\varepsilon\varepsilon_\infty \omega_P^2}, \tag{1.23}$$

where all the terms have their usual meanings and ω_P represents the plasma frequency. Using $\varepsilon_\infty = 6.7$ (compares with figures in the range of 5.8–9.3 tabulated in Table 1.21) and utilizing infrared reflection measurements for a series of samples with different carrier concentrations, Wu *et al.* [341] arrived at an electron effective mass value of $0.07m_0$ at the bottom of the conduction band.

The temperature dependence of the bandgap of InN indicates a bandgap temperature coefficient of [342]

$$(\mathrm{d}E_g/\mathrm{d}T) = 1.8 \times 10^{-4}\,\mathrm{eV\,K^{-1}}. \tag{1.24}$$

1.5 Ternary and Quaternary Alloys

Many important GaN-based devices involve heterostructures as the primary means of achieving an improved performance. Ternary alloys of wurtzite polytypes of GaN, AlN, and InN have been obtained in the continuous alloy systems whose direct bandgap ranges from the old value for InN of 1.9 eV (the new value is approximately 0.7 eV according to Ref. [30]) for InN to 6.2 eV for AlN (the new value is approximately 6 eV). For an in-depth understanding of the physical mechanisms that underlie their operations, the properties of these alloys need to be extensively studied. Many of these properties such as the energy bandgap, effective masses of the electrons and holes, and the dielectric constant depend on the alloy composition. Although measured data for these parameters in InGaN and InAlN have been obtained, they are still not very precise (for AlGaN see Ref. [157] and for InGaN see Ref. [343]). Yamasaki *et al.* [344] have reported on p-InGaN. More research is necessary to confirm

these conclusions regarding p-AlN and p-InGaN. AlN and GaN are slightly lattice mismatched (2.4%). It has been noted that, for many devices, only small amounts of AlN are needed in the GaN lattice to provide sufficient carrier and optical field confinements.

1.5.1 AlGaN Alloy

The ternary alloys of wurtzite and zinc blende polytypes of GaN with AlN form a continuous alloy system with a wide range of bandgap and a small change in the lattice constant. An accurate knowledge of the compositional dependence of the barrier as well as material is a requisite in attempts to analyze heterostructures in general and quantum wells (QWs) and superlattices in particular. The barriers can be formed of AlGaN or AlN, and while dependent on the barrier material, the wells can be formed of GaN or AlGaN layers. The compositional dependence of the lattice constant, the direct energy gap, and electrical and CL properties of the AlGaN alloys were measured by Yoshida *et al.* [345]. A similar investigation followed a few years later [346]. On the structural side, namely the calculated lattice parameter of this alloy, predictions indicate that Vegard's law applies [347] (also reviewed in Ref. [17]):

$$a_{\mathrm{Al}_x\mathrm{Ga}_{1-x}\mathrm{N}} = 3.1986 - 0.0891x\ \text{Å} \quad \text{and} \quad c_{\mathrm{Al}_x\mathrm{Ga}_{1-x}\mathrm{N}} = 5.2262 - 0.2323x\,\text{Å}\,. \tag{1.25}$$

By bringing to bear various tools such as HRXRD, the experimental data for various AlGaN support the applicability of Vegard's law in that the experimental data $a_{\mathrm{Al}_x\mathrm{Ga}_{1-x}\mathrm{N}} = (3.189 \pm 0.002) - (0.086 \pm 0.004)x$ Å and $c_{\mathrm{Al}_x\mathrm{Ga}_{1-x}\mathrm{N}} = (5.188 \pm 0.003) - (0.208 \pm 0.005)x$ Å are within about 2% of those predicted by linear interpolation, Vegard's law. However, the bond lengths exhibit a nonlinear behavior, deviating from the virtual crystal approximation. Essentially, the nearest neighbor bond lengths are not as dependent on composition as might be expected from the virtual crystal approximation.

The ensuing investigations to pin down the compositional dependence of the bandgap of this important alloy continued with conflicting results. These are discussed below following the presentation of an empirical expression used to relate the bandgap to composition.

The compositional dependence of the principal bandgap of $\mathrm{Al}_x\mathrm{Ga}_{1-x}\mathrm{N}$ can be calculated from the following empirical expression providing that the bowing parameter, b, is known accurately:

$$E_g(x) = xE_g(\mathrm{AlN}) + (1-x)E_g(\mathrm{GaN}) - bx(1-x), \tag{1.26}$$

where $E_g(\mathrm{GaN}) = 3.4$ eV, $E_g(\mathrm{Al\,N}) = 6.1$ eV, x is the AlN molar fraction, and b is the bowing parameter.

An earlier compilation by Amano *et al.* [348] already pinpointed the discrepancy in the reported bowing parameters. For example, Yoshida *et al.* [349] concluded that, as the AlN mole fraction increases, the energy bandgap of $Al_xGa_{1-x}N$ deviates upward, implying a negative value for the bowing parameter b. This contrasts the data of Wickenden *et al.* [350] that support a vanishing bowing parameter b. Koide *et al.* [351] observed that the bowing parameter is positive and that the bandgap of the alloy deviates downward indicating a positive value for the bowing parameter. To determine the bowing parameter accurately, as investigations expanded [352–362] so did the dispersion in the bowing parameters ranging from -0.8 eV (upward bowing) to $+2.6$ eV (downward bowing), as compiled by Yun *et al.* [363].

Much of this spread emanates from the likely dispersion in the quality of $Al_xGa_{1-x}N$, thus erroneous determination of its bandgap and to a lesser extent its lattice parameter. Because the genesis of PL transitions could be nonintrinsic, a technique relying on absorption or modulated photoreflectance is more accurate in the determination of bandgap energy. Using X-ray and surface analytical techniques, such as secondary ion mass spectroscopy (SIMS) and Rutherford backscattering (RBS), for determining composition, reflectance, and absorption for bandgap for AlGaN layers spanning the entire compositional range, Yun *et al.* [363] revisited the bowing parameter. The results of this study, shown in Figure 1.38 in the form of AlGaN bandgap versus the composition, yield a bowing parameter of $b = 1.0$ eV for the entire range of alloy compositions. In this figure, the solid line represents a least square fit to the data, which in turn are depicted by solid circles. X-ray diffraction peaks generally tend to be wider for alloy compositions around the midway point that is the most likely source of error in determining the bowing parameter. The situation is exacerbated by the fact that the data points near the middle of the compositional range determine the bowing parameter to a much larger extent, as near each of the binary ends the compositional variation approaches the linear line. It is still possible that as the quality of the films improves smaller bowing parameters could result. A bowing parameter as low as 0.7 has been reported.

Hall measurements for n-$Al_{0.09}Ga_{0.91}N$ demonstrated a carrier concentration of 5×10^{18} cm^{-3} and a mobility of 35 cm^2 V^{-1} s^{-1} at 300 K [364]. This measurement did not reveal any temperature-dependent mobility of n-$A1_{0.09}Ga_{0.91}N$. Other Hall measurements [365] on Mg-doped p-$Al_{0.08}Ga_{0.92}N$ grown by MOVPE, however, addressed the temperature dependence of the mobility [365]. They indicate that the hole mobility decreases with increasing temperature, reaching a value of about 9 cm^2 V^{-1} s^{-1} for a doping density of 1.48×10^{19} cm^{-3}. This low mobility is ascribed to a high carrier concentration and the intergrain scattering present in the samples. While the lattice constant was studied, it was observed to be almost linearly dependent on the AlN mole fraction in AlGaN.

Until recently, the resistivity of unintentionally doped AlGaN was believed to increase so rapidly with increasing AlN mole fraction that AlGaN became almost insulating for AlN mole fractions exceeding 20%. As the AlN mole fraction increased from 0 to 30%, the n-type carrier concentration dropped from 10^{20} to 10^{17} cm^{-3} and the mobility increased from 10 to 30 cm^2 V^{-1} s^{-1}. An increase in

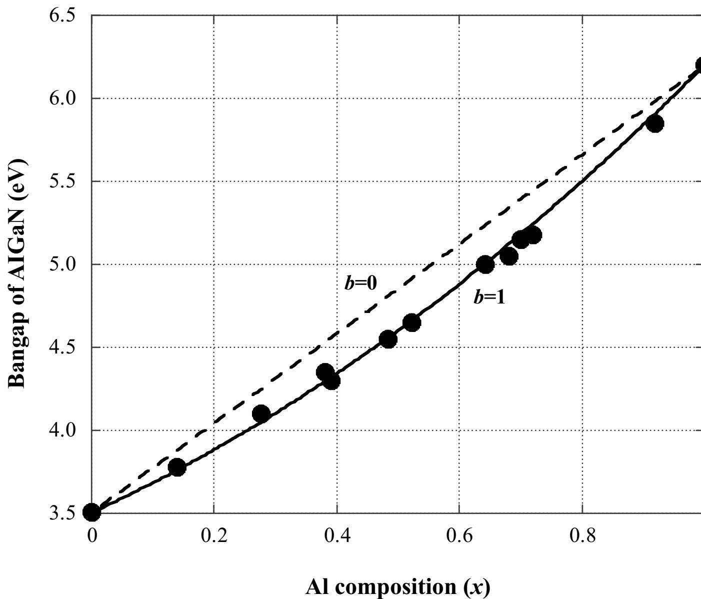

Figure 1.38 Experimental data of energy bandgap of AlGaN ($0 \leq x \leq 1$), plotted as a function of Al composition (solid circle), and the least squares fit (solid line) giving a bowing parameter of $b = 1.0$ eV. The dashed line shows the case of zero bowing. As the quality of the near 50 : 50 alloy layers get better, giving rise to sharper X-ray and PR data, smaller bowing parameters may ensue. Bowing parameters as low as 0.7 have been reported.

the native defect ionization energies with increasing AlN may possibly be responsible for this variation. Our knowledge of the doping characteristics of AlGaN is still incomplete. For example, it is not known how the dopant atoms such as Si and Mg respond to the variation of the AlN mole fraction in AlGaN. However, it was suggested that as the AlN mole fraction increases, the dopant atom moves deeper into the forbidden energy bandgap. AlGaN with an AlN mole fraction as high as 50–60% may be doped by both n- and p-type impurity atoms. The ability to dope a high mole fraction AlGaN, especially when low-resistivity p-type material is required, is important because it may otherwise restrict the overall characteristics of devices such as laser diodes. A low AlN mole fraction in AlGaN has been considered sufficient for acceptable optical field confinement. However, this must be addressed before the potential of AlGaN with respect to the other wide bandgap semiconductors is fully realized.

1.5.2
InGaN Alloy

The growth of high-quality InN and an enumeration of its fundamental physical properties remain somewhat elusive as compared to the other alloy, AlGaN.

Notwithstanding the difficulties in technology, InGaN is already an integral part of important device designs. $In_xGa_{1-x}N$ (x is the InN mole fraction) is not any less important than $Al_xGa_{1-x}N$ for the fabrication of electrical and optical devices, such as LEDs and lasers, which can emit in the violet or blue wavelength range. It can be a promising strained QW material for these devices, but added complexities such as the phase separation and other inhomogeneities make the determination of the bandgap of InGaN versus the composition a very difficult task.

The first growth of single crystalline InGaN by MOVPE was realized by Nagatomo *et al.* in 1989 [366] and Matsuoka *et al.* [367], followed by Yoshimoto *et al.* in 1991 [368]. Since then, considerable effort has been expended worldwide on this material, as it is responsible for emission in the near-UV, violet, blue, and green colors of the optical spectrum. High-efficiency blue and green LEDs utilizing InGaN active layers are commercially available. This material, however, is not as easy to grow because of the high vapor pressure of N on In and also mismatch between the large In atom and the small N atom. To mitigate this problem, V/III ratios in excess of 20 000, increasing with InN mole fraction, as well as reduced growth temperatures are employed. Matsuoka *et al.* [369] discovered that lowering the growth temperature to 500 °C from nominal temperatures such as 800 °C increased the In content in the layers, but at the expense of reduced quality. Efforts to increase the In concentration by raising the indium precursor temperature or the carrier gas flow rate resulted in the degradation of the structural and surface morphology so much that In droplets were formed on the surface [370].

The great disparity between Ga and In could lead to issues such as phase separation and instabilities. In this vein, Ho and Stringfellow [371] investigated the temperature dependence of the binodal and spinodal boundaries in the InGaN system with a modified valence force field model. The calculation of the extent of the miscibility gap yielded an equilibrium InN mole fraction in GaN of less than 6% at 800 °C [371]. In the annealing experiments in argon ambient, the phase separation in an $In_xGa_{1-x}N$ alloy with $x \geq 0.1$ was observed at temperatures between 600 and 700 °C [372], pointing to the large region of solid immiscibility of these alloys. However, under nonequilibrium growth conditions, $In_xGa_{1-x}N$ layers were grown in the entire range of compositions. But, the decomposition into two phases upon annealing of the $In_xGa_{1-x}N$ alloys ($x = 0.11$ and $x = 0.29$) at 600 and 700 °C was observed pointing to the existence of the miscibility gap. For some alloys with $x = 0.6$, the phase separation could not be observed at 600 °C. Above 800 °C, the alloy samples with $x = 0.1$ actively evaporated from the substrate. These results suggest that the solid solutions are grown in metastable conditions and decomposed under annealing conditions.

Koukitu *et al.* [373] performed a thermodynamical analysis of InGaN alloys grown by MOCVD. They found that in contrast to other III–III–V alloy systems where the solid composition is a linear function of the molar ratio of the group III metalorganic precursors at constant partial pressure of group V gas, the solid composition of InGaN deviates significantly from a linear function at high substrate temperatures.

Kawaguchi *et al.* [374] reported a so-called InGaN composition pulling effect in which the indium fraction is smaller during the initial stages of growth but increases with increasing growth thickness. This observation was to a first extent independent

of the underlying layer, GaN or AlGaN. The authors suggested that this effect is caused by strain caused by the lattice mismatch at the interface. They found that a larger lattice mismatch between InGaN and the bottom epitaxial layers was accompanied by a larger change in the In content. What one can glean from this is that the indium distribution mechanism in InGaN alloy is caused by the lattice deformation because of the lattice mismatch. With increasing thickness, the lattice strain is relaxed owing to the formation of structural defects and roughness, which weakens the composition pulling effect.

Other substrates have also been used for InGaN growth. It has been reported that the crystalline quality of InGaN is superior when grown with the composition that lattice matches ZnO substrate to that grown directly on (0 0 0 1) sapphire substrate [368,369]. In the same investigations, it was observed that InGaN films grown on sapphire substrates using GaN as buffer layers exhibited much better optical properties than InGaN films grown directly on sapphire substrates [375]. For a given set of growth conditions, an increase of InN in InGaN can be achieved by reducing the hydrogen flow [376]. As in the case of AlGaN, the calculated lattice parameter of this alloy follows Vegard's law [347] (also reviewed in Ref. [17]):

$$a_{\mathrm{In}_x\mathrm{Ga}_{1-x}\mathrm{N}} = 3.1986 + 0.3862x\ \text{Å} \quad \text{and} \quad c_{\mathrm{In}_x\mathrm{Ga}_{1-x}\mathrm{N}} = 5.2262 + 0.574x\ \text{Å}. \tag{1.27}$$

By bringing to bear various tools such as HRXRD, the experimental data for various AlGaN support the applicability of Vegard's law in that the experimental data $a_{\mathrm{Al}_x\mathrm{Ga}_{1-x}\mathrm{N}} = (3.560 \pm 0.019) + (0.449 \pm 0.019)x\,\text{Å}$ and $c_{\mathrm{Al}_x\mathrm{Ga}_{1-x}\mathrm{N}} = (5.195 \pm 0.002) + (0.512 \pm 0.006)x\,\text{Å}$ are within about 2% of that predicted by linear interpolation, Vegard's law.

As in the case of AlGaN but to a larger extent, the bond lengths exhibit a nonlinear behavior, deviating from the virtual crystal approximation. Essentially, the nearest neighbor bond lengths are not as dependent on composition as might be expected from the virtual crystal approximation.

The compositional dependence of InGaN bandgap is a crucial parameter in designs of any heterostructure utilizing it. As such, the topic has attracted a number of theoretical [377–382] and experimental (to be discussed below) investigations and reports. Similar to the case of AlGaN, the energy bandgap of $\mathrm{In}_x\mathrm{Ga}_{1-x}\mathrm{N}$ over $0 \le x \le 1$ can be expressed by the following empirical expression:

$$\begin{aligned} E^{\mathrm{g}}_{\mathrm{In}_x\mathrm{Ga}_{1-x}\mathrm{N}} &= xE^{\mathrm{g}}_{\mathrm{InN}} + (1-x)E^{\mathrm{g}}_{\mathrm{GaN}} - b_{\mathrm{InGaN}}x(1-x) \\ &= 0.7x + 3.4(1-x) - b_{\mathrm{InGaN}}x(1-x)\ \mathrm{eV}, \end{aligned} \tag{1.28}$$

where $E^{\mathrm{g}}_{\mathrm{GaN}} = 3.40\,\mathrm{eV}$ and $E^{\mathrm{g}}_{\mathrm{InN}} = 1.9\,\mathrm{eV}$ or near $0.7\,\mathrm{eV}$. For the nomenclature $\mathrm{Ga}_x\mathrm{In}_{1-x}\mathrm{N}$, the terms x and $1-x$ in Equation 1.28 must be interchanged. Another point of caution is that the sign in front of the bowing parameter is changed to positive in some reports. When a comparison is made, the sign of the b parameter must be changed.

An earlier investigation of InGaN bowing parameter for alloys with small concentrations of InN by Nakamura *et al.* [383] led to a bowing parameter of 1.0, which is in disagreement with the value of 3.2 reported by Amano *et al.* [348], who took into

consideration the strain and piezoelectric fields as well. It should be mentioned that these reports dealt with the Ga-rich side of the alloy. To obtain a fit over a large range of compositions, a composition-dependent bowing parameter has been suggested. As the InGaN is grown on GaN, there are many complicating factors, such as the piezoelectric effect and the nonuniform strain; the impact of the former can be made negligible by growing thick films. Moreover, compositional inhomogeneities due to partial phase separation are present. If the strain caused by the lattice mismatch were uniform, it would be compressive due to the InN lattice constant being 11% larger than that of GaN with an accompanying blue shift of the band edge. Herein lies the dilemma faced by the experimentalists. Growing thick films could minimize the extent of strain and the piezoelectric effect. However, this is nearly an intractable proposition. The relaxation value of the lattice constant and the origin of the optical transitions must be known accurately to determine the bandgap versus composition dependence. Absorption and/or reflection measurements, provided that the absorption edge is sharp, are more useful in determining the bandgap but again require thick and/or high-quality films. Detailed X-ray reciprocal-space mapping undertaken by Amano *et al.* [348] purportedly indicated that InGaN wells and even somewhat thicker InGaN layers grown on GaN buffer layers are coherently strained; a conclusion reached by the observation that the in-plane lattice constants of GaN and InGaN match. At the same time, though, the layer thicknesses well exceeded the calculated critical values.

When a bandgap of $\sim$1.9 eV for InN is assumed as the end point value for InN in regard to InGaN ternary, large and/or more than one bowing parameter is required to fit the compositional dependence of the bandgap energy. For example, a bowing parameter of 2.5 eV was obtained from optical absorption measurements and a value of 4.4 eV was obtained from the position of the emission peaks [384]. Nagatomo *et al.* [366] noted that the $In_xGa_{1-x}N$ lattice constant varies linearly with the In mole fraction up to at least $x = 0.42$, but it violates the *Vegard's law* for $x > 0.42$, which may be caused by erroneous determination of the composition and illustrates well the problem at hand. Even additional investigations did not agree on the exact value of the bowing parameter. For example, a value for $b_{InGaN} = 3.9 \pm 0.5$ eV was reported when 0.9 eV was used for the InN gap, but the bowing parameter had to be increased to 5.1 ± 0.4 eV when 1.9 eV was used for the InN gap [385]. Using the bandgap determined by PL, a bowing parameter of 4.5 eV was also reported [386]. However, when reflectivity measurements together with PL data corrected for Stokes shift were used, $b_{InGaN} = 2.5 \pm 0.7$ eV was obtained for 0.9 eV bandgap of InN and $b_{InGaN} = 3.5 \pm 0.7$ eV for 1.9 eV InN bandgap. Optical transmission measurements led to a bowing parameter of 8.4 eV [387]. At least one theoretical effort resulted in a bowing parameter of 1.2 eV [377]. In fact, linear bandgap dependence on composition with a slope of -3.57 eV for up to 25% InN content has also been reported [388]. Linear dependence with a slope of -4.1 eV for InN mole fraction, $x < 0.12$, has been reported in another publication as well [389]. Wu *et al.* [390] visited the bandgap dependence of InGaN on composition by considering $\sim$0.8 eV for the bandgap of the end binary InN. Figure 1.39 shows the composition dependence of the bandgap of InGaN, determined by using photomodulated transmission [391] and optical absorption [392] measurements, as a

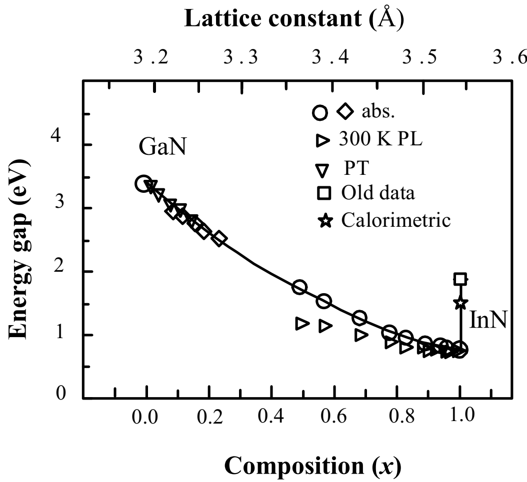

Figure 1.39 PL peak energy and bandgap of InGaN determined by optical absorption as a function of composition, as compiled in Ref. [390], including previously reported data for InN. The solid curve shows the fit to the bandgap energies (determined by absorption and phototransmission) using a bowing parameter $b = 1.43$ eV [390].

function of GaN fraction. The data near the GaN binary end include those reported by Pereria *et al.* [392], Shan *et al.* [390], and O'Donnel *et al.* [393].

Care was taken by observing the dependence of squared absorption coefficient on light probe energy and seeing nearly a linear dependence to gain confidence on the measured bandgap and also confirming the values by bandgaps determined by photomodulated transmission measurements. The slight deviation from linearity near the InN end of the ternary has been attributed to the nonparabolicity of the conduction band caused by the $k \cdot p$ interaction between the Γ_6 symmetry conduction band and the Γ_8 symmetry valence bands. As shown by the solid curve in Figure 1.39, the compositional dependence of the bandgap in the entire composition range can be well fit by a bowing parameter of $b = 1.43$ eV. Shown in Figure 1.39 with dashed line is the fit to the empirical expression using energy of 1.9 eV for InN and bowing parameter of 2.63 eV to demonstrate that it does represent the Ga-rich side of the compositions well. However, the bowing parameter of 1.43 eV that is good for the entire compositional range is the one that utilizes 0.77 eV for the bandgap of InN.

In an investigation with a different set of objectives, Yoshimoto *et al.* [368] studied the effect of growth conditions on the carrier concentration and transport properties of $In_xGa_{1-x}N$. They observed that if the deposition temperature is increased from 500 to 900 °C, $In_xGa_{1-x}N$ grown on sapphire with $x \approx 0.2$ suffers from a reduction in carrier concentration from 10^{20} to 10^{18} cm^{-3}, but gains from an increase in the carrier mobility from less than 10 to 100 cm^2 V^{-1} s^{-1}. The same group later noted that this trend does not change if the films are grown on ZnO substrates instead of sapphire [369]. They could achieve good InGaN material with In mole fractions as

large as 23%. Nakamura and Mukai [394] discovered that the film quality of $In_xGa_{1-x}N$ could be significantly improved if these films are grown on high-quality GaN films. Thus, from the reports cited above it may be concluded that the major challenge for obtaining high-mobility InGaN is to find a compromise in the growth temperature, because InN is unstable at typical GaN deposition temperatures. This growth temperature would undoubtedly be a function of the dopant atoms, as well as the method (MBE, OMVPE, etc.) used for the growth. This is evident from a study by Nakamura *et al.*, who have since expanded the study of InGaN employing Si [395] and Cd [396] as dopants. A review of various transport properties of GaInN and AlInN by Bryden and Kistenmacher [296] is available but predates the bandgap reconsideration of InN; the growth and mobility of p-GaInN is discussed by Yamasaki *et al.* [344].

1.5.3
InAlN Alloy

$In_{1-x}Al_xN$ is an important compound that can provide a lattice-matched barrier to GaN, low fraction AlGaN, and InGaN, and consequently lattice-matched AlInN/AlGaN or AlInN/InGaN heterostructures. Although there was some discrepancy as to which composition really lattice-matched GaN, continued improvement in layer quality and persistence narrowed the In composition for matching. Compositions $In_{0.29}Al_{0.71}N$ and $In_{0.17}Al_{0.83}N$ have been reported as matching, but the value around the latter composition is gaining more acceptance [397]. The growth and electrical properties of this semiconductor have not yet been as extensively studied compared to the other two ternaries, particularly AlGaN, as the growth of this ternary is also challenging because of diverse thermal stability, lattice constant, and cohesive energy of AlN and InN. Moreover, thermal instability resulting from, for example, the spinodal phase separation phenomenon, which is more of an issue in $Al_{1-x}In_xN$ than in $In_yGa_{1-y}N$ [398], must be considered. Despite the above-mentioned difficulties, lattice matching and the lack of crack formation when AlGaN is replaced with InAlN in distributed Bragg reflectors (DBRs) and other structures requiring relatively thicker layers are more than enough to pursue this material. In fact, light emitters, field effect transistors, and DBRs, as mentioned, using InAlN barriers as opposed to AlGaN are gaining considerable momentum.

As in the case of AlGaN and InGaN, the calculated lattice parameter of this alloy follows Vegard's law [347] (also reviewed in Ref. [17]) as

$$a_{Al_xIn_{1-x}N} = 3.58480 - 4753x \text{ Å} \quad \text{and} \quad c_{Al_xIn_{1-x}N} = 5.8002 - 0.8063x \text{ Å}. \tag{1.29}$$

By utilizing various tools such as HRXRD, the experimental data for various AlInN layers support the applicability of Vegard's law in that the experimental data $a_{Al_xIn_{1-x}N} = (3.560 \pm 0.019) - (0.449 \pm 0.019)x$ Å and $c = (5.713 \pm 0.014) - (0.745 \pm 0.024)x$ Å are within about 2% of that predicted by linear interpolation, the Vegard' law. As in the case of AlGaN and InGaN, the bond lengths exhibit a

nonlinear behavior, deviating from the virtual crystal approximation. Essentially, the nearest neighbor bond lengths are not as dependent on composition as might be expected from the virtual crystal approximation.

Early experimental results [288] for the bandgap of $In_{0.29}Al_{0.71}N$, which was thought lattice matched to GaN, indicate that this alloy has an energy gap of 3.34 eV at low temperatures (the room-temperature value is actually closer to 4.5 eV) that is even below that for GaN. The estimations by Wright and Nelson [399] that followed pointed to a bandgap of about 5 eV for the zinc blende variety. The accompanying bowing parameter reported by Wright and Nelson is 2.53 eV at the time when the larger InN bandgap was accepted. Naturally, when the bandgap is in question the bowing parameter is even more in question. As in the case of AlGaN and InGaN, the compositional dependence of the bandgap of AlInN can be expressed with the following empirical expression using a bowing parameter, b_{AlInN}, as

$$\begin{aligned} E^{\mathrm{g}}_{\mathrm{Al}_x\mathrm{InN}} &= xE^{\mathrm{g}}_{\mathrm{AlN}} + (1-x)E^{\mathrm{g}}_{\mathrm{InN}} - b_{\mathrm{AlInN}}x(1-x) \\ &= 6.1x + 0.7(1-x) - b_{\mathrm{AlInN}}x(1-x)\ \mathrm{eV}. \end{aligned} \tag{1.30}$$

In addition to the aforementioned calculations, experimental data for the bowing parameter, b, exist. Using a bandgap of 6.2 eV for AlN (the new figure is closer to 6 eV), the values that have been reported encompass $b = 3.1$ eV deduced by fitting the bandgap of this alloy determined by PL [400], $b = 2.384$ eV by absorption measurements but by using 2.0 eV for the bandgap of InN and 5.9 eV for AlN [401], and $b = 5.4$ eV in a review where 1.95 eV was used for InN bandgap [17]. Scaling the bandgap of AlN to about 6.0 eV would reduce the bowing parameter a little. Despite the scattered data, reasonably useful bandgap variation of AlInN with composition can be obtained as shown in Figure 1.40.

Kim *et al.* [404] deposited thin AlInN films with X-ray rocking curve FWHM values between 10 and 20 arcmin. They observed an increase of In content in AlInN of up to 8% by lowering the substrate temperature to 600 °C. A further reduction of substrate temperature during OMVPE is not useful because of the needed efficient pyrolysis of ammonia. Yamaguchi *et al.* [405] also reported on OMVPE growth of AlInN on GaN templates that were in turn deposited on low-temperature AlN nucleation layers on *c*-plane sapphire. In macroscopic sense, the alloys grown were not phase separated and the bandgap variation followed the compositional variations in the InN composition range of 19–44%. From the square of the absorption coefficient versus $E–E_g$, the bandgap of the alloy was determined.

Starosta [406] and later Kubota *et al.* [407] grew InAlN alloy by radio frequency (RF) sputtering. Kistenmacher *et al.* [408], however, used the RF magnetron sputtering (RF MS) from a composite metal target to grow InAlN at 300 °C. It was observed that the energy bandgap E of this semiconductor varies between 2.0 eV (this is supposed to represent the InN binary end point, which assumes the old and incorrect value) and 6.20 eV (this too represents the old value for the bandgap of AlN with the new figure being approximately 6 eV) for x between 0 and 1 [407]. The carrier concentration and the mobility of $In_{1-x}Al_xN$ for $x = 0.04$ were $2\times10^{20}\ \mathrm{cm}^{-3}$ and $35\ \mathrm{cm}^2\ \mathrm{V}^{-1}\mathrm{s}^{-1}$, respectively, and for $x = 0.25$ were $8\times10^{19}\ \mathrm{cm}^{-3}$ and $2\ \mathrm{cm}^2\mathrm{V}^{-1}\mathrm{s}^{-1}$,

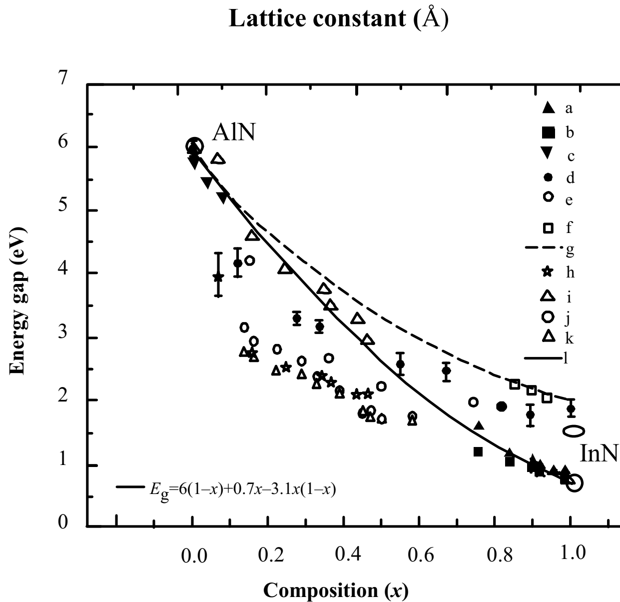

Figure 1.40 Dependence of bandgap of the InAlN alloy on composition. Unless otherwise stated, the measurement temperature is room temperature. The solid line between the 0.8 eV gap of InN and 6 eV of AlN is deemed as being reasonably accurate. (a) Absorption; (b) RT PL; (c) RT absorption [404]; (d) Ref. [401]; (e) absorption, poly [416]; (f) absorption [402]; (g) a theory [403]; (h) RT PL and CL [400]; (i) 8 K optical reflection [400]; (j) RT absorption [405]; (k) RT PL [405]; (l) fit to $E_g = 6(1-x) + 0.7x - 3.1x(1-x)$. In part courtesy of Wladek Walukiewicz.

respectively [296]. Thus, the mobility decreases substantially with an increase in the Al mole fraction because the structure of the InAlN approaches the structure of the insulating AlN.

1.5.4 InAlGaN Quaternary Alloy

By alloying InN together with GaN and AlN, the bandgap of the resulting alloy(s) can be increased from 1.9 eV (or near 0.7 eV if we use the updated InN bandgap) to a value of 6.2 eV (or 6 eV if we use the updated value), which is critical for making high-efficiency visible light sources and detectors. In addition, the bandgap of this quaternary can be changed while keeping the lattice constant matched to GaN [409,410]. In quaternary alloys of nitrides, the N atoms constitute anion sublattice, whereas group III elements (In, Ga, Al) constitute the cation sublattice. Use of this quaternary material allows almost independent control of the bandgap and thus the band offset in AlInGaN-based heterostructures. However, among other difficulties brought about by the four-component system, the optimal growth temperature is important to optimize and control, as aluminum-based compounds generally require higher growth temperatures and In-based ones require lower

temperatures. Higher temperatures are also desirable for reducing the O incorporation in the growing film as oxides of Ga and In desorb from the surface. The growth temperature will therefore govern the limits of In and Al incorporation into the AlGaInN quaternary alloy [409]. The quaternary alloy $(Ga_{1-x}Al_x)In_{1-y}N$ is expected to exist in the entire composition range $0 < x < 1$ and $0 < y < 1$. Unfortunately, as in the case of the InGaN alloy, incorporation of indium in these quaternary alloys is not easy. To prevent InN dissociation, InGaN crystals were originally grown at low temperatures (about 500 °C) [411], which also applies to InGaAlN. The use of a high nitrogen flux rate allowed the high-temperature (800 °C) growth of high-quality InGaN and InGaAlN films on (0 0 0 1) sapphire substrates. Note that the incorporation of indium into InGaN film is strongly dependent on the flow rate, N/III ratio, and growth temperature in an OMVPE environment. The incorporation efficiency of indium decreases with increasing growth temperatures. Observations made in the case of InGaN should be applicable to In incorporation in quaternary nitrides.

Ryu *et al.* [412] reported on the optical emission in this quaternary system and AlInGaN/AlInGaN multiple quantum wells grown by pulsed metalorganic chemical vapor deposition. Strong blue shift with excitation intensity was observed in both the quaternary layers and quantum wells that was attributed to localization. This would imply the inhomogeneous nature of the structures and/or presence of band tail states indicative of early stages of material development and/or serious technological problems involved.

The relationships between composition and bandgap (or lattice constant) can be predicted by the equation below, which was originally developed for the InGaAsP system [413].

$$Q(x,y,z) = \frac{xyT_{12}((1-x+y)/2) + yzT_{23}((1-y+z)/2) + zxT_{31}((1-z+x)/2)}{xy+yz+zx},$$

$$T_{ij}(\alpha) = \alpha B_j + (1-\alpha)B_i + \alpha(1-\alpha)b_{ij}.$$

The parameters x, y, and z represent the composition of GaN, InN, and AlN. If GaN, InN, and AlN are represented by 1, 2, and 3, T_{12} would represent Ga_xIn_yN. Further, the term T_{12} can be expressed as $T_{12}(\alpha) = \alpha B_2 + (1-\alpha)B_1 + \alpha(1-\alpha)b_{12}$, where b_{12} is the bowing parameter for the Ga_xIn_yN alloy and $\alpha = (1-x+y)/2$ or $(1-x+y)/2$ or $(1-z+x)/2$ is the effective molar fraction for GaInN, InAlN, and AlGaN, respectively, B_2 the bandgap of InN, and B_1 is the bandgap of GaN. Similar expressions can be constructed for T_{23} and T_{31} by appropriate permutations. An alternative approach is discussed in conjunction with Equation 1.31.

The results of these calculations for the bandgap and lattice constant dependence on composition are shown in the three-dimensional diagrams of Figures 1.41–1.43.

An empirical expression similar to that used for the ternaries can also be constructed for the quaternary as

$$\begin{aligned} E^{g}_{Al_xIn_yGa_{1-x-y}N} &= xE^{g}_{AlN} + yE^{g}_{InN} + (1-x-y)E^{g}_{GaN} \\ &\quad - b_{AlGaN}x(1-x) - b_{InGaN}y(1-y), \end{aligned} \tag{1.31}$$

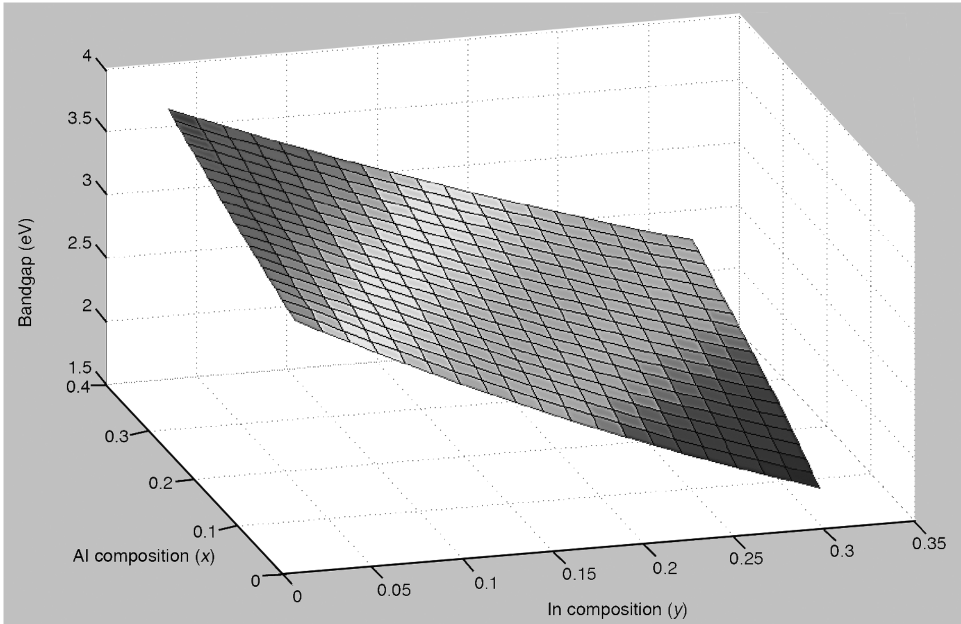

Figure 1.41 Bandgap versus composition for quaternary $Al_xIn_yGa_{1-x-y}N$ (assumed InN bandgap = 0.8 eV). (Please find a color version of this figure on the color tables.)

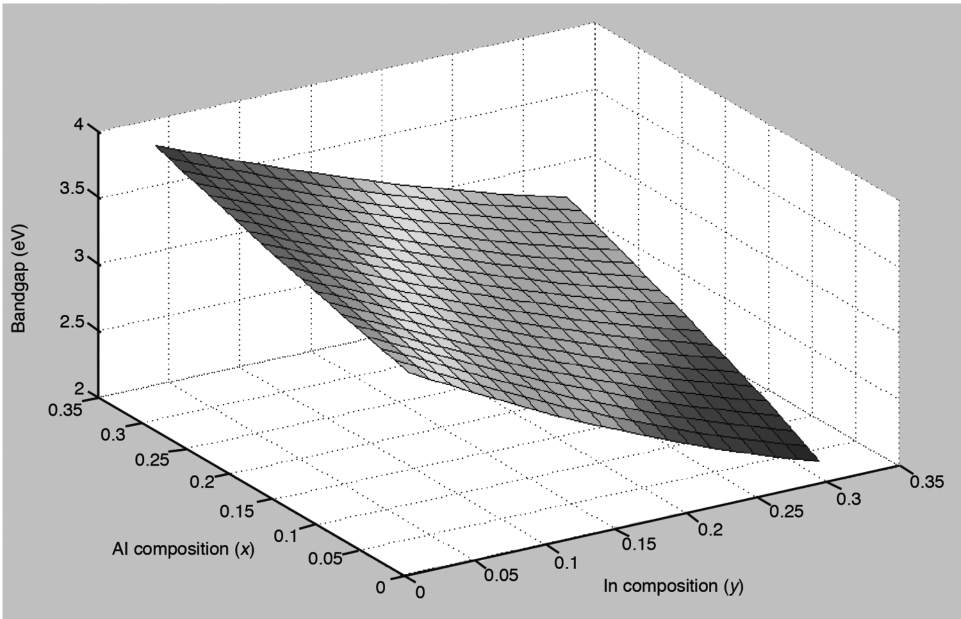

Figure 1.42 Bandgap versus composition for quaternary $Al_xIn_yGa_{1-x-y}N$ (assumed InN bandgap = 1.9 eV). (Please find a color version of this figure on the color tables.)

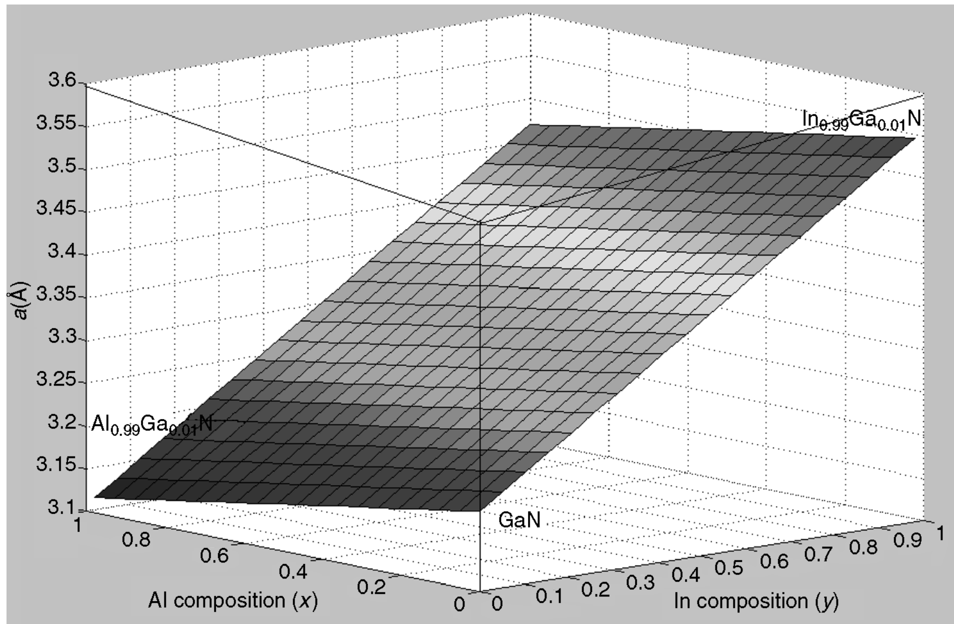

Figure 1.43 Lattice constant a versus composition for quaternary $Al_xIn_yGa_{1-x-y}N$.

where the first three parameters on the right-hand side of the equation are contributions by the binaries to the extent of their presence in the lattice, the third term represents the bowing contribution related to Al, and the last term depicts the bowing contribution due to In. The bowing parameters, b_{AlGaN} and b_{InGaN}, indicated in Equation 1.31 are the same as those discussed in conjunction with InGaN and AlInN. As such, the values are the same. The parameters x, y, and z represent the molar fraction of binaries in the quaternary.

After discussing all three ternary alloys of the nitride semiconductor family, the bandgap (both in terms of energy and also corresponding air wavelength) versus the lattice parameter is shown in Figure 1.44 for convenience.

The discussion of alloys individually up to this point paves the way to a collective discussion of alloys in terms of structural parameters for a rapid observation of trends. This discussion would be of special value particularly for the least discussed of alloys, InAlN. Let us first discuss the structural properties such as the lattice constants and bond lengths, and angles of nitride semiconductor alloys, following the discussion in Sections 1.5.1–1.5.3 and that surrounding Figure 1.8, Equation 1.3, and Table 1.2. Following Ref. [17], the lattice parameter calculated using Equation 1.25 (for AlGaN), Equation 1.27 (for InGaN), and Equation 1.29 (for InAlN) can be used to calculate the lattice constants for the three ternaries for all compositions and compared with experiments for AlGaN [414], InGaN [415], and InAlN [416], as shown in Figure 1.45.

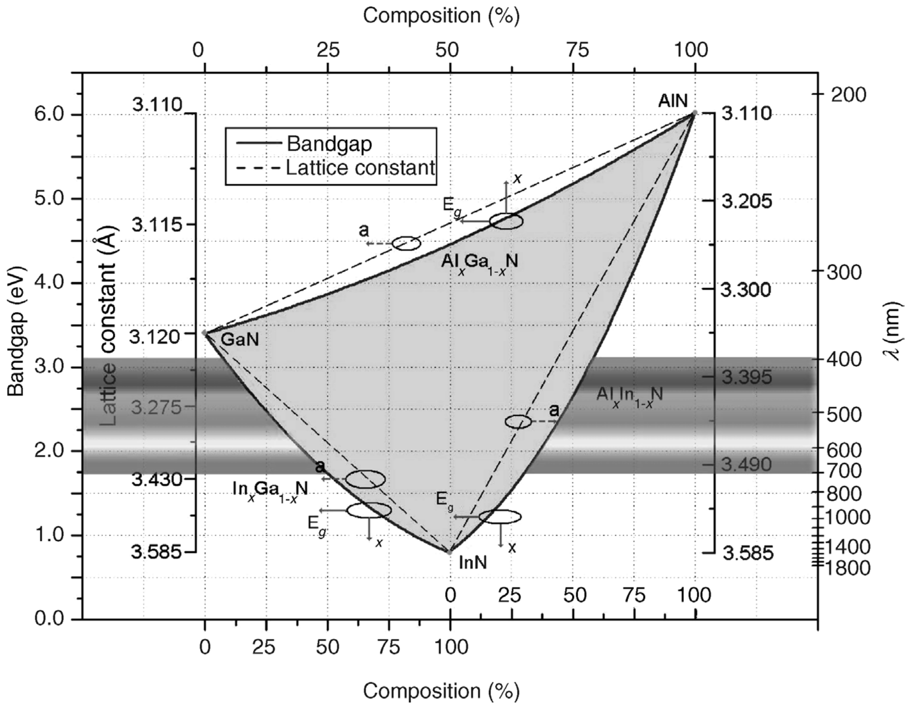

Figure 1.44 The bandgap versus the lattice parameter for AlGaN, InGaN, and InAlN using bowing parameters in the same order, 1, 1.43, and 3.1 eV, and bandgap values of 6 eV for AlN, 3.4 eV for GaN, and 0.8 eV for InN. The lattice constants used for the binary AlN, GaN, and InN are 3.11, 3.199, and 3.585 Å, respectively.

Following the case for the binaries tabulated in Table 1.2 and discussed from a theoretical point of view in Refs [347,417], and the experimental points of view in Refs [414] (for AlGaN), [415] (for InGaN), and [416] (for $Al_xIn_{1-x}N$), the cell parameter, u, has been calculated for randomly distributed $A_{0.5}B_{0.5}N$ (here A and B represent the metal components forming the alloy) alloys by the theoretical approach of Ref. [418], the pertinent parts of which are succinctly discussed in Section 1.1. The internal cell parameter can be approximately expressed by the quadratic equation

$$u_{A_xB_{1-x}N} = xu_{AN} + (1-x)u_{BN} - b_{AB}x(1-x), \qquad (1.32)$$

where b_{AB} is the bowing parameter defined as

$$b_{AB} = 2Y_{AN} + 2Y_{BN} - 4Y_{A_{0.5}B_{0.5}N}. \qquad (1.33)$$

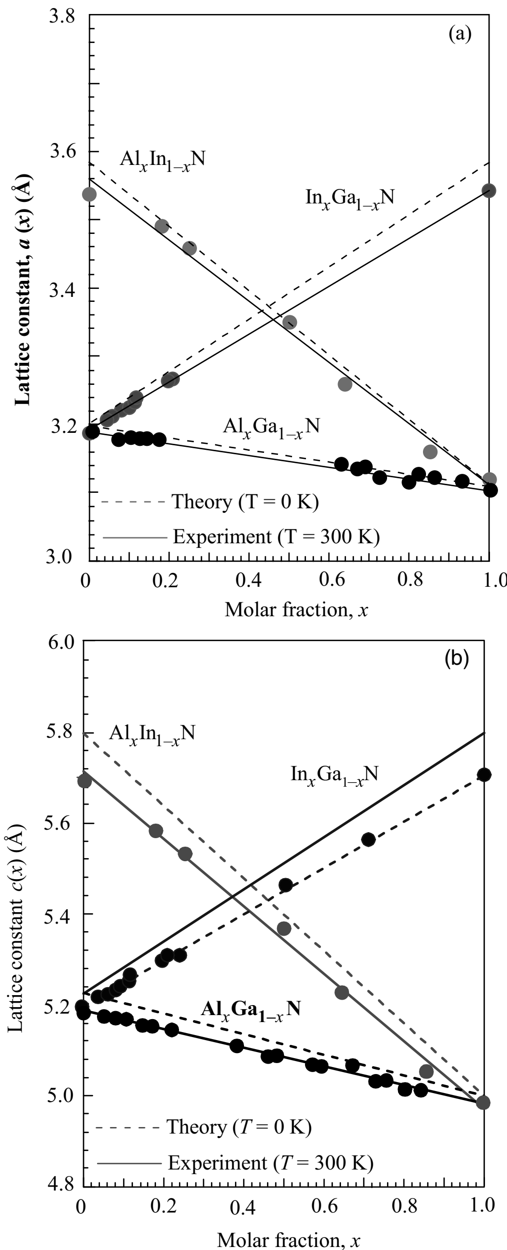

Figure 1.45 (a) The $a(x)$ lattice parameter and (b) the $c(x)$ lattice parameter for random ternary alloys of $Al_xGa_{1-x}N$, $In_xGa_{1-x}N$, and $Al_xIn_{1-x}N$ as measured by HRXRD at room temperature (solid lines) and the calculated values using Equation 1.25 (for AlGaN) and Equation 1.27 (for InGaN) for $T = 0$ K (dashed lines). The agreement between calculations and measured lattice constants is better than 2% over the entire range of compositions, compiled in Ref. [17] utilizing Refs [414,415]. Courtesy of O. Ambacher.

The internal cell parameters for each of the three alloys then are

$$\begin{aligned} u_{\mathrm{Al}_x\mathrm{Ga}_{1-x}\mathrm{N}} &= 0.3819x + 0.3772(1-x) - 0.0032x(1-x), \\ u_{\mathrm{In}_x\mathrm{Ga}_{1-x}\mathrm{N}} &= 0.3793x + 0.3772(1-x) - 0.0057x(1-x), \\ u_{\mathrm{Al}_x\mathrm{In}_{1-x}\mathrm{N}} &= 0.3819x + 0.3793(1-x) - 0.0086x(1-x). \end{aligned} \tag{1.34}$$

The structural and other polarization related parameters of ternaries do not follow a linear relationship of the composition, as discussed in detail in Section 2.7. The nonlinearity in question for an alloy, $A_xB_{1-x}N$, where A and B represent the metal components, is approximated by quadratic equations of the form [418]

$$Y_{\mathrm{A}_x\mathrm{B}_{1-x}\mathrm{N}} = xY_{\mathrm{AN}} + (1-x)Y_{\mathrm{BN}} - b_{\mathrm{AB}}x(1-x), \tag{1.35}$$

where Y represents any parameter, namely the lattice constant, the u parameter or polarization, and the bowing parameter is defined in Equation 1.33.

As in the case of binaries discussed in Section 1.1, the cell parameter, u, and the c/a ratio do not follow the ideal crystal values for the three ternaries of nitride semiconductors. They are shown for the three ternaries for varying composition in Figure 1.46. Similar to the binaries, tabulated in Table 1.2 in conjunction with Figure 1.8, the aforementioned two parameters, the nearest and the second neighbor bond lengths, as well as the bond angles have been calculated for the three ternaries and those associated with 50% alloys are tabulated in Table 1.34.

As displayed in Figure 1.46, the cell internal parameter increases as one goes from GaN to InN and, more significantly, to AlN. The nonlinear dependencies on the alloy composition are described by a bowing parameter, b_{AB}, whose values are 0.0032, 0.0057, and 0.0086 for $Al_xGa_{1-x}N$, $In_xGa_{1-x}N$, and $Al_xIn_{1-x}N$, respectively. The bowing parameter increases from $Al_xGa_{1-x}N$ to $In_xGa_{1-x}N$, and continues on to $Al_xIn_{1-x}N$. It is worth noting that the bowing parameter is negative for all the three ternaries, the average cell internal parameter of the same alloys is always above the ideal value of 0.375. If the lattice constants scale linearly with the alloy composition but the internal parameter does not, the bond angles and/or the bond lengths of the real and the virtual crystal must depend nonlinearly on the alloy composition. The average nearest neighbor bond lengths (b and b_1, see Figure 1.8 for a graphical description) and bond angles (see Figure 1.8 for a graphical description) calculated by using Equations 1.2–1.4 are shown in Figure 1.47a and b and listed in Tables 1.2 and 1.34. The average cation–anion distances to the nearest and second nearest neighbors scale nearly linearly with alloy composition for $Al_xGa_{1-x}N$, $In_xGa_{1-x}N$, and $Al_xIn_{1-x}N$. The average bond length along the c-axis is 0.7–0.9% longer than the nearest neighbor bonds in the direction of the basal plane (Figure 1.47a).

1.5.5 Dilute GaAs(N)

When small amounts of N and As are incorporated into GaAs and GaN lattices, respectively, a large negative bandgap bowing parameter results. Consequently, with

very small amounts of N in the GaAs lattice, its bandgap can be made very small, to a point where 1.3 μm lasers and 1.5 μm lasers if In and Sb are also added to the lattice can all be built with GaAs technology. Anomalously large bandgap bowing parameters exhibited by GaAsN and GaNAs are caused by large chemical and size

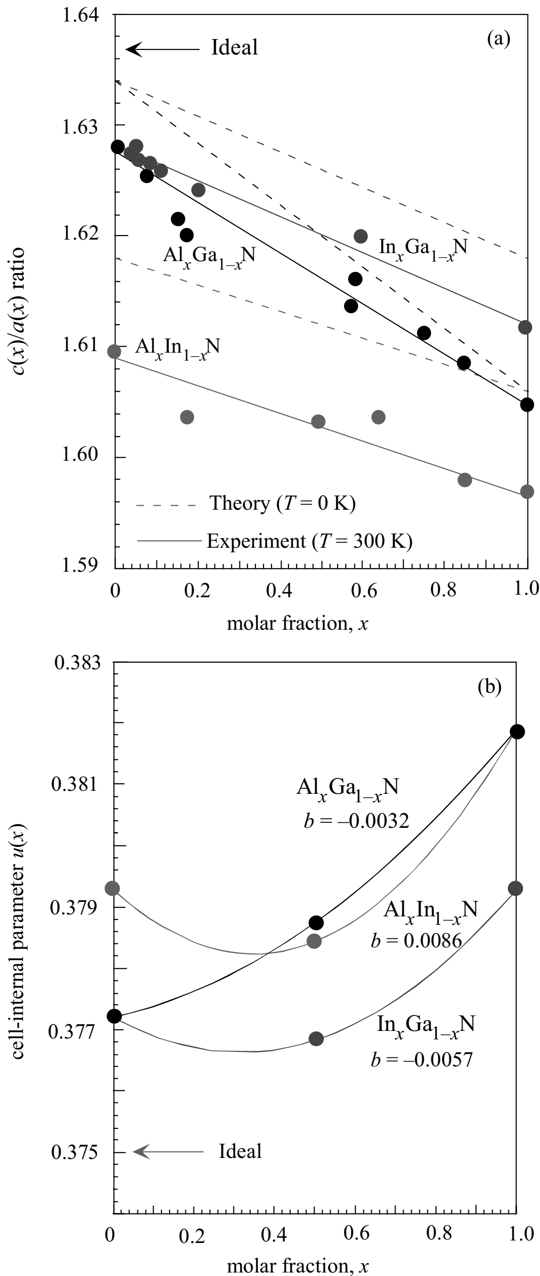

Table 1.34 Calculated cell internal parameter, *a* lattice parameter, *c*/*a* ratio, cation–anion distance between the nearest and second nearest neighbors, and bond angles (given in degrees) for the three ternary random alloys in the virtual crystal limit with a composition of 50%.

	$Al_{0.5}Ga_{0.5}N$	$In_{0.5}Ga_{0.5}N$	$In_{0.5}Al_{0.5}N$
u	0.379	0.377	0.378
a (Å)	3.154	3.392	3.347
c/a	1.620	1.625	1.612
b (Å)	1.935	2.078	2.042
b_1 (Å)	1.924	2.073	2.041
b_1' (Å)	3.175	3.436	3.354
b_2' (Å)	3.701	3.977	3.921
b_3' (Å)	3.694	3.975	3.920
α	108.80	109.13	108.76
β	110.14	109.81	110.18

The distance is in Å and the angles are in degrees [17].

differences between As and N [419–422]. Dependence of the bandgap energy in GaAsN and InPN on nitrogen content is shown in Figure 1.48. To a first extent, the dashed lines originating from both GaN end (in which case small amounts of As are added to GaN) and GaAs end (in which case small amounts of N are added to GaAs) represent the bandgap dependence of GaNAs. However, one must keep in mind that for both GaAsN and InPN the simple treatment behind the aforementioned statement fails and that the arrows shown in the figure indicate the boundaries of the regions where the gap dependence on composition may be predicted with any accuracy. Also shown is the bandgap variation with composition for other commonly used ternaries. The thicker vertical line through GaAs represents the bandgap attainable with GaInAsN, at least in theory, while maintaining lattice matching to GaAs. The decrease in the lattice constant caused by N can be compensated with In added to the lattice. The potential of covering a large range of bandgap energies on GaAs substrates has attracted a great deal of interest in this material system. In fact, the first laser containing N was an InGaAs(N) active layer one. Owing in part to

Figure 1.46 (a) The *c*/*a* ratio for the three random ternary alloys determined by HRXRD at room temperature (solid lines) and calculated using Equation 1.24 for $T = 0$ K (dashed lines). The measured and calculated data confirm that the *c*/*a* ratios of Wz InGaN, AlGaN, and AlInN crystals are always less than the value of 1.633 for ideal hexagonal crystal. (b) The cell internal parameter, *u*, for three random AlGaN, InGaN, and AlInN alloys calculated using the quadratic Equation 1.35. The nonlinearity of the internal cell internal parameter in its compositional dependence can be described by a negative bowing parameter *b*. This bowing parameter is 0.0032, 0.0057, and 0.0086 for $Al_xGa_{1-x}N$, $In_xGa_{1-x}N$, and $Al_xIn_{1-x}N$, respectively, as indicated in the figure as well. The *u* parameter of the ternaries is always larger than 0.375 that is the value for an ideal hexagonal crystal [17]. Courtesy of O. Ambacher.

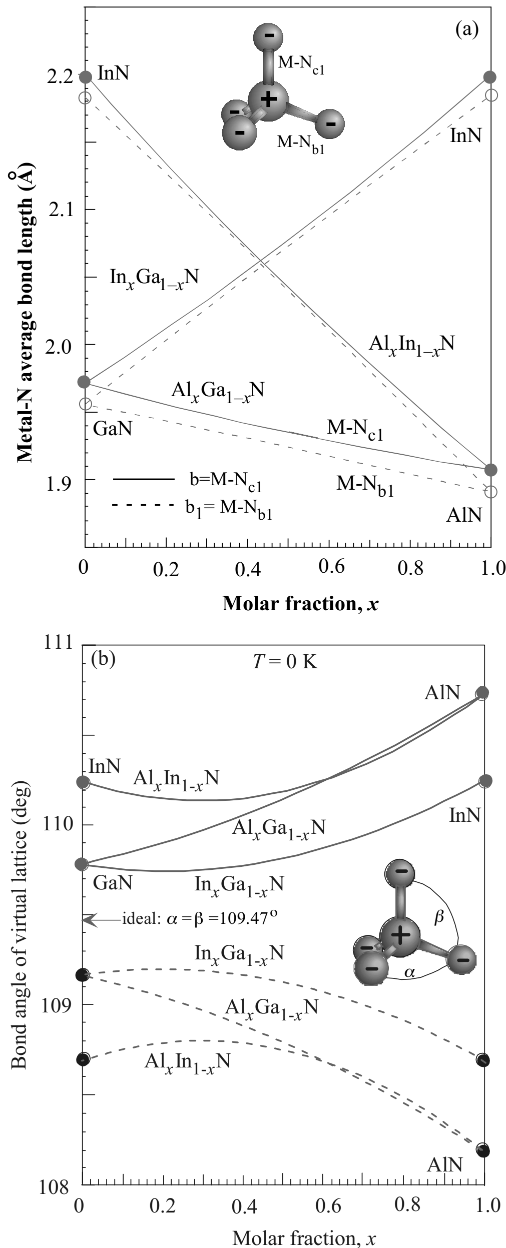

Figure 1.47 (a) The compositional dependence of the average nearest neighbor bond lengths, b and b_1 (see Figure 1.8 for a graphical description) in the virtual crystal limit for the metal–nitrogen bonds along the c-axis (solid line) and off c-axis (dashed line). (b) The compositional dependence of the average bond angles α (dashed lines) and β (solid lines) of random $Al_xGa_{1-x}N$, $In_xGa_{1-x}N$, and $Al_xIn_{1-x}N$ alloys (see Figure 1.8 for a graphical description). Clearly, the average bond angles deviate noticeably from the ideal hexagonal crystal for which $\alpha = \beta = 109.47$. Moreover, the deviation increases from GaN to InN and continues onto AlN in a nonlinear fashion [17]. Courtesy of O. Ambacher.

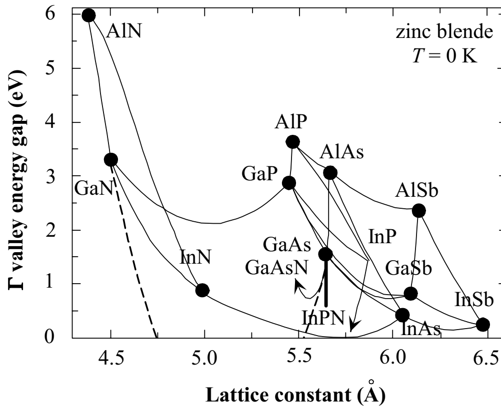

Figure 1.48 Direct Γ valley energy gap as a function of lattice constant for the zinc blende form of 12 III–V binary compound semiconductors (filled circles) and some of their random ternary alloys (lines connecting the solid circles) at zero temperature. The energy gaps for certain ternaries such as AlAsP, InAsN, GaAsN, InPN, and GaPN are extended into regions where no experimental data have been reported. For GaAsN and InPN, the arrows indicate the boundaries of the regions where the gap dependence on composition may be predicted with any accuracy, patterned after Ref. [423] with necessary changes, particularly the one reflecting the small bandgap of InN.

extreme nonequilibrium conditions employed for growth, MBE is the dominant growth approach for dilute arsenides with nitrogen. The critical issues are compositional control, incorporation of more than a small percentage of N, doping inefficiency, and layer quality. The situation is exacerbated on all fronts when the N concentration is increased for achieving 1.5 μm wavelength of emission. Postgrowth annealing is often employed to improve the crystal quality and/or to increase Si dopant incorporation, however, at the expense of blue shift in the bandgap. While GaAsN is chosen here for the present discussion, there are many other dilute nitride semiconductors as discussed in Section 2.11 in conjunction with band parameters.

As alluded to earlier, the chemical and size differences between the N and As atoms are the challenges facing experimentalists. In addition, the generation of atomic nitrogen, although not that different from the technology required for hexagonal GaN growth [424], deserves some attention. While basic mismatch between N and As can be dealt with by growing the layers under nonequilibrium conditions, the issue of atomic nitrogen can be handled by compact RF sources that have seen a good degree of improvement lately. By adjusting the RF power and pressure in the cell, one can tailor the source to produce mostly the atomic species by optimizing the emission at 745 nm of wavelength. Note that the substrate and most of the structure are zinc blende and, consequently, the dilute material assimilates and assumes the same crystalline structure. The desired nitrogen concentrations are in the range of 1–10% for red shifting the transitions out to as long as 1.55 μm. Larger growth rates lead to a reduced incorporation of N in the lattice. Similarly, higher growth temperatures lead to the same. Consequently, when 1.55 μm wavelength material is desired, lower

growth rates must be employed as well as lower growth temperatures. At substrate temperatures of 500 °C or below, if very large As overpressure is employed, incorporation of N is limited because the flux of atomic nitrogen is small. However, atomic nitrogen is very reactive and, therefore, compositional control should be much better as compared to quaternaries relying on P and As (InGaAsP).

As expected, owing to dissimilarities of N and As, the luminescence properties of GaInNAs degrade rapidly with increasing nitrogen concentration. Employing remedies such as postgrowth annealing enhances the luminescence efficiency of GaInNAs. However, this enhancement is accompanied by a blue shift in the transition in bulk and quantum well materials. Nitrogen and possibly In diffusion out of GaInAsN are responsible for the observed luminescence shift to shorter wavelengths.

For completeness, a one-paragraph discussion of device issues will be made in conjunction with the edge emitting and vertical cavity lasers operating at 1.3 and 1.5 μm portion of the optical spectrum, although other applications such as heterojunction bipolar transistors are possible. Several groups have reported lasers operating at 1.3 μm region [425–442], where the silica-based fiber dispersion is zero, and 1.5 μm region [443–447] (albeit with addition of Sb to the lattice as the quality required for laser operation for InGaAsN layers cannot be obtained), where the loss is low, again for the silica-based fibers. Both are intended for telecommunication purposes. Even 8 W [448] and 12 W [449] CW operation has been reported. High-speed testing of these lasers has also been performed [450] with data transmission rates as high as Gbit s^{-1} having been achieved already [451]. For interconnects and high-speed data links, vertical cavity surface emitting lasers (VCSELs) have received a great deal of attention. Now that dilute nitrides are becoming potential candidates for long-wavelength lasers, efforts are under way to explore VCSELs in this material system as well [452,453].

References

1 Lei, T., Fanciulli, M., Molnar, R.J., Moustakas, T.D., Graham, R.J. and Scanlon, J. (1991) *Applied Physics Letters*, **59**, 944.

2 Paisley, M.J., Sitar, Z., Posthill, J.B. and Davis, R.F. (1989) *Journal of Vacuum Science & Technology*, **7**, 701.

3 Powell, R.C., Lee, N.E., Kim, Y.W. and Greene, J.E. (1993) *Journal of Applied Physics*, **73**, 189.

4 Mizita, M., Fujieda, S., Matsumoto, Y. and Kawamura, T. (1986) *Japanese Journal of Applied Physics*, **25**, L945.

5 Xia, Q., Xia, H. and Ruoff, A.L. (1993) *Journal of Applied Physics*, **73**, 8198.

6 Perlin, P., Jauberthie-Carillon, C., Itie, J.P., San Miguel, A., Grzegory, I. and Polian, A. (1992) *Physical Review B: Condensed Matter*, **45**, 83.

7 Ueno, M., Yoshida, M., Onodera, A., Shimommura, O. and Takemura, K. (1994) *Physical Review B: Condensed Matter*, **49**, 14.

8 Pirouz, P. and Yang, J.W. (1993) *Ultramicroscopy*, **51**, 189.

9 Ruterana, P., Sánchez, A.M. and Nouet, G. (2003) Extended defects in wurtzite GaN layers: atomic structure, formation and interaction mechanisms, in *Nitride Semiconductors – Handbook on Materials*

and Devices (eds P. Ruterana, M. Albrecht and J. Neugebauer), Wiley-VCH Verlag GmbH, Weinheim, Germany.

10 Harris, W.A. (1980) *Electronic Structure and Properties of Solids*, Dover, NY, pp. 174–179.

11 Yeh, C.-Y., Lu, Z.W., Froyen, S. and Zunger, A. (1992) *Physical Review B: Condensed Matter*, **46**, 10086.

12 Bernardini, F., Fiorentini, V. and Vanderbilt, D. (2001) Accurate calculation of polarization-related quantities in semiconductors. *Physical Review B: Condensed Matter*, **63**, 193–201.

13 Bechstedt, F., Großner, U. and Furthmüller, J. (2000) *Physical Review B: Condensed Matter*, **62**, 8003.

14 Wei, S.-H. and Zunger, A. (1996) *Applied Physics Letters*, **69**, 2719.

15 Leszczynski, M., Teisseyre, H., Suski, T., Grzegory, I., Bockowski, M., Jun, J., Porowski, S., Pakula, K., Baranowski, J.M., Foxon, C.T. and Cheng, T.S. (1996) Lattice parameters of gallium nitride. *Applied Physics Letters*, **69**, 73.

16 Leszczynski, M. (1999) Common crystal structure of the group III-nitrides, in *Properties, Processing and Applications of Gallium Nitride and Related Semiconductors* (eds J.H. Edgar, S. Strite, I. Akasaki, H. Amano and C. Wetzel), EMIS Data Review Series, No. 23, INSPEC, The Institution of Electrical Engineers, Stevenage, UK, pp. 3–5.

17 Ambacher, O., Majewski, J., Miskys, C., Link, A., Hermann, M., Eickhoff, M., Stutzmann, M., Bernardini, F., Fiorentini, V., Tilak, V., Schaff, B. and Eastman, L.F. (2002) Pyroelectric properties of Al(In)GaN/GaN hetero- and quantum well structures. *Journal of Physics: Condensed Matter*, **14**, 3399–3434.

18 Leszczynski, M., Suski, T., Perlin, P., Teisseyre, H., Grzegory, I., Bockowski, M., Jun, J., Porowski, S., Pakula, K., Baranowski, J.M., Foxon, C.T. and Cheng, T.S. (1996) *Applied Physics Letters*, **69**, 73.

19 Jeffery, G.A., Parry, G.S. and Mozzi, R.L. (1956) *Journal of Chemical Physics*, **25**, 1024.

20 Schulz, H. and Theimann, K.H. (1977) *Solid State Communications*, **23**, 815.

21 Tanaka, M., Nakahata, S., Sogabe, K., Nakata, H. and Tabioka, M. (1997) *Japanese Journal of Applied Physics*, **36**, L1062.

22 Angerer, H., Brunner, D., Freudenberg, F., Ambacher, O., Stutzmann, M., Höpler, R., Metzger, T., Born, E., Dollinger, G., Bergmaier, A., Karsch, S. and Körner, H.-J. (1997) *Applied Physics Letters*, **71**, 1504.

23 Domagala, J., Leszczynski, M., Prystawko, P., Suski, T., Langer, R., Barski, A. and Bremser, M. (1999) *Journal of Alloys and Compounds*, **286**, 284.

24 Kim, K., Lambrecht, W.R.L. and Segall, B. (1996) *Physical Review B: Condensed Matter*, **53**, 16310.

25 Wright, A.F. and Nelson, J.S. (1995) *Physical Review B: Condensed Matter*, **51**, 7866.

26 Detchprohm, T., Hiramatsu, K., Itoh, K. and Akasaki, I. (1992) *Japanese Journal of Applied Physics*, **31**, L1454.

27 Leszczynski, M., Teisseyre, H., Suski, T., Grzegory, I., Bockowski, M., Jun, J., Porowski, S. and Major, J. (1995) *Journal of Physics D: Applied Physics*, **69**, A149.

28 Deguchi, T., Ichiryu, D., Toshikawa, K., Sekiguchi, K., Sota, T., Matsuo, R., Azuhata, T., Yamaguchi, M., Yagi, T., Chichibu, S. and Nakamura, S. (1999) *Journal of Applied Physics*, **86**, 1860.

29 Paszkowicz, W. (1999) *Powder Diffraction*, **14**, 258.

30 Wu, J., Walukiewicz, W., Yu, K.M., Ager, J.W., III, Haller, E.E., Lu, H., Schaff, W.J., Saito, Y. and Nanishi, Y. (2003) *Applied Physics Letters*, **80**, 3967.

31 Phillips, J.C. (1973) *Bonds and Bands in Semiconductors*, Academic Press, New York, p. 31.

32 Xu, Y.-N. and Ching, W.Y. (1993) Electronic, optical, and structural properties of some wurtzite crystals.

Physical Review B: Condensed Matter, **48**, 4335–4350.

33 Morkoç, H., Strite, S., Gao, G.B., Lin, M.E., Sverdlov, B. and Burns, M. (1994) Large-band-gap SiC, III–V nitride, and II–VI ZnSe-based semiconductor device technologies. *Journal of Applied Physics*, **76** (3), 1363–1398.

34 Akasaki, I. and Amano, H. (1994) *Properties of Group III Nitrides* (ed. J.H. Edgar), EMIS Data Review Series, No. 11, INSPEC, The Institution of Electrical Engineers, Stevenage, UK, pp. 30–34.

35 Christensen, N.E. and Gorczyca, I. (1994) Optical and structural properties of III–V nitrides under pressure. *Physical Review B: Condensed Matter*, **50**, 4397–4415.

36 Levinshtein, M., Rumyantsev, S. and Shur, M. (eds) (1996/1999) *Handbook Series on Semiconductor Parameters*, vols 1 and 2, World Scientific, London.

37 Bougrov, V., Levinshtein, M.E., Rumyantsev, S.L. and Zubrilov, A. (2001) *Properties of Advanced Semiconductor Materials GaN, AlN, InN, BN, SiC, SiGe* (eds M.E. Levinshtein, S.L. Rumyantsev and M.S. Shur), John Wiley & Sons, Inc., New York, pp. 1–30.

38 Polian, A., Grimsditch, M. and Grzegory, I. (1996) *Journal of Applied Physics*, **79**, 3343–3344.

39 Kisielowski, C., Krüger, J., Ruvimov, S., Suski, T., Ager, J.W., III, Jones, E., Liliental-Weber, Z., Rubin, M., Weber, E.R., Bremser, M.D. and Davis, R.F. (1996) *Physical Review B: Condensed Matter*, **54**, 17745.

40 Nikolaev, V., Shpeizman, V. and Smirnov, B. (1998) The Second Russian Workshop on GaN, InN, and AIN-Structures and Devices, June 2, St Petersburg Technical University, St Petersburg, Russia.

41 Drory, M.D., Ager, J.W., Suski, T., Grzegory, I. and Porowski, S. (1996) Hardness and fracture toughness of bulk single crystal gallium nitride. *Applied Physics Letters*, **69** (26), 4044–4046.

42 Wright, A.F. (1997) Elastic properties of zinc-blende and wurtzite AlN, GaN, and InN. *Journal of Applied Physics*, **82** (6), 2833–2839.

43 Madelung, O. (ed.) (1991) *Semiconductor: Group IV Elements and III–V Compound, Data in Science and Technology* (series ed. R. Poerschke), Springer, Berlin.

44 Truell, R., Elbaum, C. and Chick, B.B. (1969) *Ultrasonic Methods in Solid State Physics*, Academic Press, New York.

45 Kim, K., Lambrecht, W.R.L. and Segall, B. (1994) *Physical Review B: Condensed Matter*, **50**, 1502.

46 Ueno, M., Yoshida, M., Onodera, A., Shimomura, O. and Takemura, K. (1994) *Physical Review B: Condensed Matter*, **49**, 14.

47 Leszczynski, M., Podlasin, S. and Suski, T. (1993) *Journal of Applied Crystallography*, **32**, 1528.

48 Qian, W., Skowronski, M. and Rohrer, G.R. (1996) Structural defects and their relationship to nucleation of GaN thin films, in III-Nitride, SiC, and Diamond Materials for Electronic Devices, Materials Research Society Symposium Proceedings, vol. 423 (eds D.K. Gaskill, C.D. Brandt and R.J. Nemanich), Pittsburgh, PA, pp. 475–486.

49 Sheleg, A.U. and Savastenko, V.A. (1977) *Vestsi Akademii Nauk, Seria. Fizika i Matematika Nauk*, 126.

50 Porowski, S. (1997) *Materials Science & Engineering B: Solid State Materials for Advanced Technology*, **44**, 407–413.

51 Barin, I., Knacke, O. and Kubaschewski, O. (1977) *Thermochemical Properties of Inorganic Substances*, Springer, Berlin.

52 Fritsch, D., Schmidt, H. and Grundmann, M. (2003) Band-structure pseudopotential calculation of zinc-blende and wurtzite AlN, GaN, and InN. *Physical Review B: Condensed Matter*, **67**, 235205.

53 Chow, T.P. and Ghezzo, M.J. (1996) SiC power devices, in III-Nitride, SiC, and Diamond Materials for Electronic Devices, Materials Research Society Symposium Proceedings, vol. 423 (eds D.K. Gaskill, C.D. Brandt and R.J. Nemanich), Pittsburgh, PA, pp. 69–73.

54 Ejder, E. (1971) *Physica Status Solidi a: Applied Research*, **6**, 445–448.

55 Barker, A.S., Jr and Ilegems, M. (1973) Infrared lattice vibrations and free-electron dispersion in GaN. *Physical Review B: Condensed Matter*, **7**, 743.

56 Manchon, D.D., Jr, Barker, A.S., Jr, Dean, P.J. and Zetterstrom, R.B. (1970) *Solid State Communications*, **8**, 1227.

57 Siegle, H., Kaczmarczyk, G., Filippidis, L., Litvinchuk, L., Hoffmann, A. and Thornsen, C. (1997) Zone-boundary phonons in hexagonal and cubic GaN. *Physical Review B: Condensed Matter*, **55** (11), 7000–7004.

58 Karch, K., Wagner, J.-M. and Bechstedt, F. (1998) *Ab initio* study of structural, dielectric, and dynamical properties of GaN. *Physical Review B: Condensed Matter*, **57**, 7043–7049.

59 Zi, J., Wan, X., Wei, G., Zhang, K. and Xie, X. (1996) *Journal of Physics: Condensed Matter*, **8**, 6323–6328.

60 Lemos, V., Arguello, C.A. and Leite, R.C.C. (1972) *Solid State Communications*, **11**, 1351.

61 Dingle, R. and Ilegems, M. (1971) *Solid State Communications*, **9**, 175.

62 Rheinlander, A. and Neumann, H. (1974) *Physica Status Solidi b: Basic Research*, **64**, K123.

63 Bloom, S., Harbeke, G., Meier, E. and Ortenburger, I.B. (1974) *Physica Status Solidi b: Basic Research*, **66**, 161–168.

64 Pankove, J.I., Bloom, S. and Harbeke, G. (1975) *RCA Review*, **36**, 163.

65 Look, D.C. and Sizelove, J.R. (2001) Predicted mobility in bulk GaN. *Applied Physics Letters*, **79** (8), 1133–1135.

66 Stroscio, M.A. and Dutta, M. (2001) *Phonons in Nanostructures*, Cambridge University Press.

67 Duboz, J.Y. (2002) Hot photoluminescence in GaN: carrier energy relaxation and hot phonon effects. *Journal of Applied Physics*, **92** (8), 4312–4319.

68 Lee, B.C., Kim, K.W., Dutta, M. and Stroscio, M.A. (1997) *Physical Review B: Condensed Matter*, **56**, 997.

69 Ramirez-Flores, G., Navarro-Contreras, H., Lastras-Martinez, A., Powell, R.C. and Greene, J.E. (1994) *Physical Review B: Condensed Matter*, **50**, 8433.

70 Fan, J.W., Li, M.F., Chong, T.C. and Xia, J.B. (1996) Electronic properties of zinc-blende GaN, AlN, and their alloys $Ga_{1-x}Al_xN$. *Journal of Applied Physics*, **79** (1), 188–194.

71 Chang, W.Y. and Harmon, B.N. (1986) *Physical Review B: Condensed Matter*, **34**, 5305.

72 Hejda, B. and Hauptmanova, K. (1969) *Physica Status Solidi*, **36**, K95.

73 Blum, S. (1971) *Journal of Physics and Chemistry of Solids*, **32**, 2027.

74 Jones, D. and Lettington, A.H. (1972) *Solid State Communications*, **11**, 701.

75 Kobayasi, A., Sankey, O.F., Volz, S.M. and Dow, J.D. (1983) *Physical Review B: Condensed Matter*, **28**, 935.

76 Huang, M.Z. and Ching, W.Y. (1985) *Journal of Physics and Chemistry of Solids*, **46**, 977.

77 Slack, G.A. (1973) *Journal of Physics and Chemistry of Solids*, **34**, 321–335.

78 Goldberg, Y. (2001) *Properties of Advanced Semiconductor Materials GaN, AlN, InN, BN, SiC, SiGe* (eds M.E. Levinshtein, S.L. Rumyantsev and M.S. Shur), John Wiley & Sons, Inc., New York, pp. 31–47.

79 Gerlich, D., Dole, S.L. and Slack, G.A. (1986) *Journal of Physics and Chemistry of Solids*, **47**, 437.

80 Thokala, R. and Chaudhuri, J. (1995) *Thin Solid Films*, **266** (2), 189–191.

81 Kawabi, K., Tredgold, R.H. and Inuishi, Y. (1967) *Electrical Engineering in Japan*, **87**, 62.

82 Yonenaga, I., Shima, T. and Sluiter, M.H.F. (2002) *Japanese Journal of Applied Physics*, **41**, 4620.

83 McNeil, E., Grimsditch, M. and French, R.H. (1993) *Journal of the American Ceramic Society*, **76** (5), 1132–1136.

84 Vurgaftman, I. and Meyer, J.R. (2003) Band parameters for nitrogen-containing semiconductors. *Journal of Applied Physics*, **94** (6), 3675–3696.

85 Slack, G.A. and Bartram, S.F. (1975) *Journal of Applied Physics*, **46** (1), 89–89.

86 Touloukian, Y.S., Kirby, R.K., Taylor, R.E. and Lee, T.Y.R. (eds) (1977) *Thermophysical Properties of Matter*, vol. 13, Plenum Press, New York.

87 Meng, W.J. (1994) *Properties of Group III Nitrides* (ed. J.H. Edgar), IEE EMIS Data Review Series, No. 11, INSPEC, The Institution of Electrical Engineers, Stevenage, UK, pp. 22–29.

88 Krukowski, S., Leszczynski, M. and Porowski, S. (1999) Thermal properties of the group III nitrides, in *Properties, Processing and Applications of Gallium Nitride and Related Semiconductors* (eds J.H. Edgar, S. Strite, I. Akasaki, H. Amano and C. Wetzel), EMIS Data Review Series, No. 23, INSPEC, The Institution of Electrical Engineers, Stevenage, UK, pp. 21–28.

89 Sirota, N.N. and Golodushko, V.Z. (1974) Tezisy Dokl., Vses Konf. Khi., Svyazi Poluprovdn. Polumetallakh 5th, p. 98.

90 Slack, G.A., Tanzilli, R.A., Pohl, R.O. and Vandersande, J.W. (1987) *Journal of Physics and Chemistry of Solids*, **48** (7), 641–647.

91 Slack, G., Schowalter, L., Rojo, J., Morelli, D. and Freitas, J. (2002) Proceedings of the International Workshop on Bulk Nitrides, May 2002, Amazonas, Brazil, *Journal of Crystal Growth*, **246** (3–4), 287–298; For an application of the method to synthetic diamond, see Morelli, D.T., Beetz, C.P. and Perry, T.A. (1988) Thermal conductivity of synthetic diamond films. *Journal of Applied Physics*, **64** (6), 3063–3066.

92 MacChesney, J.B., Bridenbaugh, P.M. and O'Connor, P.B. (1970) *Materials Research Bulletin*, **5**, 783.

93 Koshchenko, V.I., Grinberg, Ya.Kh. and Demidienko, A.F. (1984) *Inorganic Materials*, **20** (11), 1550–1553.

94 Ribeiro, C.T.M., Alvarez, F. and Zanatta, A.R. (2002) *Applied Physics Letters*, **81**, 1005.

95 See, for example, Colthup, N.B., Daly, L.H. and Wiberley, S.E. (1990) *Infrared and Raman Spectroscopy*, Academic Press, San Diego, FL.

96 Ren, Z.M., Lu, Y.F., Ni, H.Q., Liew, T.Y.F., Cheong, B.A., Chow, S.K., Ng, M.L. and Wang, J.P. (2000) *Journal of Applied Physics*, **88**, 7346.

97 Chang, W.Y. and Harmon, B.N. (1986) *Physical Review B: Condensed Matter*, **34**, 5305.

98 Hejda, B. and Hauptmanova, K. (1969) *Physica Status Solidi*, **36**, K95.

99 Blum, S. (1971) *Journal of Physics and Chemistry of Solids*, **32**, 2027.

100 Jones, D. and Lettington, A.H. (1972) *Solid State Communications*, **11**, 701.

101 Kobayashi, A., Sankey, O.F., Volz, S.M. and Dow, J.D. (1983) *Physical Review B: Condensed Matter*, **28**, 935.

102 Huang, M.Z. and Ching, W.Y. (1985) *Journal of Physics and Chemistry of Solids*, **46**, 977.

103 Guo, Q. and Yoshida, A. (1994) *Japanese Journal of Applied Physics, Part 1: Regular Papers, Short Notes & Review Papers*, **33** (5A), 2453–2456.

104 Teisseyre, H., Perlin, P., Suski, T., Grzegory, I., Porowski, S., Jun, J., Pietraszko, A. and Moustakas, T.D. (1994) Temperature dependence of the energy gap in GaN bulk single crystals and epitaxial layer. *Journal of Applied Physics*, **76** (4), 2429–2434.

105 Yamashita, H., Fukui, K., Misawa, S. and Yoshida, S. (1979) *Journal of Applied Physics*, **50**, 896.

106 Roskovcova, L. and Pastrnak, J. (1980) *Czechoslovak Journal of Physics B*, **30**, 586.

107 Silveira, E., Freitas, J.A., Jr, Kneissl, M., Treat, D.W., Johnson, N.M., Slack, G.A. and Schowalter, L.J. (2004) Near-bandedge cathodoluminescence of an AlN homoepitaxial film. *Applied Physics Letters*, **84** (18), 3501–3503.

108 Silveira, E., Freitas, J.A., Jr, Glembocki, O.J., Slack, G.A. and Schowalter, L.J. (2005) Excitonic structure of bulk AlN from optical reflectivity and

cathodoluminescence measurements. *Physical Review B: Condensed Matter*, **71**, 041201(R)-1–041201(R)-4.

109 Gorczyca, I. and Christensen, N.E. (1993) *Physica B*, **185**, 410–414.

110 Gorczyca, I., Svane, A. and Christensen, N.E. (1997) *Internet Journal of Nitride Semiconductor Research*, **2**, article 18.

111 Collins, A.T., Lightowlers, E.C. and Dean, P.J. (1967) *Physical Review*, **158** (3), 833–838.

112 Chu, T.L. and Keln, R.W., Jr (1975) *Journal of the Electrochemical Society*, **122**, 995.

113 Moore, W.J., Freitas, J.A., Jr, Holm, R.T., Kovalenkov, O. and Dmitriev, V. (2005) Infrared dielectric function of wurtzite aluminum nitride. *Applied Physics Letters*, **86**, 141912-1–141912-3.

114 Suzuki, M. and Uenoyama, T. (1995) *Physical Review B: Condensed Matter*, **52**, 8132.

115 Kim, K., Lambrecht, W.R.L. and Segall, B. (1997) *Physical Review B: Condensed Matter*, **56**, 7363.

116 Suzuki, M. and Uenoyama, T. (1996) Strain effect on electronic and optical properties of GaN/AlGaN quantum-well lasers. *Journal of Applied Physics*, **80** (12), 6868–6874.

117 Sanjurjo, J.A., Lopez-Cruz, E., Vogi, P. and Cardona, M. (1983) Dependence on volume of the phonon frequencies and the IR effective charges of several III–V semiconductors. *Physical Review B: Condensed Matter*, **28**, 4579.

118 Carlone, C., Lakin, K.M. and Shanks, H.R. (1984) *Journal of Applied Physics*, **55**, 4010.

119 MacMillan, M.F., Devaty, R.P. and Choyke, W.J. (1993) Infrared reflectance of thin aluminum nitride films on various substrates. *Applied Physics Letters*, **62** (7), 750–752.

120 Perlin, P., Polian, A. and Suski, T. (1993) Raman-scattering studies of aluminum nitride at high pressure. *Physical Review B: Condensed Matter*, **47** (5), 2874–2877.

121 Van Camp, P.E., Van Doren, V.E. and Devreese, J.T. (1991) High-pressure properties of wurtzite- and rocksalt-type aluminum nitride. *Physical Review B: Condensed Matter*, **44** (16), 9056–9059.

122 Pearson, W.B. (1967) *A Handbook of Lattice Spacings and Structures of Metals and Alloys*, Pergamon Press, Oxford.

123 Pichugin, I.G. and Tiachala, M. (1978) *Izvestia Akademii Nauk SSSR, Neorganicheskie Materialy*, **14**, 175.

124 Zubrilov, A. (2001) *Properties of Advanced Semiconductor Materials GaN, AlN, InN, BN, SiC, SiGe* (eds M.E. Levinshtein, S.L. Rumyantsev and M.S. Shur), John Wiley & Sons, Inc., New York, pp. 49–66.

125 Edgar, J.H., Wei, C.H., Smith, D.T., Kistenmacher, T.J. and Bryden, W.A. (1997) *Journal of Materials Science*, **8**, 307.

126 Perlin, P., Iota, V., Weinstein, B.A., Wisniewski, P., Suski, T., Eliseev, P.G. and Osinski, M. (1997) Influence of pressure on photoluminescence and electroluminescence in GaN/InGaN/AlGaN quantum wells. *Applied Physics Letters*, **70**, 2993–2995.

127 Krukowski, S., Witek, A., Adamczyk, J., Jun, J., Bockowski, M., Grzegory, I., Lucznik, B., Nowak, G., Wroblewski, M., Presz, A., Gierlotka, S., Stelmach, S., Palosz, B., Porowski, S. and Zinn, P. (1998) Thermal properties of indium nitride. *Journal of Physics and Chemistry of Solids*, **59**, 289–295.

128 Davydov, V.Yu., Emtsev, V.V., Goncharuk, A.N., Smirnov, A.N., Petrikov, V.D., Mamutin, V.V., Vekshin, V.A., Ivanov, S.V., Smirnov, M.B. and Inushima, T. (1999) Experimental and theoretical studies of phonons in hexagonal InN. *Applied Physics Letters*, **75**, 3297–3299.

129 Tansley, T.L. (1994) *Properties of Group III Nitrides* (ed. J.H. Edgar), INSPEC, London, p. 39.

130 Sobolev, V.V. and Zlobina, M.A. (1999) *Semiconductors*, **33**, 395.

131 Tyagai, V.A., Evstigneev, A.M., Krasiko, A.N., Andreeva, A.F. and Malakhov, V.Ya. (1977) *Soviet Physics: Semiconductors*, **11**, 1257–1259; *Fizika i Tekhnika Poluprovodnikov*, 1977, **11**, 2142 (in Russian).

132 Inushima, T., Shiraishi, T. and Davydov, V.Yu. (1999) Phonon structure of InN grown by atomic layer epitaxy. *Solid State Communications*, **110** (9), 491–495.

133 Lambrecht, W.R. and Segall, B. (1993) Anomalous band-gap behavior and phase stability of c-BN-diamond alloys. *Physical Review B: Condensed Matter*, **47**, 9289–9296.

134 Yeo, Y.C., Chong, T.C. and Li, M.F. (1998) Electronic band structures and effective-mass parameters of wurtzite GaN and InN. *Journal of Applied Physics*, **83**, 1429–1436.

135 Pugh, S.K., Dugdale, D.J., Brand, S. and Abram, R.A. (1999) *Semiconductor Science and Technology*, **14**, 23–31.

136 Foley, C.P. and Tansley, T.L. (1986) Pseudopotential band structure of indium nitride. *Physical Review B: Condensed Matter*, **33**, 1430.

137 Yeh, C.-Y., Lu, Z.W., Froyen, S. and Zunger, A. (1992) Zinc-blende-wurtzite polytypism in semiconductors. *Physical Review B: Condensed Matter*, **46**, 10086–10097.

138 Bechstedt, F. and Furthmüller, J. (2002) Do we know the fundamental energy gap of InN? *Journal of Crystal Growth*, **246** (3–4), 315–319.

139 Johnson, W.C., Parson, J.B. and Crew, M.C. (1932) *The Journal of Physical Chemistry*, **36**, 2561.

140 Maruska, H.P. and Tietjen, J.J. (1969) *Applied Physics Letters*, **15**, 327.

141 Pankove, J.I. (1972) *Journal of the Electrochemical Society*, **119**, 1110.

142 Chu, T.L. (1971) *Journal of the Electrochemical Society*, **118**, 1200.

143 Lakshmi, E. (1981) *Thin Solid Films*, **83**, L137.

144 Morimoto, Y. (1974) *Journal of the Electrochemical Society*, **121**, 1383.

145 Shintani, A. and Minagawa, S. (1976) *Journal of the Electrochemical Society*, **123**, 706.

146 Itoh, K., Amano, H., Hiramatsu, K. and Akasaki, I. (1991) *Japanese Journal of Applied Physics*, **30**, 1604.

147 Ito, K., Hiramatsu, K., Amano, H. and Akasaki, I. (1990) *Journal of Crystal Growth*, **104**, 533.

148 Visconti, P., Reshchikov, M.A., Jones, K.M., Wang, D.F., Cingolani, R., Morkoç, H., Molnar, R.J. and Smith, D.J. (2001) Highly selective photoelectro-chemical etching of nitride materials for defect investigation and device fabrication. *Journal of Vacuum Science & Technology B: Microelectronics and Nanometer Structures*, **19** (4), 1328–1333.

149 Mohammad, S.N., Salvador, A. and Morkoç, H. (1995) *Proceedings of the IEEE*, **83**, 1306.

150 Pearton, S.J., Zolper, J.C., Shul, R.J. and Ren, F. (1999) GaN: processing, defects, and devices. *Journal of Applied Physics*, **86**, 1.

151 Maruska, H.P., Anderson, L.J. and Stevenson, D.A. (1974) *Journal of the Electrochemical Society*, **121**, 1202.

152 Lagerstedt, O. and Monemar, B. (1979) *Physical Review B: Condensed Matter*, **19**, 3064.

153 Maruska, H.P., Anderson, L.J. and Stevenson, D.A. (1974) *Journal of the Electrochemical Society*, **121**, 1202.

154 Krüger, J., Sudhir, G.S., Corlatan, D., Cho, Y., Kim, Y., Klockenbrink, R., Ruvimov, S., Liliental-Weber, Z., Kisielowski, C., Rubin, M., Weber, E.R., McDermott, B., Pittman, R. and Gertner, E.R. (1997) Proceedings of the Fall '97 Meeting of the Materials Research Society, Boston.

155 Leszczynski, M., Suski, T., Domagala, J. and Prystawko, P. (1999) Lattice parameters of the group III-nitrides, in *Properties, Processing and Applications of Gallium Nitride and Related Semiconductors* (eds J.H. Edgar, S. Strite, I. Akasaki, H. Amano and C. Wetzel), EMIS Data Review Series, No. 23, INSPEC, The Institution of Electrical Engineers, Stevenage, UK, pp. 6–10.

156 Liu, C., Bensching, B., Volz, K. and Rauschenbach, B. (1997) *Applied Physics Letters*, **71**, 2313.

157 Akasaki, I. and Amano, H. (1994) *Properties of Group III Nitrides* (ed. J.H. Edgar), IEE EMIS Data Review Series, INSPEC, The Institution of Electrical Engineers, Stevenage, UK, p. 222.

158 Van Camp, P.E., Van Doren, V.E. and Devreese, J.T. (1992) *Solid State Communications*, **81**, 23.

159 Murnaghan, F.D. (1944) *Proceedings of the National Academy of Sciences of the United States of America*, **30**, 244.

160 Polian, A. (1999) Mechanical properties of the group III nitrides, in *Properties, Processing and Applications of Gallium Nitride and Related Semiconductors* (eds J.H. Edgar, S. Strite, I. Akasaki, H. Amano and C. Wetzel), EMIS Data Review Series, No. 23, INSPEC, The Institution of Electrical Engineers, Stevenage, UK, pp. 11–20.

161 Miwa, K. and Fukumoto, A. (1993) *Physical Review B: Condensed Matter*, **48**, 7897.

162 Savastenko, V.A. and Sheleg, A.U. (1978) *Physica Status Solidi a: Applied Research*, **48**, K135.

163 Chetverikova, I.F., Chukichev, M.V. and Rastorguev, L.N. (1986) *Inorganic Materials*, **22**, 53.

164 Sherwin, M.E. and Drummond, T.J. (1991) *Journal of Applied Physics*, **69**, 8423.

165 Deger, C., Born, E., Angerer, H., Ambacher, O., Stutzmann, M., Hornsteiner, J., Riha, E. and Fischerauer, G. (1998) *Applied Physics Letters*, **72**, 2400.

166 Yamaguchi, M., Yagi, T., Azuhata, T., Sota, T., Suzuki, K., Chichibu, S. and Nakamura, S. (1997) *Journal of Physics: Condensed Matter*, **9**, 241.

167 Kim, K.W., Lambert, W.R.L. and Segall, B. (1996) *Physical Review B: Condensed Matter*, **53**, 16310.

168 Kim, K.W., Lambert, W.R.L. and Segall, B. (1994) *Physical Review B: Condensed Matter*, **50**, 1502.

169 Davydov, V.Yu., Kitaev, Yu.E., Goncharuk, I.N., Smirnov, A.N., Graul, J., Semchinova, O., Uffmann, D., Smirnov, M.B., Mirgorodsky, A.P. and Evarestov, R.A. (1998) *Physical Review B: Condensed Matter*, **58**, 12899.

170 Yamaguchi, M., Yagi, T., Sota, T., Deguchi, T., Shimada, K. and Nakamura, S. (1999) *Journal of Applied Physics*, **85**, 8502.

171 Schwarz, R.B., Khachaturyan, K. and Weber, E.R. (1997) *Applied Physics Letters*, **70**, 1122.

172 Bergman, L., Dutta, M. and Nemanich, R.J. (2000) Raman scattering spectroscopy and analyses of III–V nitride based materials, in *Raman Scattering in Material Science*, Springer, Berlin, Chapter 7.

173 Cardona, M. (1982) *Light Scattering in Solids II*, *Springer Topics in Applied Physics*, vol. 50 (eds M. Cardona and G. Güntherodt), Springer, Berlin, pp. 19–178.

174 Harima, H. (2002) Properties of GaN and related compounds studied by means of Raman scattering. *Journal of Physics: Condensed Matter*, **14**, R967–R993.

175 Arguello, C.A., Rousseau, D.L. and Porto, S.P.S. (1969) *Physical Review B: Condensed Matter*, **181**, 1351.

176 Cingolani, A., Ferrara, M., Lugara, M. and Scamarcio, G. (1986) *Solid State Communications*, **58**, 823.

177 Huang, D., Yun, F., Visconti, P., Reshchikov, M.A., Wang, D., Morkoç, H., Rode, D.L., Farina, L.A., KurdakÇ., Tsen, K.T., Park, S.S. and Lee, K.Y. (2001) Hall mobility and carrier concentration in GaN free-standing templates grown by hydride vapor phase epitaxy with high quality. *Solid State Electronics*, **45** (5), 711–715.

178 Wagner, J.M. and Bechstedt, F. (2002) *Physical Review B: Condensed Matter*, **66**, 115202.

179 Miyoshi, S., Onabe, K., Ohkouchi, N., Yaguchi, H., Ito, R., Fukutsu, S. and Shraki, Y. (1992) *Journal of Crystal Growth*, **124**, 439.

180 Miller, S.C. and Love, W.F. (1967) *Tables of Irreducible Representations of Space Groups and Corepresentations of Magnetic Space Groups, Pruett, Boulder, CO.*

181 Davydov, V.Yu., Averkiev, N.S., Goncharuk, I.N., Nelson, D.K., Nikitina, I.P., Polkovnikov, A.S., Smirnov, A.N., Jacobson, M.A. and Semchinova, O.K. (1997) *Journal of Applied Physics*, **82**, 5097.

182 Leszczynski, M. and Walker, J.F. (1993) *Applied Physics Letters*, **62**, 1484–1487.

183 Sime, J.R. and Margrave, J.L. (1956) *The Journal of Physical Chemistry*, **60**, 810.

184 Morimoto, Y. (1974) *Journal of the Electrochemical Society*, **121**, 1383.

185 Furtado, M. and Jacob, G. (1983) *Journal of Crystal Growth*, **64**, 257.

186 Gordienko, S.P., Samsonov, G.V. and Fesenko, V.V. (1964) *Soviet Journal of Physical Chemistry*, **38**, 1620.

187 Munir, Z.A. and Searcy, A.W. (1965) *Journal of Chemical Physics*, **42**, 4223.

188 Groh, R., Gerey, G., Bartha, L. and Pankove, J.I. (1974) *Physica Status Solidi a: Applied Research*, **26**, 353.

189 Munir, Z.A. and Searcy, A.W. (1965) *Journal of Chemical Physics*, **42**, 4223.

190 Thurmond, C.D. and Logan, R.A. (1972) *Journal of the Electrochemical Society*, **119**, 622.

191 Karpinski, J., Jun, J. and Porowski, S. (1984) *Journal of Crystal Growth*, **66**, 1.

192 Grzegory, I., Krukowski, S., Leszczynski, M., Perlin, P., Suski, T. and Porowski, S. High pressure crystallization of GaN, in *Nitride Semiconductors – Handbook on Materials and Devices* (eds P. Ruterana, M. Albrecht and J. Neugebauer), Wiley-VCH Verlag GmbH, Weinheim, Germany.

193 Sasaki, T. and Matsuoka, T. (1995) *Journal of Applied Physics*, **77**, 192.

194 Madar, R., Jacob, G., Hallais, J. and Fruchart, R. (1975) *Journal of Crystal Growth*, **31**, 197.

195 Slack, G.A. and McNelly, T.F. (1976) *Journal of Crystal Growth*, **34**, 263.

196 Ambacher, O. (1998) Growth and applications of group III-nitrides. *Journal of Physics D: Applied Physics*, **31**, 2653.

197 Matsuoka, T. (2004) Progress in nitride semiconductors from GaN to InN – MOVPE growth and characteristics. *Superlattices and Microstructures*, **37** (1), 19–32.

198 Popovici, G. and Morkoç, H. (1999) Growth and doping of and defects in III-nitrides, in *GaN and Related Materials II: Optoelectronic Properties of Semiconductors and Superlattices* (ed. S.J. Pearton, series ed. M.O. Manaresh), vol. 7, Gordon and Breach, Amsterdam, pp. 93–172.

199 Ambacher, O., Brandt, M.S., Dimitrov, R., Metzger, T., Stutzmann, M., Fischer, R.A., Miehr, A., Bergmaier, A. and Dollinger, G. (1996) *Journal of Vacuum Science & Technology B: Microelectronics and Nanometer Structures*, **14**, 3532.

200 Redhead, P.A. (1962) *Vacuum*, **12**, 203; Redhead, P.A. (1962) *Journal of Crystal Growth*, **9**, 158.

201 Madar, R., Jacob, G., Hallais, J. and Fruchart, R. (1975) *Journal of Crystal Growth*, **31**, 197.

202 Karpinski, J. and Porowski, S. (1984) *Journal of Crystal Growth*, **66**, 11.

203 Glushko, W.P. (ed.) (1979) *Termodinamiczeskije swojstwa indiwidualnych weszczestw*, Nauka, Moscow (in Russian).

204 Zinowiev, W.E. (1989) *Teplofiziczeskije swojstwa metallow pri wysokich temperaturach*, Metallurgia, Moscow (in Russian).

205 Bhandari, C.M. and Rowe, D.M. (1988) *Thermal Conduction in Semiconductors*, John Wiley & Sons, Inc., New York.

206 Kittel, C. (1986) *Introduction to Solid State Physics*, 6th edn, John Wiley & Sons, Inc., New York, p. 150.

207 Sichel, E.K. and Pankove, J.I. (1977) *Journal of Physics and Chemistry of Solids*, **38**, 330.

208 Witek, A. (1998) Some aspects of thermal conductivity of isotopically pure diamond – a comparison with nitrides. *Diamond & Related Materials*, **7** (7), 962–964.

209 Florescu, D.I., Asnin, V.M., Pollak, F.H., Jones, A.M., Ramer, J.C., Schurman, M.J. and Ferguson, I. (2000) *Applied Physics Letters*, **77**, 1464.

210 Kotchetkov, D., Zouand, J., Balandin, A., Florescu, D.I. and Pollak, F.H. (2001) Effect of dislocations on thermal conductivity of GaN. *Applied Physics Letters*, **79** (26), 4316–4318.

211 Florescu, D.I., Asnin, V.M., Pollak, F.H. and Molnar, R.J. (2000) *Materials Research Society Symposium Proceedings*, **595**, 3.89.1.

212 Florescu, D.I., Asnin, V.M., Pollak, F.H., Molnar, R.J. and Wood, C.E.C. (2000) *Journal of Applied Physics*, **88**, 3295.

213 Florescu, D.I., Pollak, F.H., Lanford, W.B., Khan, F., Adesida, I. and Molnar, R.J. (2000) Plasma-induced effects on the thermal conductivity of hydride vapor phase epitaxy grown n-GaN/sapphire (0001). *Materials Research Society Symposium Proceedings*, **639**, G11.57.

214 Kittel, C. *Introduction to Solid State Physics*, 4th edn, John Wiley & Sons, Inc., New York, p. 215.

215 Koshchenko, V.I., Demidienko, A.F., Sabanova, L.D., Yachmenev, V.E., Gran, V.E. and Radchenko, A.E. (1979) *Inorganic Materials*, **15**, 1329–1330 (translation of *Izv. Akad. Nauk SSSR, Neorg. Mater.*, 1979, **15**, 1686–1687).

216 Demidienko, A.F., Koshchenko, V.I., Sabanova, L.D. and Gran, V.E. (1975) *Russian Journal of Physical Chemistry*, **49**, 1585.

217 Elwell, D. and Elwell, M.M. (1988) *Progress in Crystal Growth and Characterization of Materials*, **17**, 53.

218 Porowski, S. and Grzegory, I. (1994) *Properties of Group III Nitrides* (ed. J.H. Edgar), IEE EMIS Data Review Series, No. 11, INSPEC, The Institution of Electrical Engineers, Stevenage, UK, pp. 71, 76, 83.

219 Oliner, A.A. (ed.) (1978) *Acoustic Surface Waves, Topics in Applied Physics*, vol. 24, Springer, Berlin.

220 Petrov, I., Mojab, E., Powell, R., Greene, J., Hultman, L. and Sundgren, J.E. (1992) *Applied Physics Letters*, **60**, 2491.

221 Vollstadt, H., Ito, E., Akaishi, M., Akimoto, S. and Fukunaga, O. (1990) *Proceedings of the Japan Academy, Series B*, **66**, 7.

222 Ruiz, E., Alvarez, S. and Alemany, P. (1994) *Physical Review B: Condensed Matter*, **49**, 7115.

223 Tsubouchi, K. and Mikoshiba, N. (1985) Zero-temperature coefficient SAW devices on AlN epitaxial films. *IEEE Transactions on Sonics and Ultrasonics*, **32**, 634–644.

224 Tsubouchi, T., Sugai, K. and Mikoshiba, N. (1981) Ultrosonic Symposium Proceedings, IEEE, New York, p. 375.

225 Taylor, K.M. and Len, C. (1960) *Journal of the Electrochemical Society*, **107**, 308.

226 Cline, C.F. and Kalm, J.S. (1963) *Journal of the Electrochemical Society*, **110**, 773.

227 Gleize, J., Renucci, M.A., Frandon, J., Bellett-Amalric, E. and Daudin, B. (2003) *Journal of Applied Physics*, **93**, 2065.

228 Tischler, J.G. and Freitas, J.A., Jr (2004) Anharmonic decay of phonons in strain free wurtzite AlN. *Applied Physics Letters*, **85**, 1943.

229 Bergman, L., Alexson, D., Murphy, P.L., Nemanich, R.J., Dutta, M., Stroscio, M.A., Balkas, C., Shin, H. and Davis, R.F. (1999) *Physical Review B: Condensed Matter*, **59**, 12977.

230 Ribeiro, C.T.M., Alvarez, F. and Zanatta, A.R. (2002) *Applied Physics Letters*, **81**, 1005.

231 See, for example, Colthup, N.B., Daly, L.H. and Wiberley, S.E. (1990) *Infrared and Raman Spectroscopy*, Academic Press, San Diego, FL.

232 Ren, Z.M., Lu, Y.F., Ni, H.Q., Liew, T.Y.F., Cheong, B.A., Chow, S.K., Ng, M.L. and Wang, J.P. (2000) *Journal of Applied Physics*, **88**, 7346.

233 Karch, K. and Bechstedt, F. (1997) *Physical Review B: Condensed Matter*, **56**, 7404.

234 Tütüncü, H.M. and Srivastava, G.P. (2000) Phonons in zinc-blende and wurtzite phases of GaN, AlN, and BN with the adiabatic bond-charge model. *Physical Review B: Condensed Matter*, **62** (8), 5028–5235.

235 Class, W. (1968) NASA Report CR-1171.

236 Van Vechten, J.A. (1973) *Physical Review B: Condensed Matter*, **7**, 1479.

237 Yim, W.M. and Paff, R.J. (1974) *Journal of Applied Physics*, **45**, 1456.

238 Mah, A.D., King, E.G., Weller, W.W. and Christensen, A.U. (1961) *Bureau of Mines Report of Investigations*, **5716**, 18.

239 Glushko, V.P., Gurevich, L.V., Bergman, G.A., Weitz, I.V., Medvedev, V.A., Chachkurov, G.A. and Yungman, V.S. (1979) *Thermodinamicheskiie swoistwa indiwidualnych weshchestw*, vol. 1, Nauka, Moscow, pp. 164–165.

240 Slack, G.A., Tanzilli, R.A., Pohl, R.O. and Vandersande, J.W. (1987) *Journal of Physics and Chemistry of Solids*, **48**, 641.

241 Slack, G.A. and McNelly, T.F. (1977) *Journal of Crystal Growth*, **42**, 560 (AlN from pellet drop, sublimation, and final growth).

242 Florescu, D.I., Asnin, V.M. and Pollak, F.H. (2001) Thermal conductivity of GaN and AlN. *Compound Semiconductor*, **7** (2), 62.

243 Nikolaev, A., Nikitina, I., Zubrilov, A., Mynbaeva, M., Melnik, Y. and Dmitriev, V. (2000) *Materials Research Society Symposium Proceedings*, **595**, 6.5.1.

244 Edwards, J., Kawabe, K., Stevens, G. and Tredgold, R.H. (1965) *Solid State Communications*, **3**, 99.

245 Cox, G.A., Cummins, D.O., Kawabe, K. and Tredgold, R.H. (1967) *Journal of Physics and Chemistry of Solids*, **28**, 543.

246 Yim, W.M., Stotko, E.J., Zanzucchi, P.J., Pankove, J.I., Ettenberg, M. and Gilbert, S.L. (1973) *Journal of Applied Physics*, **44**, 292.

247 Yoshida, S., Misawa, S., Fujii, Y., Takada, S., Hayakawa, H., Gonda, S. and Itoh, A. (1979) *Journal of Vacuum Science & Technology*, **16**, 990.

248 Chu, T.L., Ing, D.W. and Noreika, A.J. (1967) *Solid State Electronics*, **10**, 1023.

249 Rutz, R.F. (1976) *Applied Physics Letters*, **28**, 379.

250 Rutz, R.F., Harrison, E.P. and Cuome, J.J. (1973) *IBM Journal of Research*, **17**, 61.

251 Edwards, J., Kawabe, K., Stevens, G. and Tredgold, R.H. (1965) *Solid State Communications*, **3**, 99.

252 Kawabe, K., Tredgold, R.H. and Inuishi, Y. (1967) *Electrical Engineering in Japan*, **87**, 62.

253 Harris, J.H. and Youngman, R.A. (1994) *Properties of Group III Nitrides* (ed. J.H. Edgar), IEE EMIS Data Review Series, No. 11, INSPEC, The Institution of Electrical Engineers, Stevenage, UK, p. 203.

254 Pacesova, S. and Jastrabik, L. (1979) *Czechoslovak Journal of Physics B*, **29**, 913.

255 Youngman, R.A. and Harris, J.H. (1990) *Journal of the American Ceramic Society*, **73**, 3238.

256 Harris, J.H., Youngman, R.A. and Teller, R.G. (1990) *Journal of Materials Research*, **5**, 1763.

257 Shishkin, Y., Devaty, R.P., Choyke, W.J., Feng Yun, King, T. and Morkoç, H., (2001) Near bandedge cathodoluminescence studies of AlN films: dependence on MBE growth conditions. International Conference on Nitride Semiconductors, Denver, CO, July; *Physica Status Solidi a: Applied Research*, **188** (2), 591–594.

258 Perry, P.B. and Rutz, R.F. (1978) *Applied Physics Letters*, **33**, 319.

259 Pastrnak, J. and Roskovcova, L. (1968) *Physica Status Solidi*, **26**, 591.

260 Pastrnak, J. and Souckova, L. (1963) *Physica Status Solidi*, **9**, K71.

261 Pastrnak, J. and Roskovcova, L. (1965) *Physica Status Solidi*, **11**, K73.

262 Karel, F., Pastrnak, J., Hejduk, J. and Losik, V. (1966) *Physica Status Solidi*, **15**, 693.

263 Karel, F. and Pastrnak, J. (1969) *Czechoslovak Journal of Physics B*, **19**, 78.

264 Karel, F. and Pastrnak, J. (1970) *Czechoslovak Journal of Physics B*, **20**, 46.

265 Karel, F. and Mares, J. (1972) *Czechoslovak Journal of Physics B*, **22**, 847.

266 Karel, F. and Mares, J. (1973) *Czechoslovak Journal of Physics B*, **23**, 652.

267 Juza, R. and Hahn, H. (1938) *Zeitschrift für Anorganishce und Allgemeine Chemie*, **239**, 282.

268 Matsuoka, T. (2004) MOVPE growth and characteristics of nitride semiconductors from GaN to InN, in *Advanced Materials in Electronics* (ed. Q. Guo), Research Signpost, pp. 46–83.

269 Osamura, K., Naka, S. and Murakami, Y. (1975) *Journal of Applied Physics*, **46**, 3432.

270 Puychevrier, N. and Menoret, M. (1976) *Thin Solid Films*, **36**, 141.

271 Tansley, T.L. and Foley, C.P. (1986) *Journal of Applied Physics*, **59**, 3241.

272 Westra, K.L., Lawson, R.P.W. and Brett, M.J. (1988) *Journal of Vacuum Science & Technology A: Vacuum Surfaces and Films*, **6**, 1730.

273 Bhuiyan, A.G., Hashimoto, A. and Yamamoto, A. (2003) Indium nitride (InN): a review on growth, characterization, and properties. *Journal of Applied Physics*, **94** (5), 2779–2808.

274 Davydov, V.Yu., Klochikhin, A.A., Emtsev, V.V., Ivanov, S.V., Vekshin, V.V., Bechstedt, F., Furthmüller, J., Harima, H., Mudryi, A.V., Hashimoto, A., Yamamoto, A., Aderhold, J., Graul, J. and Haller, E.E. (2002) *Physica Status Solidi b: Basic Research*, **230**, R4.

275 Araki, T., Saito, Y., Yamaguchi, T., Kurouchi, M., Nanishi, Y. and Naoi, H. (2004) Radio frequency-molecular beam epitaxial growth of InN epitaxial films on (0 0 0 1) sapphire and their properties. *Journal of Vacuum Science & Technology B: Microelectronics and Nanometer Structures*, **22** (4), 2139–2143.

276 Fritsch, D., Schmidt, H. and Grundmann, M. (2004) Band dispersion relations of zinc-blende and wurtzite InN. *Physical Review B: Condensed Matter*, **69**, 165204.

277 Wu, J. and Walukiewicz, W. (2004) Band gaps of InN and group III-nitride alloys. *Superlattices and Microstructures*. **34**, 63–75.

278 Butcher, K.S.A. (2004) InN, a historic review – from obscurity to controversy, in Advanced Materials in Electronics (ed. Q. Guo), Research Signpost.

279 Butcher, K.S.A. and Tansley, T.L. (2005) InN, latest development and a review of the band-gap controversy. *Superlattices and Microstructures*, **38** (1), 1–37.

280 Shubina, T.V., Ivanov, S.V., Jmerik, V.N., Solnyshkov, D.D., Vekshin, V.A., Kop'ev, P.S., Vasson, A., Leymarie, J., Kavokin, A., Amano, H., Shimono, K., Kasic, A. and Monemar, B. (2004) Mie resonances, infrared emission, and the band gap of InN. *Physical Review Letters*, **92** (11), 117407–117410.

281 Butcher, K.S.A., Wintrebert-Fouquet, M., Chen, P.P., Timmers, H. and Sherestha, S.K. (2003) Detailed analysis of the absorption data for InN. Presented at the International Symposium on Point Defects and Nonstoichiometry, March 2003, Sendai, Japan; *Material Science in Semiconductor Processing*, 2003, **6**, 351–354.

282 Wolfe, C.M. and Stillman, G.E. (1975) Apparent mobility enhancement in inhomogeneous crystals, in *Semiconductors and Semimetals*, vol. 10 (eds R.K. Willardson and A.C. Beer), Academic Press, New York, pp. 175–220.

283 Yamaguchi, S., Kariya, M., Nitta, S., Takeuchi, T., Wetzel, W., Amano, H. and Akasaki, I., (1999) Structural properties of InN on GaN grown by metalorganic vapor-phase epitaxy. *Journal of Applied Physics*, **85** (11), 7682–7688.

284 Strite, S., Chandrasekhar, D., Smith, D.J., Sariel, J., Chen, H., Teraguchi, N. and Morkoç, H. (1993) *Journal of Crystal Growth*, **127**, 204.

285 Hahn, H. and Juza, R. (1940) *Zeitschrift für Anorganishce und Allgemeine Chemie*, **244**, 111.

286 Tansley, T.L. (1994) *Properties of Group III Nitrides*, (ed. J.H. Edgar), IEE EMIS Data Review Series, No. 11, INSPEC, The Institution of Electrical Engineers, Stevenage, UK, p. 35.

287 van Camp, P.E., van Doren, V.E. and Devreese, J.T. (1990) *Physical Review B: Condensed Matter*, **41**, 1598.

288 Kubota, K., Kobayashi, Y. and Fujimoto, K. (1989) *Journal of Applied Physics*, **66**, 2984.

289 Inushima, T., Yaguchi, T., Nagase, A., Iso, A., Shiraishi, T. and Ooya, S. (1995) Optical and electrical properties of InN grown by the atomic layer epitaxy. 7th International Conference on Indium Phosphide and Related Materials (Cat. No. 95CH35720), IEEE, New York, pp. 187–190.

290 Inushima, T., Yaguchi, T., Nagase, A., Iso, A. and Shiraishi, T. (1996) Investigation of optical properties of InN grown by atomic layer epitaxy. Presented at the International Meeting on Silicon Carbide and Related Materials, 1995, Kyoto, Japan, IOP Publishing, Bristol, UK, pp. 971–974.

291 Osamura, K., Naka, S. and Murakami, Y. (1975) *Journal of Applied Physics*, **46**, 3432.

292 Sheleg, A.V. and Savastenko, V.A. (1976) *Vestsi Akademii Nauk USSR, Seria Fiziki i Matematika Nauk*, **3**, 126.

293 Krukowski, S., Witek, A., Adamczyk, J., Jun, J., Bockowski, M., Grzegory, I., Lucznik, B., Nowak, G., Wroblewski, M., Presz, A., Gierlotka, S., Stelmach, S., Palosz, B., Porowski, S. and Zinn, P. (1998) *Journal of Physics and Chemistry of Solids*, **59**, 289–295.

294 Tansley, T.L. and Foley, C.P. (1985) Proceedings of the 3rd International Conference on Semiinsulating III–V Materials, Warm Springs, OR, 1984 (ed. J.S. Blakemore), Shiva, London.

295 Bryden, W.R., Ecelberger, S.A., Hawley, M.E. and Kistenmacher, T.J. (1994) *Diamond SiC, Nitride Wide Bandgap Semiconductors* (eds C.H. Carter Jr, G. Gildenblat, S. Nakamura and R.J. Nemanich), Materials Research Society, Pittsburgh, PA; *Materials Research Society Symposium Proceedings*, **339**, 497.

296 Bryden, W.R. and Kistenmacher, T.J. (1994) *Properties of Group X Nitrides* (ed. J.H. Edgar), IEE EMIS Data Review Series, No. 11, INSPEC, The Institution of Electrical Engineers, Stevenage, UK, pp. 117–118.

297 Abernathy, C.R., Pearton, S.J., Ren, F. and Wisk, P.W. (1993) *Journal of Vacuum Science & Technology B: Microelectronics and Nanometer Structures*, **11**, 179.

298 Maruyama, T. and Morishita, T. (1994) *Journal of Applied Physics*, **76**, 5809.

299 Yamaguchi, S., Kariya, M., Nitta, S., Takeuchi, T., Wetzel, C., Amano, H. and Akasaki, I. (1999) *Journal of Applied Physics*, **85**, 7682.

300 Lu, H., Schaff, W.J., Hwang, J., Wu, H., Yeo, W., Pharkya, A. and Eastman, L.F. (2000) *Applied Physics Letters*, **77**, 2548.

301 Aderhold, J., Davydov, V.Yu., Fedler, F., Klausing, H., Mistele, D., Rotter, T., Semchinova, O., Stemmer, J. and Graul, J. (2001) *Journal of Crystal Growth*, **222**, 701.

302 Lu, H., Schaff, W.J., Hwang, J., Wu, H., Koley, G. and Eastman, L.F. (2001) *Applied Physics Letters*, **79**, 1489.

303 Motlan, Goldys, E.M. and Tansley, T.L. (2002) *Journal of Crystal Growth*, **241**, 165.

304 Saito, Y., Yamaguchi, T., Kanazawa, H., Kano, K., Araki, T., Nanishi, Y., Teraguchi, N. and Suzuki, A. (2002) *Journal of Crystal Growth*, **237–239**, 1017.

305 Lu, H., Schaff, W.J., Eastman, L.F., Wu, J., Walukiewicz, W., Yu, K.M., Auger, J.W., III, Haller, E.E. and Ambacher, O. (2002) Conference Digest of the 44th Electronic Materials Conference, Santa Barbara, p. 2; Schaff, W.J., Lu, H., Eastman, L.F., Walukiewicz, W., Yu, K.M., Keller, S., Kurtz, S., Keyes, B. and Gevilas, L. (2004) Electrical properties of InN grown by molecular beam epitaxy. Fall 2004 ECS Meeting. *State-of-the-Art Program on Compound Semiconductors XLI and Nitride and Wide Bandgap Semiconductors for Sensors, Photonics, and Electronics*, vol. 2004-06 (eds V.-H. Ng and A.G. Baca).

306 Higashiwaki, M. and Matsui, T. (2003) *Journal of Crystal Growth*, **252**, 128.

307 Look, D.C., Lu, H., Schaff, W.J., Jasinski, J. and Liliental-Weber, Z. (2002) *Applied Physics Letters*, **80**, 258.

308 Tansley, T.L. and Foley, C.P. (1984) *Electronics Letters*, **20**, 1066.

309 O'Leary, S.K., Foutz, B.E., Shur, M.S., Bhapkar, U.V. and Eastman, L.F. (1998) *Journal of Applied Physics*, **83**, 826.

310 Bellotti, E., Doshi, B.K., Brennan, K.F., Albrecht, J.D. and Paul Ruden, P. (1999) Ensemble Monte Carlo study of electron transport in wurtzite InN. *Journal of Applied Physics*, **85**, 916.

311 Foutz, B.E., Eastman, L.F., Bhapkar, U.V. and Shur, M.S. (1997) Comparison of high field electron transport in GaN and GaAs. *Applied Physics Letters*, **70**, 2849–2851.

312 Foutz, B.E., O'Leary, S.K., Shur, M.S. and Eastman, L.F. (1999) Transient electron transport in wurtzite GaN, InN, and AlN. *Journal of Applied Physics*, **85**, 7727–7734.

313 Wakahara, A., Tsuchiya, T. and Yoshida, A. (1990) *Journal of Crystal Growth*, **99**, 385.

314 Kubota, K., Kobayashi, Y. and Fujimoto, K. (1989) *Journal of Applied Physics*, **66**, 2984–2988.

315 Guo, Q., Kato, O., Fujisawa, M. and Yoshida, A. (1992) Optical constants of indium nitride. *Solid State Communications*, **83** (9), 721–723.

316 Guo, Q., Ogawa, H., and Yoshida, A., (1996) Optical properties of indium nitride in vacuum ultraviolet region. *Journal of Electron Spectroscopy & Related Phenomena*, **79**, 9.

317 Yodo, T., Yona, H., Ando, H., Nosei, D. and Harada, Y. (2002) *Applied Physics Letters*, **80**, 968.

318 Inushima, T., Mamutin, V.V., Vekshin, V.A., Ivanov, S.V., Sakon, T., Motokawa, M. and Ohoya, S. (2001) *Journal of Crystal Growth*, **481**, 227–228.

319 Davydov, V.Yu., Klochikhin, A.A., Seisyan, R.P., Emtsev, V.V., Ivanov, S.V., Bechstedt, F., Furthmuller, J., Harima, H., Mudryi, A.V., Aderhold, J., Semchinova, O. and Graul, J. (2002) *Physica Status Solidi b: Basic Research*, **229**, R1.

320 Hamberg, I. and Granqvist, C.G. (1986) *Journal of Applied Physics Reviews*, **60**, R123.

321 Alexandrov, D., Butcher, K.S.A. and Wintrebert-Fouquet, M. (2004) Absorption and photoluminescence features caused by defects in InN. *Journal of Crystal Growth*, **269** (1), 77–86.

322 Alexandrov, D., Butcher, K.S.A. and Wintrebert-Fouquet, M. (2004) Energy band gaps of InN containing oxygen and of the $In_xAl_{1-x}N$ interface layer formed during InN film growth. *Journal of Vacuum Science & Technology A: Vacuum Surfaces and Films*, **22**, 954–961.

323 Trainor, J.W. and Rose, K. (1974) *Journal of Electronic Materials*, **3**, 821.

324 Haddad, D.B., Takur, J.S., Naik, V.M., Auner, G.W., Naik, R. and Wenger, L.E. (2003) *Materials Research Society Symposium Proceedings*, **743**, 701.

325 Hovel, H.J. and Cuomo, J.I. (1972) *Applied Physics Letters*, **20**, 71.

326 Nataraian, B.R., Eltoukhy, A.H., Greene, J.E. and Barr, T.L. (1980) *Thin Solid Films*, **69**, 201.

327 Sullivan, B.T., Parsons, R.R., Westra, K.L. and Brett, M.J. (1988) *Journal of Applied Physics*, **64**, 4144.

328 Wintrebert-Fouquet, M., Butcher, K.S.A. and Chen, P.P.-T. (2003) InN grown by remote plasma enhanced chemical vapour deposition. Presented at the First International InN Workshop, November 16–20, Fremantle, Australia.

329 Butcher, K.S.A., Wintrebert-Fouquet, M., Chen, P.P.-T., Tansley, T.L. and Srikeaw, S. (2002) *Materials Research Society Symposium Proceedings*, **693**, 341.

330 Demangeot, F., Frandon, J., Pinquier, C., Caumont, M., Briot, O., Maleyre, B., Clur-Ruffenach, S. and Gil, B. (2003) Raman scattering in large single indium nitride dots: correlation between morphology and strain. *Physical Review B: Condensed Matter*, **68**, 245308.

331 Briot, O., Maleyre, B., Ruffenach, S., Pinquier, C., Demangeot, F., Frandon, J. and Gil, B. (2003) Absorption and Raman scattering processes in InN films and dots. Presented at the 1st International InN Workshop, November 16–20, Fremantle, Australia.

332 Tsen, K.T., Liang, W., Ferry, D.K., Hai Lu, Schaff, W.J., Özgür, Ü., Fu, Y., Moon, Y.T., Yun, F., Morkoç, H. and Everitt, H.O. (2005) Optical studies of carrier dynamics

and non-equilibrium optical phonons in nitride-based wide bandgap semiconductors. *Superlattices and Microstructures*, **38** (2), 77–114.

333 Shan, W., Song, J.J., Feng, Z.C., Schurman, M. and Stall, R.A. (1997) *Applied Physics Letters*, **71**, 2433.

334 Shan, W., Ager, J.W., III, Yu, K.M., Walukiewicz, W., Haller, E.E., Martin, M.C., McKinney, W.R. and Yang, W. (1999) *Journal of Applied Physics*, **85**, 8505.

335 Wolford, D.J. and Bradley, J.A. (1985) *Solid State Communications*, **53**, 1069.

336 Perlin, P., Gorczyca, I., Suski, T., Wisniewski, P., Lepkowski, S., Christansen, N.E., Svane, A., Hansen, M., DenBaars, S.P., Damilano, D., Grandjean, N. and Massies, S.P. (2001) *Physical Review B: Condensed Matter*, **64**, 115319.

337 Tyagai, V.A., Snitko, O.V., Evstigneev, A.M. and Krasiko, A.N. (1981) *Physica Status Solidi b: Basic Research*, **103**, 589.

338 Davydov, V., Klochikhin, A., Ivanov, S., Aderhold, J. and Yamamoto, A. (2003) Growth and properties of InN, in *Nitride Semiconductors – Handbook on Materials and Devices*, (eds. P. Ruterana, M. Albrecht and J. Neugebauer), Wiley-VCH Verlag GmbH, Weinheim.

339 Kasic, A., Schebert, M., Saito, Y., Nanishi, Y. and Wagner, G. (2002) Effective electron mass and phonon modes in n-type hexagonal InN. *Physical Review B: Condensed Matter*, **65**, 115206.

340 Perlin, P., Litwin-Staszewska, E., Suchanek, B., Knap, W., Camassel, J., Suski, T., Piotrzkowski, R., Grzegory, I., Porowski, S., Kaminska, E. and Chervin, J.C. (1996) Determination of the effective mass of GaN from infrared reflectivity and Hall effect. *Applied Physics Letters*, **68** (8), 1114–1116.

341 Wu, J., Walukiewicz, W., Shall, W., Yu, K.M., Ager, J.W., III, Haller, E.E., Lu, H. and Schaff, W.J. (2002) Effects of the narrow band gap on the properties of InN. *Physical Review B: Condensed Matter*, **66**, 201403.

342 Osamura, K., Naka, S. and Murakami, Y. (1975) *Journal of Applied Physics*, **46**, 3432.

343 Matsuoka, T. (1994) *Properties of Group III Nitrides* (ed. J.H. Edgar), IEE EMIS Data Review Series, No. 11, INSPEC, The Institution of Electrical Engineers, Stevenage, UK, pp. 231–238.

344 Yamasaki, S., Asami, S., Shibata, N., Koike, M., Manabe, K., Tanaka, T., Amano, H. and Akasaki, I. (1995) *Applied Physics Letters*, **66**, 1112.

345 Yoshida, S., Misawa, S. and Gonda, S. (1982) *Journal of Applied Physics*, **53**, 6844.

346 Khan, M.R.H., Koide, Y., Itoh, H., Sawaki, N. and Akasaki, I. (1986) *Solid State Communications*, **60**, 509.

347 Zoroddu, A., Bernardini, F., Ruggerone, P. and Fiorentini, V. (2001) First-principles prediction of structure, energetics, formation enthalpy, elastic constants, polarization, and piezoelectric constants of AlN, GaN, and InN: comparison of local and gradient-corrected density-functional theory. *Physical Review B: Condensed Matter*, **64** (45), 208.

348 Amano, H., Takeuchi, T., Sota, S., Sakai, H. and Akasaki, I. (1997) *III–V Nitrides* (eds. F.A. Ponce, T.D. Moustakas, I. Akasaki and B. Monemar), *Materials Research Society Symposium Proceedings*, **449**, 1143–1150.

349 Yoshida, S., Misawa, S. and Gonda, S. (1983) *Journal of Vacuum Science & Technology B: Microelectronics and Nanometer Structures*, **1**, 250.

350 Wickenden, D.K., Bargeron, C.B., Bryden, W.A., Miragliova, J. and Kistenmacher, T.J. (1994) *Applied Physics Letters*, **65**, 2024.

351 Koide, Y., Rob, H., Khan, M.R.H., Hiramatsu, K., Sawaki, N. and Akasaki, I. (1987) *Journal of Applied Physics*, **61**, 4540.

352 Khan, M.A., Skogman, R.A., Schulze, R.G. and Gershenzon, M. (1983) *Applied Physics Letters*, **43**, 492.

353 Korkotashvili, G.A., Pikhtin, A.N., Pichugin, I.G. and Tsaregorodtsev, A.M.

(1984) *Soviet Physics: Semiconductors*, **18**, 913.

354 Wethkamp, T., Wilmers, K., Esser, N., Richter, W., Ambacher, O., Angerer, H., Jungk, G., Johnson, R.L. and Cardona, M. (1998) *Thin Solid Films*, **313**, 745.

355 Paduano, Q.S., Weyburne, D.W., Bouthillette, L.O. and Alexander, M.N. (2002) 7th International Workshop on Wide Bandgap Nitrides, Abstract Book, Richmond, VA, 10–14 March, p. 21.

356 Nikishin, S.A., Faleev, N.N., Zubrilov, A.S., Antipov, V.G. and Temkin, H. (2000) *Applied Physics Letters*, **76**, 3028.

357 Shan, W., Ager, J.W., III, Yu, K.M., Walukiewicz, W., Haller, E.E., Martin, M.C., McKinney, W.R. and Yang, W. (1999) *Journal of Applied Physics*, **85**, 8505.

358 Özgür, Ü., Webb-Wood, G., Everitt, H.O., Yun, F. and Morkoç, H. (2001) *Applied Physics Letters*, **79**, 4103.

359 Wagner, J., Obloh, H., Kunzer, M., Maier, M., Kohler, K. and Johs, B. (2000) *Journal of Applied Physics*, **89**, 2779.

360 Jiang, H., Zhao, G.Y., Ishikawa, H., Egawa, T., Jimbo, T. and Umeno, M. (2001) *Journal of Applied Physics*, **89**, 1046.

361 Ochalski, T.J., Gil, B., Lefebvre, P., Grandjean, M., Leroux, M., Massies, J., Makamura, S. and Morkoç, H. (1999) *Applied Physics Letters*, **74**, 3353.

362 Lee, S.R., Lee, S.R., Wright, A.F., Crawford, M.H., Petersen, G.A., Han, J. and Biefeld, R.M. (1999) *Applied Physics Letters*, **74**, 3344.

363 Yun, F., Reshchikov, M.A., He, L., King, T., Morkoç, H., Novak, S.W. and Wei, L., (2002) Energy band bowing parameter in $Al_xGa_{1-x}N$ alloys. *Journal of Applied Physics: Rapid Communications*, **92**, 4837–4839.

364 Khan, M.A., Van Hove, J.M., Kuznia, J.N. and Olson, D.T. (1991) *Applied Physics Letters*, **58**, 2408.

365 Tanaka, T., Watanabe, A., Amano, H., Kobayashi, Y., Akasaki, I., Yamazaki, S. and Koike, M. (1994) *Applied Physics Letters*, **65**, 593.

366 Nagatomo, T., Kuboyama, T., Minamino, H. and Omoto, O. (1989) *Japanese Journal of Applied Physics*, **28**, L1334.

367 Matsuoka, T., Tanaka, H., Sasaki, T. and Katsui, K. (1990) Proceedings of the 16th International Symposium on GaAs and Related Compounds, 1989, Karuizawa, Institute of Physics Conference Series, vol. 106, Institute of Physics, Bristol, p. 141.

368 Yoshimoto, N., Matsuoka, T., Sasaki, T. and Katsui, A. (1991) *Applied Physics Letters*, **59**, 2251.

369 Matsuoka, T., Yoshimoto, N., Sasaki, T. and Katsui, A. (1992) *Journal of Electronic Materials*, **21**, 157.

370 Shimizu, M., Hiramatsu, K. and Sawaki, N. (1994) *Journal of Crystal Growth*, **145**, 209.

371 Ho, I.-H. and Stringfellow, G.B. (1996) *Applied Physics Letters*, **69**, 2701.

372 Osamura, K., Naka, S. and Murakami, Y. (1975) *Journal of Applied Physics*, **46**, 3432.

373 Koukitu, A., Takahashi, N., Taki, T. and Seki, H. (1996) *Japanese Journal of Applied Physics*, **35**, L673.

374 Kawaguchi, Y., Shimizu, M., Hiramatsu, K. and Sawaki, N. (1997) *Materials Research Society Symposium Proceedings*, **449**, 89.

375 Nakamura, S. and Mukai, T. (1992) *Japanese Journal of Applied Physics*, **31**, L1457.

376 Piner, E.L., Behbehani, M.K., El-Mastry, N.A., McIntosh, F.G., Roberts, J.C., Boutros, K.S. and Bedair, S.M. (1997) *Applied Physics Letters*, **70**, 461.

377 Wright, A.F., Leung, K. and van Schilfgaarde, M. (2001) Effects of biaxial strain and chemical ordering on the band gap of InGaN. *Applied Physics Letters*, **78** (2), 189–191.

378 Ferhat, M. and Bechstedt, F. (2002) First-principles calculations of gap bowing in $In_xGa_{1-x}N$ and $In_xAl_{1-x}N$ alloys: relation to structural and thermodynamic properties. *Physical Review B: Condensed Matter*, **65**, 0752131–0752137.

379 Sökeland, F., Rohlfing, M., Krüger, P. and Pollmann, J. (2003) Density functional and quasiparticle band-structure calculations for $Ga_xAl_{1-x}N$ and $Ga_xIn_{1-x}N$ alloys. *Physical Review B: Condensed Matter*, **68**, 075203-1–075203-11.

380 Pugh, S.K., Dugdale, D.J., Brand, S. and Abram, R.A. (1999) *Journal of Applied Physics*, **86**, 3768.

381 Teles, L.K., Furthmüller, J., Scolfaro, L.M.R., Leite, J.R. and Bechstedt, F. (2000) *Physical Review B: Condensed Matter*, **62**, 2475.

382 Teles, L.K., Furthmüller, J., Scolfaro, L.M.R., Leite, J.R. and Bechstedt, F. (2001) Influence of composition fluctuations and strain on gap bowing in $In_xGa_{1-x}N$. *Physical Review B: Condensed Matter*, **63**, 085204.

383 Nakamura, S. and Mukai, J. (1995) *Journal of Vacuum Science & Technology A: Vacuum Surfaces and Films*, **13**, 6844.

384 O'Donnell, K.P., Martin, R.W., Trager-Cowan, C., White, M.E., Esona, K., Deatcher, C., Middleton, P.G., Jacobs, K., van der Stricht, W., Merlet, C., Gil, B., Vantomme, A. and Mosselmans, J.F.W. (2001) *Materials Science & Engineering B: Solid State Materials for Advanced Technology*, **82**, 194.

385 Monroy, E., Gogneau, N., Enjalbert, F., Fossard, F., Jalabert, D., Bellet-Amalric, E., Dang, L.S. and Daudin, B. (2003) Molecular-beam epitaxial growth and characterization of quaternary III-nitride compounds. *Journal of Applied Physics*, **94** (5), 3121–3127.

386 Aumer, M.E., LeBoeuf, S.F., McIntosh, F.G. and Bedair, S.M. (1999) *Applied Physics Letters*, **75**, 3315.

387 Dimakis, E., Georgakilas, A., Androulidaki, M., Tsagaraki, K., Kittler, G., Kalaitzakis, F., Cengher, D., Bellet-Amalric, E., Jalabert, D. and Pelekanos, N.T. (2003) Plasma-assisted MBE growth of quaternary InAlGaN quantum well heterostructures with room temperature luminescence. *Journal of Crystal Growth*, **251** (1–4), 476–480.

388 Pereira, S., Correia, M.R., Monteiro, T., Pereira, E., Alves, E., Sequeira, A.D. and Franco, N. (2001) Compositional dependence of the strain-free optical band gap in $In_xGa_{1-x}N$ layers. *Applied Physics Letters*, **78** (15), 2137–2139.

389 McCluskey, M.D., Van der Walle, C.G., Romano, L.T., Krusor, B.S. and Johnson, N.M. (2003) Effect of composition on the band gap of strained $In_xGa_{1-x}N$ alloys. *Journal of Applied Physics*, **93**, 4340–4342.

390 Wu, J., Walukiewicz, W., Yu, K.M., Ager, J.W., III, Haller, E.E., Hai Lu and Schaff, W.J. (2002) Small bandgap bowing in $In_{1-x}Ga_xN$ alloys. *Applied Physics Letters*, **80**, 4741.

391 Shan, W., Walukiewicz, W., Haller, E.E., Little, B.D., Song, J.J., McCluskey, M.D., Johnson, N.M., Feng, Z.C., Schurman, M. and Stall, R.A. (1998) *Journal of Applied Physics*, **84**, 4452.

392 Pereira, S., Correia, M.R., Monteiro, T., Pereira, E., Alves, E., Sequeira, A.D. and Franco, N. (2001) *Applied Physics Letters*, **78**, 2137.

393 O'Donnell, K.P., Martin, R.W., Trager-Cowan, C., White, M.E., Esona, K., Deatcher, C., Middleton, P.G., Jacobs, K., van der Stricht, W., Merlet, C., Gil, B., Vantomme, A. and Mosselmans, J.F.W. (2001) *Materials Science & Engineering B: Solid State Materials for Advanced Technology*, **82**, 194.

394 Nakamura, S. and Mukai, T. (1992) *Japanese Journal of Applied Physics*, **3** (1), L1457.

395 Nakamura, S., Mukai, T. and Seno, M. (1993) *Japanese Journal of Applied Physics*, **31**, L16.

396 Nakamura, S., Iwasa, N. and Nagahama, S. (1993) *Japanese Journal of Applied Physics*, **32**, L338–341.

397 See, for example, Butte, R., Carlin, J.-F., Feltin, E., Gonschorek, M., Nicolay, S., Christmann, G., Simeonov, D., Castiglia, A., Dorsaz, J., Buehlmann, H.J., Christopoulos, S., Baldassarri, G., von Hogersthal, H., Grundy, A.J.D., Mosca, M., Pinquier, C., Py, M.A., Demangeot, F.,

Frandon, J., Lagoudakis, P.G., Baumberg, J.J. and Grandjean, N. (2007) Current status of AlInN layers lattice-matched to GaN for photonics and Electronics. *Journal of Physics D: Applied Physics*, **40**, 1–17.

398 Nakamura, S., Senoh, M., Nagahata, S., Iwasa, N., Yamada, T., Matsushita, T., Hiyoku, H. and Sugimoto, Y. (1996) *Japanese Journal of Applied Physics, Part 2: Letters*, **35** L74.

399 Wright, A.F. and Nelson, J.S. (1995) First-principles calculations for zinc-blende AlInN alloys. *Applied Physics Letters*, **66** (25), 3465–3467.

400 Onuma, T., Chichibu, S.F., Uchinuma, Y., Sota, T., Yamaguchi, S., Kamiyama, S., Amano, H. and Akasaki, I. (2003) Recombination dynamics of localized excitons in $Al_{1-x}In_xN$ epitaxial films on GaN templates grown by metalorganic vapor phase epitaxy. *Journal of Applied Physics*, **94** (4), 2449–2453.

401 Lukitsch, M.J., Danylyuk, Y.V., Naik, V.M., Huang, C., Auner, G.W., Rimai, L. and Naik, R. (2001) Optical and electrical properties of $Al_{1-x}In_xN$ films grown by plasma source molecular-beam epitaxy. *Applied Physics Letters*, **79** (5), 632–634.

402 Guo, Q., Ogawa, H. and Yoshida, A. (1995) *Journal of Crystal Growth*, **146**, 462.

403 Goano, M., Bellotti, E., Ghillino, E., Garetto, C., Ghione, G. and Brennen, K.F. (2000) *Journal of Applied Physics*, **88**, 6476.

404 Kim, K.S., Saxler, A., Kung, P., Razeghi, R. and Lim, K.Y. (1997) Determination of the band-gap energy of $Al_{1-x}In_xN$ grown by metal–organic chemical-vapor deposition. *Applied Physics Letters*, **71** (6), 800–802.

405 Yamaguchi, S., Kariya, M., Nitta, S., Takeuchi, T., Wetzel, C., Amano, H. and Akasaki, I. (1998) Observation of photoluminescence from $Al_{1-x}In_xN$ heteroepitaxial films grown by metalorganic vapor phase epitaxy. *Applied Physics Letters*, **73**, 830.

406 Starosta, K. (1981) *Physica Status Solidi a: Applied Research*, **68**, K55–K57.

407 Kubota, K., Kobayashi, Y. and Fujimoto, K. (1989) *Journal of Applied Physics*, **66**, 2984.

408 Kistenmacher, T.J., Ecelberger, S.A. and Bryden, W.A. (1993) *Journal of Applied Physics*, **74**, 1684.

409 Bedair, S.M., McIntosh, F.G., Roberts, J.C., Piner, E.L., Boutros, K.S. and El-Masry, N.A. (1997) *Journal of Crystal Growth*, **178**, 32.

410 Mohammad, S.N., Salvador, A. and Morkoç, H. (1995) Emerging GaN based devices. *Proceedings of the IEEE*, **83**, 1306–1355.

411 Nagamoto, T., Kuboyama, T., Minamino, H. and Omoto, O. (1989) *Japanese Journal of Applied Physics*, **28**, L1334.

412 Ryu, M.-Y., Chen, C.Q., Kuokstis, E., Yang, J.W., Simin, G. and Asif Khan, M. (2002) Luminescence mechanisms in quaternary $Al_xIn_yGa_{1-x-y}N$ materials. *Applied Physics Letters*, **80** (20), 3730–3733.

413 Williams, C.K., Glisson, T.H., Hauser, J.R. and Littlejohn, M.A. (1978) *Journal of Electronic Materials*, **7**, 639.

414 Angerer, H., Brunner, D., Freudenberg, F., Ambacher, O., Stutzmann, M., Höpler, R., Metzger, T., Born, E., Dollinger, G., Bergmaier, A., Karsch, S. and Körner, H.-J. (1997) Determination of the Al mole fraction and the band gap bowing of epitaxial $Al_xGa_{1-x}N$ films. *Applied Physics Letters*, **71** (11), 1504–1506.

415 Görgens, L., Ambacher, O., Stutzmann, M., Miskys, C., Scholz, F. and Off, J. (2000) Characterization of InGaN thin films using high-resolution X-ray diffraction. *Applied Physics Letters*, **76** (5), 577–579.

416 Peng, T., Piprek, J., Qiu, G., Olowolafe, J.O., Unruh, K.M., Swann, C.P. and Schubert, E.F. (1997) Band gap bowing and refractive index spectra of polycrystalline $Al_xIn_{1-x}N$ films deposited by sputtering. *Applied Physics Letters*, **71** (17), 2439–2441.

417 Bellaiche, L., Wei, S.-H. and Zunger, A. (1997) Bond-length distribution in tetrahedral versus octahedral semiconductor alloys: the case of

$Ga_{1-x}In_xN$. *Physical Review B: Condensed Matter*, **56** (21), 13872–13877.

418 Bernardini, F. and Fiorentini, V. (2001) Nonlinear macroscopic polarization in III–V nitride alloys. *Physical Review B: Condensed Matter*, **64**, 085207.

419 Bellaiche, L. (1999) Band gaps of lattice-matched (Ga,In)(As,N) alloys. *Applied Physics Letters*, **75** (17), 2578–2580.

420 Bellaiche, L., Wei, S.-H. and Zunger, A. (1997) Band gaps of GaPN and GaAsN alloys. *Applied Physics Letters*, **70**, 3558.

421 Wang, L.-W. (2001) Large-scale local-density-approximation band gap-corrected GaAsN calculations. *Applied Physics Letters*, **78** (11), 1565–1567.

422 Kent, P.R.C. and Zunger, A. (2001) Evolution of III–V nitride alloy electronic structure: the localized to delocalized transition. *Physical Review Letters*, **86** (12), 2613–2616.

423 Vurgaftman, I., Meyer, J.R. and Ram-Mohan, L.-R. (2001) Band parameters for III–V compound semiconductors and their alloys. *Journal of Applied Physics*, **89** (11), 5815–5875.

424 Morkoç, H. (2001) III-nitride semiconductor growth by MBE: recent issues. *Journal of Materials Science*, **12**, 677–695.

425 Kondow, M., Kitatani, T., Nakatsuka, S., Larson, M.C., Nakahara, K., Yazawa, Y., Okai, M. and Uomi, K. (1997) GaInNAs: a novel material for long wavelength semiconductor lasers. *IEEE Journal of Selected Topics in Quantum Electronics*, **3**, 719–730.

426 Harris, J.S., Jr (2000) Tunable long-wavelength vertical-cavity lasers: the engine of next generation optical networks? *IEEE Journal of Selected Topics in Quantum Electronics*, **6** (6), 1145–1160.

427 Kitatani, T., Nakahara, K., Kondow, M., Uomi, K. and Tanaka, T. (2000) A 1.3-μm GaInNAs/GaAs single-quantum-well laser diode with a high characteristic temperature over 200 K. *Japanese Journal of Applied Physics, Part 2: Letters*, **39** (2A), L86–L87.

428 Yang, K., Hains, C.P. and Cheng, J.L. (2000) Efficient continuous-wave lasing operation of a narrow-stripe oxide-confined GaInNAs–GaAs multiquantum-well laser grown by MOCVD. *IEEE Photonics Technology Letters*, **12** (1), 7–9.

429 Kondow, M., Kitatani, T., Nakahara, K. and Tanaka, T. (1999) A 1.3-μm GaInNAs laser diode with a lifetime of over 1000 hours. *Japanese Journal of Applied Physics, Part 2: Letters*, **38** (12A), L1355–L1356.

430 Li, N.Y., Hains, C.P., Yang, K., Lu, J., Cheng, J. and Li, P.W. (1999) Organometallic vapor phase epitaxy growth and optical characteristics of almost 1.2 μm GaInNAs three-quantum-well laser diodes. *Applied Physics Letters*, **75** (8), 1051–1053.

431 Sato, S. and Satoh, S. (1998) Room-temperature pulsed operation of strained GaInNAs/GaAs double quantum well laser diode grown by metal organic chemical vapour deposition. *Electronics Letters*, **34** (15), 1495–1497.

432 Kitatani, T., Kondow, M., Nakahara, K., Larson, M.C. and Uomi, K. (1998) Temperature dependence of the threshold current and the lasing wavelength in 1.3-μm GaInNAs/GaAs single quantum well laser diode. *Optical Review*, **5** (2), 69–71.

433 Nakatsuka, S., Kondow, M., Kitatani, T., Yazawa, Y. and Okai, M. (1998) Index-guide GaInNAs laser diode for optical communications. *Japanese Journal of Applied Physics, Part 1: Regular Papers, Short Notes & Review Papers*, **37** (3B), 1380–1382.

434 Ougazzaden, A., Bouchoule, S., Mereuta, A., Rao, E.V.K. and Decobert, J. (1999) Room temperature laser operation of bulk InGaAsN/GaAs structures grown by AP-MOVPE using N_2 as carrier gas. *Electronics Letters*, **35** (6), 474–475.

435 Fischer, M., Reinhardt, M. and Forchel, A. (2000) High temperature operation of GaInAsN laser diodes in the 1.3 μm regime. 58th Device Research Conference, IEEE, pp. 119–120.

436 Shimizu, H., Kumada, K., Uchiyama, S. and Kasukawa, A. (2000) High

performance CW 1.26 μm GaInNAsSb-SQW and 1.2 μm GaInAsSb-SQW ridge lasers. *Electronics Letters*, **36** (20), 1701–1703.

437 Setiagung, C., Shimizu, H., Ikenaga, Y., Kumada, K. and Kasukawa, A. (2003) Very low threshold current density of 1.3-μm-range GaInNAsSb–GaNAs 3 and 5 QWs lasers. *IEEE Journal of Selected Topics in Quantum Electronics*, **9** (5), 1209–1213.

438 Bank, S.R., Yuen, H.B., Bae, H., Wistey, M.A. and Harris, J.S. (2006) Overannealing effects in GaInNAs(Sb) alloys and their importance to laser applications. *Applied Physics Letters*, **88**, article 221115.

439 Gollub, D., Moses, S., Fischer, M. and Forchel, A. (2003) 1.42 μm continuous-wave operation of GaInNAs laser diodes. *Electronics Letters*, **39** (10), 777–778.

440 Ikenaga, Y., Miyamoto, T., Makino, S., Kageyama, T., Arai, M., Koyama, F. and Iga, K. (2002) 1.4 μm GaInNAs/GaAs quantum well laser grown by chemical beam epitaxy. *Japanese Journal of Applied Physics*, **41**, 664–665.

441 Tansu, N. and Mawst, L.J. (2002) Low-threshold strain-compensated InGaAs(N) ($\lambda = 1.19$–1.31 μm) quantum well lasers. *IEEE Photonics Technology Letters*, **14** (4), 444–446.

442 Peng, C.S., Jouhti, T., Laukkanen, P., Pavelescu, E.-M., Konttinen, J., Li, W. and Pessa, M. (2002) 1.32-μm GaInNAs-GaAs laser with a low threshold current density. *IEEE Photonics Technology Letters*, **14** (3), 275–277.

443 Yang, X., Jurkovic, M.J., Heroux, J.B. and Wang, W.I. (1999) Molecular beam epitaxial growth of InGaAsN:Sb/GaAs quantum wells for long-wavelength semiconductor lasers. *Applied Physics Letters*, **75** (2), 178–180.

444 Yang, X., Heroux, J.B., Mei, L.F. and Wang, W.I. (2001) InGaAsNSb–GaAs quantum wells for 1.55 μm lasers grown by molecular-beam epitaxy. *Applied Physics Letters*, **78** (26), 4068–4070.

445 Vurgaftman, I., Meyer, J.R., Tansu, N. and Mawst, L.J. (2003) (In)GaAsN–GaAsSb type-II "W" quantum-well lasers for emission at $\lambda = 1.55$ μm. *Applied Physics Letters*, **83** (14), 2742–2744.

446 Bank, S.R., Wistey, M.A., Goddard, L.L., Yuen, H.B., Lordi, V. and Harris, J.S., Jr (2004) Low-threshold continuous-wave 1.5-μm GaInNAsSb lasers grown on GaAs. *IEEE Journal of Quantum Electronics*, **40** (6), 656–664.

447 Fischer, M., Reinhardt, M. and Forchel, A. (2000) Room-temperature operation of GaInAsN/GaAs laser diodes in the 1.5 μm range. Conference Digest, 2000 IEEE 17th International Semiconductor Laser Conference (Cat. No. 00CH37092), IEEE, Piscataway, NJ, pp. 115–116.

448 Livshits, D.A., Egorov, Yu.A. and Riechert, H. (2000) 8 W continuous wave operation of InGaAsN lasers at 1.3 μm. *Electronics Letters*, **36** (16), 1381–1382.

449 Bugge, F., Erbert, G., Fricke, J., Gramlich, S., Staske, R., Wenzel, H., Zeimer, U. and Weyers, M. (2001) 12 W continuous-wave diode lasers at 1120 nm with InGaAs quantum wells. *Applied Physics Letters*, **79** (13), 1965–1967.

450 Reinhardt, M., Fischer, M., Kamp, M. and Forchel, A. (2000) 7.8 GHz small-signal modulation bandwidth of 1.3 μm DQW GaInAsN/GaAs laser diodes. *Electronics Letters*, **36** (12), 1025–1026.

451 Steinle, G., Mederer, F., Kicherer, M., Michalzik, R., Kristen, G., Egorov, A.Y., Riechert, H., Wolf, H.D. and Ebeling, K.J. (2001) Data transmission up to 10 Gbit/s with 1.3 μm wavelength InGaAsN VCSELs. *Electronics Letters*, **37** (10), 632–634.

452 Fischer, M., Reinhardt, M. and Forchel, A. (2000) A monolithic GaInAsN vertical-cavity surface-emitting laser for the 1.3-μm regime. *IEEE Photonics Technology Letters*, **12** (10), 1313–1315.

453 Schneider, H.C., Fischer, A.J., Chow, W.W. and Klem, J.F. (2001) Temperature dependence of laser threshold in an In GaAsN vertical-cavity surface-emitting laser. *Applied Physics Letters*, **78** (22), 3391–3393.